

Dissertation

Zur Erlangung des Grades

Doktor der Naturwissenschaften

**Quantitative interactomics screen reveals the role of the
lncRNA ANRIL during viral infection**

Am Fachbereich Biologie

Der Johannes Gutenberg-Universität Mainz

Patricia Schupp

geb. am 18.02.1995 in Darmstadt

Mainz, 2025

In Copyright (InC-1.0)

Dekan: Prof. Dr. Eckhard Thines

1. Berichterstatter:

2. Berichterstatter:

Tag der mündlichen Prüfung: 20.11.2025

“To the people who look at the stars and wish.”
“To the stars who listen –
and the dreams that are answered.”

- Sarah J. Maas

Table of Contents

Preface.....	VI
Summary	VII
Zusammenfassung.....	VIII
Acknowledgements	IX
Abbreviations.....	X
Introduction.....	1
Non-coding RNAs	1
Long non-coding RNAs (lncRNAs)	2
Identification of lncRNA-protein interactions	6
The lncRNA ANRIL	8
The role of lncRNAs in viral infections.....	13
Type I interferon signaling in response to viral infections.....	13
Cedar Virus.....	17
Aims of the thesis	21
Results	22
Quantitative interactomics screen uncovers 310 proteins binding to ANRIL.....	22
Characterization of novel ANRIL-binding protein C7orf50.....	23
Functional Domains of ANRIL.....	27
ANRIL interacts with proteins that are involved in viral processes	28
ANRIL knockdown deregulates immune related pathways involved in interferon signaling and viral entry.....	31
ANRIL is differentially regulated in response to viral infection	33
ANRIL is expressed in a time- and dose-dependent manner and associates with immune activation during CedV infection.....	36
ANRIL knockdown increases CedV replication	38
INO80 knockdown shows mild effect on CedV infection	39

Discussion	42
ANRIL as a multifaceted regulator in chromatin and splicing	42
C7orf50 interaction with ribosomal proteins links ANRIL to 60S maturation	45
ANRIL as a protective factor during CedV infection	46
Conclusion	49
Material and Methodes.....	50
Materials	50
Buffers and Solutions	50
Antibodies.....	51
Reagents	51
Commercial assays.....	53
Consumables.....	54
Instruments.....	54
Primers.....	55
Methods	57
Cell culture	57
Plasmids	57
Nuclear extract preparation from cell lines	57
Preparation of RNA Fragments for the ANRIL interactome	58
Pulldown	59
Mass spectrometry sample preparation and measurement	59
LR recombination to N-terminally tag C7orf50.....	61
Bacterial transformation and plasmid extraction	61
Linear polyethylenimine (PEI) transient transfection of GFP-C7orf50.....	62
Extracting protein from eukaryotic cells.....	62
Western Blot for the validation of C7orf50 binding to ANRIL.....	62
Treatment-Immunoprecipitation (IP).....	63

AlphaFold3 binding prediction and visualization of C7orf50 to ANRIL	65
Fluorescence microscopy to detect C7orf50 localization	65
EsiRNA induced knockdown	65
RT-qPCR.....	66
RNA View Fluorescence in situ hybridization (FISH)	67
RNA-Seq (TruSeq) to investigate transcriptome-wide changes after ANRIL knockdown.....	67
Viral Infections	68
RNA sequencing (Quant-seq) for viral infection studies	68
Determination of TCID ₅₀	69
Bioinformatic analysis.....	69
Declaration of Generative AI and AI-assisted technologies in the writing process	70
Appendix.....	71
Supplementary Tables.....	72
References	79
Curriculum vitae	96

Preface

The work presented in this dissertation was primarily conducted by me. I was responsible for the conceptualization and execution of most experiments, data interpretation, and manuscript writing. Some experiments were conducted with the valuable support and collaboration from others:

- Bioinformatic data analysis was supported by Dr. Michal Levin (IMB, Mainz).
- RNA sequencing library preparation was performed by Lars Teschke (FLI, Greifswald) and sequencing was carried out by the Genomics Core Facility at the IMB.
- All viral infections were performed by Henriette Schwotzer (FLI, Greifswald).
- Some experiments were performed in close collaboration with my Master's student, Michelle Alff, and selected data included here were also part of her Master's thesis.

Disclaimer:

Parts of the text and figures included in this dissertation were used to prepare the following scientific manuscript:

Schupp et al. (2025). "Quantitative interactomics screen reveals the role of the lncRNA ANRIL during viral infection" - in submission

Additionally, parts of this dissertation were previously included in the following Master's thesis:

"Investigating the regulatory Role of lncRNA ANRIL Expression upon Cedar Infection in Human Cells using a Multi-Omics Approach" by Michelle Alff.

Summary

Recent advances in deep sequencing technologies have revealed that while only 2-5% of the human genome encodes protein-coding genes, an estimated 80% of these genes are actively transcribed into a variety of non-coding RNAs. Among these, long non-coding RNAs represent a major subclass, with over 35,000 annotated genes. Despite their abundance, most of these genes remain functionally uncharacterized.

The antisense non-coding RNA in the INK4 locus (ANRIL) is transcribed from the disease-associated hotspot 9p21.3, which has been implicated in cancer development and cardiovascular disorders, yet its molecular functions remain poorly defined. To systematically characterize ANRIL, a quantitative mass spectrometry-based interactomics screen using 14 nonoverlapping RNA fragments covering the longest ANRIL isoforms was performed. This strategy identified 310 interacting proteins, each exhibiting distinct binding patterns across different fragments, revealing both previously described and yet unknown interactors.

Among the newly identified proteins, the uncharacterized protein C7orf50 bound to two ANRIL fragments. Functional characterization revealed an enrichment of C7orf50 interactors involved in ribosomal biogenesis, including known ANRIL-binding members of the PeBoW complex. These findings suggest a potential role of C7orf50 during ribosomal maturation and indicate an additional target of ANRIL-mediated regulation during ribosome biogenesis.

Furthermore, computational analysis of the ANRIL interactome recapitulated previously reported biological functions, such as chromatin remodeling, while also suggesting previously unrecognized roles in virus infection. Interestingly, ANRIL knockdown led to altered expression of genes associated with interferon signaling and viral entry. Infection studies with dsDNA and ssRNA viruses resulted in virus-specific modulation of ANRIL expression. Notably, ANRIL was upregulated in response to cedar virus (CedV) infection in a time- and dose-dependent manner. Transcriptomic analysis revealed a concurrent increase in immune response genes, particularly those involved in type I interferon signaling. Furthermore, ANRIL lockdown led to increased CedV RNA levels and titers, demonstrating a link between ANRIL and viral infection. Preliminary mechanistic insights indicated that the knockdown of the newly identified ANRIL-interacting protein INO80 also increased CedV RNA levels. However, further analyses are required to determine the precise molecular mechanisms involved.

Overall, the unbiased RNA-protein interaction screen provides insights into how ANRIL mediates various cellular functions through protein interactions and paves the way for future investigations into the role of ANRIL in health and disease.

Zusammenfassung

Neue Fortschritte in der Hochdurchsatz-Sequenzierungstechnologie haben gezeigt, dass lediglich 2-5% des menschlichen Genoms für proteinkodierende Gene verantwortlich sind, während schätzungsweise 80% aktiv in nicht-kodierende RNAs transkribiert werden. Ein Großteil davon sind, mit über 35.000 annotierten Genen, lange nicht-kodierende RNAs (lncRNAs). Trotz ihrer Häufigkeit sind die meisten jedoch bislang funktionell kaum bis gar nicht charakterisiert.

Die Antisense-nicht-kodierende RNA im INK4-Locus (ANRIL) wird aus dem krankheitsassoziierten Hotspot 9p21.3 transkribiert, der mit der Entstehung von Krebs und kardiovaskulären Erkrankungen in Verbindung gebracht wird. Dennoch sind die molekularen Funktionen von ANRIL bislang weitgehend unklar. Zur Charakterisierung von ANRIL wurde ein quantitativer, Massenspektrometrie basierter Interaktom-Screen mit 14, sich nicht überlappenden, RNA-Fragmenten der längsten ANRIL-Isoform durchgeführt. Dadurch wurden 310 ANRIL-interagierende Proteine identifiziert, die jeweils unterschiedliche Bindungsmuster aufwiesen. Darunter sowohl bereits bekannte ANRIL bindende Proteine, als auch bislang nicht identifizierte Interaktionspartner.

Unter diesen neu identifizierten Proteinen zeigte das bislang weitestgehend uncharakterisierte Protein C7orf50 eine spezifische Bindung an zwei ANRIL-Fragmenten. Analysen zur Funktionscharakterisierung ergaben eine Anreicherung von C7orf50-Interaktionspartnern, die an der Ribosomenbiogenese beteiligt sind, darunter auch bekannte ANRIL-Bindungspartner des PeBoW-Komplexes. Die Ergebnisse deuten auf eine mögliche Rolle von C7orf50 bei der Ribosomenreifung hin und legen nahe, dass ANRIL über die Interaktion mit C7orf50 ebenfalls in diesem Prozess eine regulatorische Funktion ausüben könnte.

Zusätzliche bioinformatische Analysen des ANRIL-Interaktoms bestätigen bekannte biologische Funktionen und wiesen zugleich auf eine bislang unerforschte Rolle bei Virusinfektionen hin. Interessanterweise führte der Knockdown von ANRIL zu einer veränderten Expression von Genen, die mit dem Interferon-Signalweg sowie dem viralen Eintritt assoziiert sind. Infektionsstudien mit dsDNA und ssRNA Viren zeigten eine virusspezifische Modulation der ANRIL-Expression. In weiterführenden Experimenten mit dem ssRNA Cedar Virus (CedV), konnte eine zeit- und dosisabhängige Hochregulation von ANRIL beobachtet werden. Transkriptomanalysen ergaben eine gleichzeitige Induktion von immunregulierenden Genen, insbesondere solcher, die am Typ-I-Interferon-Signalweg beteiligt sind. Zudem führte die Runterregulierung von ANRIL mittels RNA Interferenz zu einem Anstieg der CedV-RNA-Menge und Virustiter, was eine Verbindung zwischen ANRIL und viraler Infektion nahelegt. Erste funktionelle Hinweise deuten darauf hin, dass die Runterregulierung des neu identifizierten ANRIL-Bindungspartners INO80 ebenfalls zu einem Anstieg der CedV-RNA-Menge führt. Der genaue molekulare Mechanismus bedarf jedoch weiterer Untersuchung.

Insgesamt liefert der RNA-Protein-Interaktionsscreen Einblicke in die vielfältigen zellulären Funktionen von ANRIL, welche durch Proteininteraktionen vermittelt werden und ebnet den Weg für zukünftige Studien zur Rolle von ANRIL in Gesundheit und Krankheit.

Acknowledgements

-

Abbreviations

Abbreviations

A549	Alveolar epithelial cells	CBX7	Chromobox 7
ABC	Ammonium bicarbonate	CC	Cellular compartment
ACN	Acetonitrile	CDK	Cyclin-dependent kinase
AF	Assembly factors	CDKN2A	Cyclin Dependent Kinase Inhibitor 2A
Ago2	Argonaute 2	CDKN2B	Cyclin Dependent Kinase Inhibitor 2B
AIDS	Acquired immunodeficiency syndrome	CedV	Cedar virus
ANRIL	Antisense non-coding RNA in the INK4 locus	CHART	Capture hybridization analysis of RNA targets
ARF	Alternate reading frame protein product of the CDKN2A locus	ChIP	Chromatin immunoprecipitation
AltS	Alternative splicing	ChIRP	Chromatin isolation by RNA purification
AS-lncRNA	Antisense lncRNA	circRNAs	Circular RNA
ATL	T-cell leukemia	CLIP	Crosslinking immunoprecipitation
BAZ1B	Bromodomain adjacent to zinc finger domain protein 1B	CO₂	Carbon dioxide
BOP1	Block Of Proliferation 1	CPM	Counts per million
BP	Biological process	CTD	C-terminal domain
BRD3	Bromodomain Containing 3	CTRL	Control
BSA	Bovine serum albumin	DAPI	4',6-diamidino-2-phenylindole
BSL	Biosafety level	DDX	DEAD-box helicase
C7orf50	Chromosome 7, Open Reading Frame 50	DHX	DEAH-box helicase
CAD	Coronary atherosclerotic heart disease	DMEM	Dulbecco's Modified Eagle Medium
CARD	Caspase activation and recruitment domains	DNA	Deoxyribonucleic acid

Abbreviations

DPBS	Dulbecco's phosphate-buffered saline	FUS	Fused In Sarcoma
dsRNA	double-stranded RNA	G	Glycoprotein
DTT	Dithiothreitol	G1/S-phase	Gap 1/Synthesis-phase
EBV	Epstein-Barr Virus	GA-rich	Guanine and Adenine-rich
eCLIP	enhanced CLIP	GFP	Green Fluorescent Protein
EDTA	Ethylenediaminetetraacetic acid	GMEM	Glasgow's Minimum Essential Medium
EIF2AK2	Eukaryotic Translation Initiation Factor 2 Alpha Kinase 2 (PKR)	GO	Gene Ontology
ELAVL1	Embryonic Lethal, Abnormal Vision, Drosophila)-Like 1 (Hu Antigen R; HuR)	GWAS	Genome-wide association studies
EPHA2	Ephrin Type-A Receptor 2	H1N1	Influenza A virus subtype H1N1
eRNA	enhancer RNA	H2AK119Ub	Monoubiquitination of histone H2A at lysine 119
esiRNA	Endoribonuclease-prepared small interfering RNA	H3K27me3	Trimethylation of lysine 27 on histone H3
Ex	Exon	H3N2	Influenza A virus
EZH2	Enhancer Of Zeste 2 Polycomb Repressive Complex 2 Subunit	HDAC3	Histone Deacetylase 3
F	Transmembrane-anchor Fusion protein	HeLa	Henrietta Lacks cell line
FACT	Facilitates Chromatin Transcription complex	HeV	Hendra virus
FBS	Fetal bovine serum	HF-Polymerase	High-Fidelity DNA Polymerase
FC	Fold change	HH	Hammerhead
FDR	False discovery rate	hnRNP	Heterogeneous nuclear ribonucleoproteins
FISH	Fluorescence in situ hybridization	HOTAIR	HOX transcript antisense RNA
FPKM	Fragments per kilobase of transcript per million	hpi	Hours post-infection

Abbreviations

HSV	Herpes simplex 1	KLF2	Kruppel-Like Factor 2
HTLV	Human T-cell leukemia virus type I	KSHV	Kaposi's sarcoma-associated herpesvirus
HTNV	Hantaan virus	L	Polymerase
HUVEC	Human umbilical vein endothelial cell	LDS	Lithium dodecyl sulfate
IAA	Iodoacetamide	LFQ	Label-free quantitation
IFIT	IFN-induced proteins with tetratricopeptide repeats	LGALS1	Lectin, Galactoside-Binding, Soluble, 1 (Galectin-1)
IFN	Interferon	lincRNA	intergenic lncRNA
IFNAR	Interferon Alpha And Beta Receptor	lncRNA	long non-coding RNA
IGF2BP3	Insulin-like growth factor 2 mRNA-binding protein 3	LR	Recombination reaction between attL and attR sites
IKKε	Inhibitor Of Nuclear Factor Kappa B Kinase Subunit Epsilon	LSD1	Lysine Demethylase 1A
IL	Interleukins	M	Matrix protein
ILF	Interleukin Enhancer Binding Factor	m⁷G	7-methylguanosine
INO80	INO80 Complex ATPase Subunit	MALAT1	Metastasis Associated Lung Adenocarcinoma Transcript 1
IP	Immunoprecipitations	MAP	Mitogen-Activated Protein
ipTM	interface predicted template modelling	MAP2K6	Mitogen-Activated Protein Kinase 6
IRF	Interferon Regulatory Factor	MAVS	Mitochondrial antiviral-signaling protein
ISG	IFN-stimulated genes	MDA-5	Melanoma differentiation associated gene 5
ISGF3	IFN-stimulated gene factor 3	MDM2	Mouse Double Minute 2
ISRE	IFN-stimulated response elements	MEG3	Maternally expressed gene 3
JAK1	Janus Kinase 1	MF	Molecular function

Abbreviations

miRNA	microRNA	PAMP	Pathogen-associated molecular patterns
MOI	Multiplicities of infection	PANDA	p21-associated noncoding RNA DN A damage activated
MOV10	Moloney Leukemia Virus 10	PAR-CLIP	Photoactivatable-ribonucleoside-enhanced CLIP
MS	Mass spectrometer	PCA	Principal Component Analysis
MX1	Myxoma Resistance Protein 1	PCC	Pearson correlation coefficients
N	Nucleoprotein	PCR	Polymerase Chain Reaction
ncRNA	non-coding RNAs	PeBoW	PES1-BOP1-WDR12 complex
NCS	Newborn Calf Serum	Pen-Strep	Penicillin and Streptomycin
NEAT1	Nuclear Enriched Abundant Transcript 1	PES1	Pescadillo Ribosomal Biogenesis Factor 1
NECTIN2	Nectin Cell Adhesion Molecule 2	PFA	Paraformaldehyde
NF-YA	Nuclear Transcription Factor Y Subunit Alpha	piRNA	PIWI-interacting RNA
NF-κB	nuclear factor 'kappa-light-chain-enhancer' of activated B-cells	PMSF	Phenylmethanesulfonyl fluoride
NiV	Nipah virus	PP1α/γ	Protein Phosphatase α/γ
NOP58	Nucleolar Protein 58	PPI	Protein-Protein interaction
Nop7	Yest homologs of PES1	PRC	Polycomb Repressive Complex
NOX1	NADPH Oxidase 1	PRPF	pre-mRNA processing factors
NRAV	Negative Regulator Of Antiviral Response	PRR	PAMP-recognition receptors
nt	Nucleotides	PrV	Pseudorabies virus
NTP	Nucleoside triphosphates	PTB-AS	PTB-Antisense RNA
OAS	2'-5'-Oligoadenylate Synthetase	PTBP1	Polypyrimidine Tract Binding Protein 1
P	Phosphoprotein	RAF1	Raf-1 Proto-Oncogene, Serine/Threonine Kinase
p53	Tumor Protein P53	RAP-MS	RNA antisense purification MS
p65	RELA	RBP	RNA-binding protein

Abbreviations

Rbp95	rRNA-binding protein helix H95	SMARCC2	SWI/SNF Related, Matrix Associated, Actin Dependent Regulator of Chromatin Subfamily C Member 2
RDI	RNA-dependent inteaction	sncRNA	small ncRNA
REST	RE1-Silencing Transcription Factor	Sox2ot	Sox2 overlapping transcript
RIG-I	Retinoic Acid-Inducible Gene 1	STAT	signal transducer and activator of transcription
RIP	RNA immunoprecipitation	SUZ12	Suppressor of Zeste 12
RIPA	Radioimmunoprecipitation assay	SWI/SNF	Switch/Sucrose Non-Fermenting
RISC	RNA induced silencing complex	T2D	Type 2 diabetes
RLRs	RIG-I-like receptors	TBK1	TANK-binding kinase 1
RLuc	Renilla Luciferase	TCID₅₀	Tissue Culture Infectious Dose 50
RNA	Ribonucleic acid	TERC	Telomerase RNA Component
RNAPII	RNA polymerase II	TERRA	Telomeric Repeat-containing RNA
RNP	Ribonucleoprotein	TERT	Telomerase Reverse Transcriptase
RPKM	Reads Per Kilobase Million	TGF-β	Transforming Growth Factor Beta
Rpl3	60S ribosomal protein L3	TLRs	Toll-like receptors
rRNA	ribosomal RNA	TNF	Tumor Necrosis Factor
RSL24D1	Ribosomal L24 Domain Containing 1	TRIM25	Tripartite Motif Containing 25
RT	Room temperature	tRNA	transfer RNA
RT-qPCR	Quantitative reverse transcription polymerase chain reaction	TYK2	Tyrosin Kinase 2
S1	Streptavidin aptamer	UPF1	Up-Frameshift Suppressor 1 Homolog
SARS-CoV-2	severe acute respiratory syndrome coronavirus 2	USP18	ubiquitin specific peptidase 18
SDC	Sodium Deoxycholate Detergent	UTR	Untranslated region
SF	Splicing factors	vFLIP	Viral FLICE-Like Inhibitory Protein
siRNA	small interfering RNA	VIM-AS1	Vimentin Antisense RNA 1

Abbreviations

VSMC	vascular smooth muscle cells
VSV	Vesicular stomatitis virus
WDR12	WD Repeat-Containing Protein 12
WDR5	WD Repeat Domain 5
Ytm1	Yeast Telomere Maintenance 1
YY1	Ying Yang 1
ZAP-IT1	Zika virus Activated lncRNA Promoting IFN-beta Transcription 1

Introduction

Disclaimer: Some parts of this section are part of my own paper Schupp et al. "Quantitative interactomics screen reveals the role of the lncRNA ANRIL during viral infection" (submitted)

Non-coding RNAs

Deep sequencing technologies in recent years have revealed, that, while only 2-5% of the human genome is transcribed into approximately 20,000 protein-coding genes, a surprisingly high percentage, between 75-80%, is actively transcribed into a diverse set of non-coding RNAs (ncRNAs) (2-5) (Figure 1A). NcRNAs are broadly categorized based on their function into two main groups: housekeeping and regulatory ncRNAs (5,6). Housekeeping ncRNAs are widely and ubiquitously expressed to maintain essential steps of cellular functions (6) and include well-characterized classes such as ribosomal RNAs (rRNAs) and transfer RNAs (tRNAs). In contrast, regulatory ncRNAs modulate gene expression through a variety of mechanisms, including epigenetic modifications, transcriptional regulation, and post-transcriptional processing (6). Based on their lengths, they are further divided into small ncRNAs (sncRNAs), which are shorter than 200 nucleotides (nt), including microRNAs (miRNAs) and small interfering RNAs (siRNAs), and long ncRNAs (lncRNAs) defined as transcripts longer than 500 nt (3) (Figure 1B).

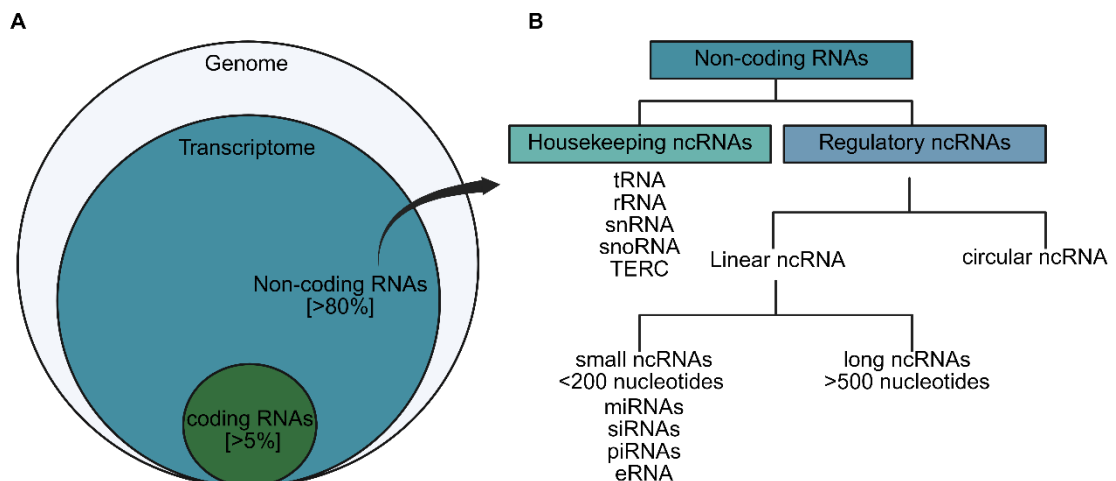


Figure 1 Classifications of non-coding RNAs

(A) The majority of the human genome is transcribed into non-coding RNAs (ncRNAs), while less than 5% is transcribed into protein-coding genes. (B) The class of ncRNAs is subdivided into two categories: Housekeeping ncRNAs and regulatory ncRNAs. Housekeeping ncRNAs include transfer RNAs (tRNA), ribosomal RNAs (rRNAs), small nuclear RNAs (snRNA), small nucleolar RNAs (snoRNAs) and telomerase RNA (TERC). Regulatory ncRNAs are further divided based on their structure into circular and linear ncRNAs. Linear ncRNAs are classified by length into small ncRNAs (<200 nucleotides) and long ncRNAs (>500 nucleotides). Small ncRNAs include microRNAs (miRNAs), small interfering RNAs (siRNA), PIWI-interacting RNAs (piRNA) and enhancer RNAs (eRNAs). Figure adapted from Gomes, C. P. d. C., et al. (2019).

Long non-coding RNAs (lncRNAs)

lncRNAs represent a major portion within the ncRNA landscape. According to the latest release from the Ensembl-GENCODE project (GENCODE 47), over 35,000 genes in the human genome have been annotated as encoding for lncRNAs (2), the majority of which remain functionally uncharacterized. lncRNAs are commonly classified based on their genomic location relative to protein-coding genes into several categories: intergenic lncRNAs (lincRNA), intronic lncRNAs, antisense lncRNAs (AS-lncRNAs) and bidirectional lncRNAs. lincRNAs are transcribed in the sense direction from genomic regions located between two protein-coding genes (Figure 2A), whereas intronic lncRNAs originate from introns between exons of a protein-coding gene (Figure 2B). Contrary, AS-lncRNAs are transcribed from the opposite strand of a protein-coding gene and partially or fully overlap with its sequence (Figure 2C). In contrast, bidirectional lncRNAs are transcribed in the opposite direction of a nearby protein-coding gene, initiating close to the same promoter region but without overlapping its sequence (Figure 2D) (7,8). Notably, lncRNAs can also be transcribed from so called pseudogenes (9). Many of the described lncRNAs are encoded by RNA polymerase II (RNAPII) and undergo post-transcriptional processing, including 7-methylguanosine (m⁷G) capping, 3'-end polyadenylation, and splicing (10). Splicing results in multiple lncRNA isoforms, that may have distinct molecular functions, by altering the interaction properties of the lncRNA (11,12) (Figure 2E).

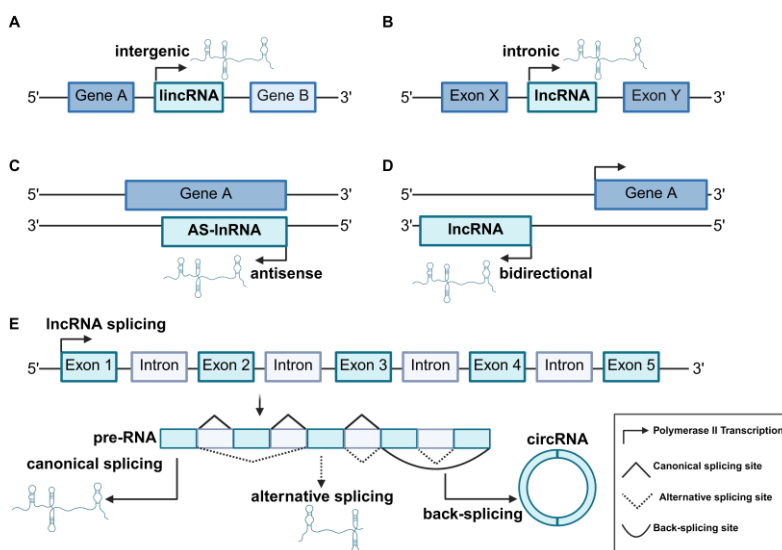


Figure 2 Types of lncRNAs based on genomic origin and processing

Classification of lncRNAs based on their genomic origin. (A) Intergenic lncRNAs (lincRNAs) are transcribed from genomic regions located between two protein coding genes. (B) Intronic lncRNAs are transcribed from intronic sequences within a protein-coding gene. (C) Antisense lncRNAs (AS-lncRNAs) are transcribed from the opposite to a protein-coding gene, overlapping it in an antisense orientation. (D) Bidirectional lncRNAs are also transcribed from the complementary strand of a protein-coding gene, but its transcription is initiated near the same promoter but in the reverse direction, without overlapping the protein-coding gene sequence. (E) lncRNAs are processed by splicing, resulting in either linear lncRNAs through canonical or alternative splicing or circular RNAs (circRNAs) via back-splicing. Figure based on Naseer, Q. A., et al. (2024) and Fernandes, J. C. R., et al. (2019)

Introduction

An example highlighting the functional impact of alternative splicing (Alts) in lncRNAs is the AS-lncRNA HOTAIR (HOX antisense intergenic RNA). HOTAIR plays a critical role in transcription regulation and chromatin remodeling through interactions with chromatin-modifying complexes (13). Specifically, its 5' domain binds the polycomb repressive complex 2 (PRC2), while its 3' domain interacts with the LSD1/CoREST/REST complex (14). AltsS of the HOTAIR gene transcript generates multiple splice variants, leading to the exclusion or truncation of those binding domains, possibly influencing its functionality (15).

While both canonical and alternative splicing generate linear lncRNA transcripts, a process known as back-splicing results in the formation of circular RNAs (circRNAs). Back-splicing relies on the canonical spliceosome machinery and occurs when a 5'-splice donor site is joined to an 3'-splice acceptor site, resulting in covalent 3'-5' phosphodiester bond that forms the circular RNA molecule (16,17). This closed structure makes circRNAs more stable than their linear counterparts, as they show higher resistance towards exonuclease-mediated degradation (18,19).

Beyond their structural diversity, lncRNAs also exhibit diverse expression patterns and distinct subcellular localizations. In comparison with mRNAs, most lncRNAs are predominantly localized in the nucleus, where they are often involved in transcriptional regulation or chromatin remodeling (20,21). However, some lncRNAs can also localize to the cytoplasm, regulating mRNA stability or translation (22). While most lncRNAs are generally expressed at lower levels compared to mRNAs, showing tightly regulated, tissue- and cell type-specificity expression, a few lncRNAs such as MALAT1 and NEAT1 are exceptionally high abundant (23).

lncRNAs influence the transcriptome and proteome by interacting with various cellular components such as, DNA, RNAs, miRNAs or proteins (24-26) (Figure 3), thereby influencing a wide range of biological processes (27,28).

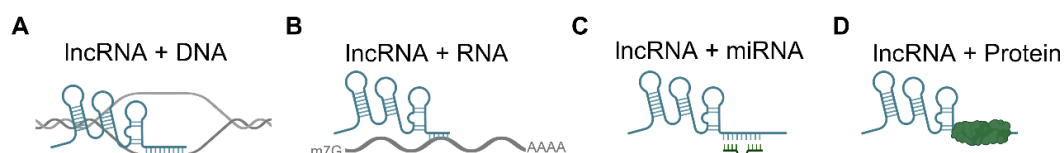


Figure 3 Functions of lncRNAs

lncRNAs can interact with (A) DNA, (B) RNA, (C) microRNA (miRNA) or (D) proteins to carry out their cellular functions. Figure adapted from Cheng, J.-T., et al. (2019).

lncRNAs can directly bind to genomic DNA to form RNA-DNA hybrid structures known as R-loops (29) (Figure 3A). For instance, the telomeric repeat-containing RNA TERRA has been shown to form R-loops

Introduction

at short yeast telomers, inducing homology-directed repair delaying senescence (30). Similarly, R-loop formation by lncRNAs can also directly modulate gene expression (27). VIM-AS1, for example, forms an R-loop around the promoter of the gene vimentin, leading to chromatin opening and enhanced binding of transcriptional activators (31).

Another mode of action is the formation of RNA-RNA complexes, where lncRNAs bind to their target mRNAs to influence their stability (Figure 3B). The lncRNA PTB-AS, for example, binds to the 3'UTR of PTBP1 mRNA, preventing its miRNA-mediated degradation by blocking their binding sites (32).

In addition, lncRNAs can also directly interact with miRNAs (Figure 3C), often functioning as miRNA sponges or competitive endogenous RNAs (ceRNAs). By sequestering miRNAs, they protect target mRNAs from degradation. One example being the tumor-derived lncRNA Sox2ot. Sox2ot promotes epithelial-mesenchymal transition by regulating SOX2 levels through miR-200 binding (33). Conversely, miRNAs can also regulate the abundance of lncRNAs via miRNA-triggered decay (34). For example, ELAVL1 (HuR) facilitates the recruitment of the miRNA let-7 together with the Argonaute (Ago2) to the lncRNA HOTAIR, forming a RNA induced silencing complex (RISC) and thereby promoting its degradation (35).

Among all interaction types, protein binding is considered the most prominent mechanism by which lncRNAs exert their regulatory functions (36,37). Those interactions are generally classified into three main categories: guides, decoys and scaffolds (Figure 4).

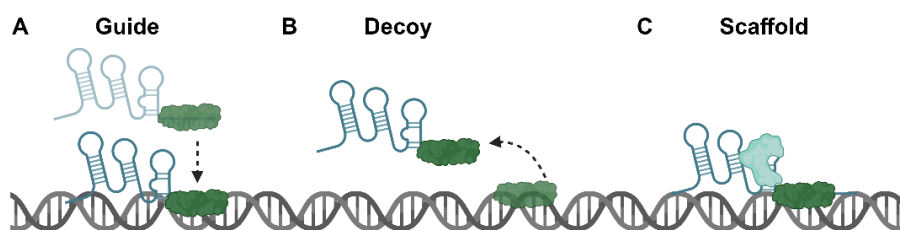


Figure 4 Functional mechanisms of lncRNA interactions with proteins

lncRNAs regulate diverse cellular through interactions with proteins, by acting (A) as guides, directing proteins to specific DNA sequences; (B) as decoys, sequestering proteins away from their DNA targets; and (C) as scaffolds, facilitating the assembly of protein complexes by bringing interacting partners into proximity. Figure adapted from Cheng, J.-T., et al. (2019).

Specifically, lncRNAs can guide effector proteins to their target regions (Figure 5A). Growing evidence indicates that lncRNAs form RNA-DNA triplex structures that facilitate the recruitment of chromatin-modifying complexes to specific genomic loci (3). Among the best-studied are the complexes PRC1 and PRC2. Since neither complex contains proteins with sequence-specific DNA-binding domains (38), they depend in part on lncRNAs for accurate genomic targeting.

Introduction

For example, the lncRNA MEG3 forms triplexes at GA-rich sequences to guide the PRC2 subunit EZH2 to TGF- β pathway genes and regulate their expression (39).

Conversely, lncRNAs can also act as decoys, preventing proteins from acting at their usual targets (Figure 5B). For instance, the DNA damage activated lncRNA PANDA sequesters the nuclear transcription factor NF- κ B from promoters of pro-apoptotic genes, thereby promoting cell survival of DNA damaged cells (40).

When functioning as scaffolds, lncRNAs serve as structural platforms that bring multiple proteins into proximity, facilitating the assembly of ribonucleoprotein (RNP) complexes (Figure 5C). A well-known RNP complex mediated by a lncRNA is the telomerase complex, where the housekeeping lncRNA TERC acts as a scaffold for the catalytic protein TERT and other cofactors needed for telomere length maintenance (3,41).

Additionally, lncRNAs can also act as enhancers, interacting with transcriptional co-activators to stabilize or spatially arrange protein assemblies that promote gene expression (37).

Together, these mechanisms illustrate the multifaceted roles of lncRNAs in gene regulation. (Figure 5) Identifying protein partners of lncRNAs is therefore essential for understanding their diverse functions in cellular and disease contexts (42,43).

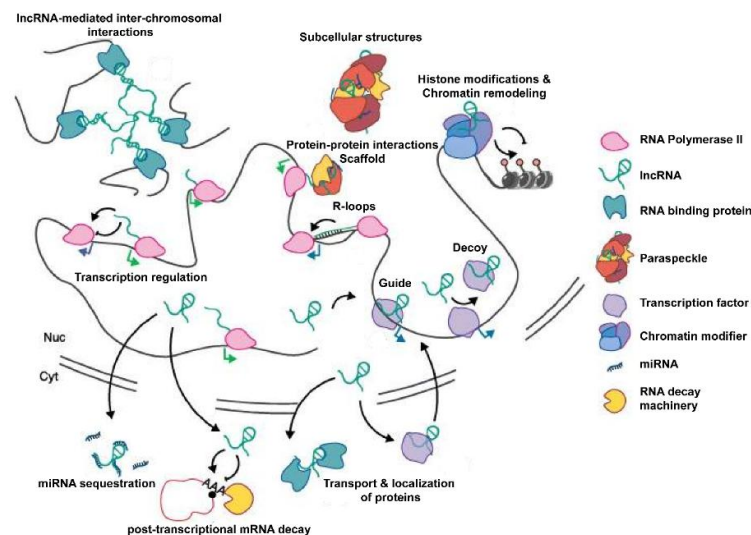


Figure 5 Functional diversity of lncRNAs

lncRNAs interact with DNA, RNA, and protein, thereby influencing a wide range of cellular functions. In the nucleus, lncRNAs can regulate gene transcription, mediate inter-chromosomal interactions, and contribute to the formation of nuclear structures, such as paraspeckles or R-loops. Through their binding to proteins, lncRNAs can function as guides, decoys or scaffolds, for example, guiding chromatin remodeling complexes to specific genomic loci to mediate different histone modifications to alter their chromatin state. They can also regulate the subcellular localization of proteins. In the cytoplasm, lncRNAs can act as molecular sponges for miRNAs or regulate mRNA stability and post-transcriptional decay. Figure adapted from Marchese, F. P., et al. (2017).

Identification of lncRNA-protein interactions

There are two complementary approaches for identifying RNA-protein interactions. The protein-centric strategy focuses on identifying RNA species bound to a protein of interest, whereas RNA-centric techniques identify proteins bound to a selected RNA (42,44) (Figure 6). Both approaches offer complementary insights into RNA-protein interactions.

The protein-centric approach focusses on selected proteins and the identification of their interacting RNAs (Figure 6A, B). A common *in vitro* method is RNA capture, in which the protein of interest is immobilized on an affinity matrix and incubated with *in vitro* transcribed RNA. Bound RNAs are then reverse transcribed, fluorescently labeled, and hybridized to a microarray for computational quantification (45) (Figure 6A). Alternatively, *in vivo* methods such as RNA immunoprecipitation (RIP) and its crosslinking-based variants, such as CLIP, photoactivatable ribonucleoside-enhanced (PAR)-CLIP or enhanced CLIP (eCLIP) use immunoprecipitation to isolate RNA-protein complexes, followed by qPCR or RNA-sequencing to identify the bound RNAs (Figure 6B). While those methods provide valuable insights, like specific binding sites, they require prior knowledge of the protein of interest and are therefore limited in detecting unexpected interactions.

In contrast, RNA-centric approaches allow the identification of novel interaction partners for a specific RNA of interest, enabling a broader, unbiased view of RNA-protein interactions (Figure 6C, D). Most of these methods rely on crosslinking and probe-based affinity purification followed by mass spectrometry (MS) analysis of the precipitated proteins (10). Like the protein-centric approaches, they can be performed either *in vivo* or *in vitro*.

For *in vivo* identification of lncRNA-interacting proteins, methods like chromatin isolation by RNA purification (ChIRP), capture hybridization analysis of RNA targets (CHART), or RNA antisense purification MS (RAP-MS) are commonly used (Figure 6C). Briefly, in these methods cells are crosslinked, lysed, and lncRNA-protein complexes pulled down using biotinylated antisense probes targeting the lncRNA of interest. The associated proteins are then identified by Western blot or MS (46). While these approaches preserve physiological lncRNA-protein interactions, they are technically demanding, require large amounts of starting material, and involve extensive optimization (37,44).

To circumvent these limitations, *in vitro* strategies offer a simplified alternative (Figure 6D). Here *in vitro* transcribed RNAs are chemically tagged, commonly with biotin, or equipped with RNA aptamers such as the streptavidin-binding S1 aptamer (47). The tagged RNA is immobilized on an affinity matrix and,

Introduction

incubated with protein extracts. After washing, the RNA-protein complexes are eluted and analyzed by Western blot or MS (37,44).

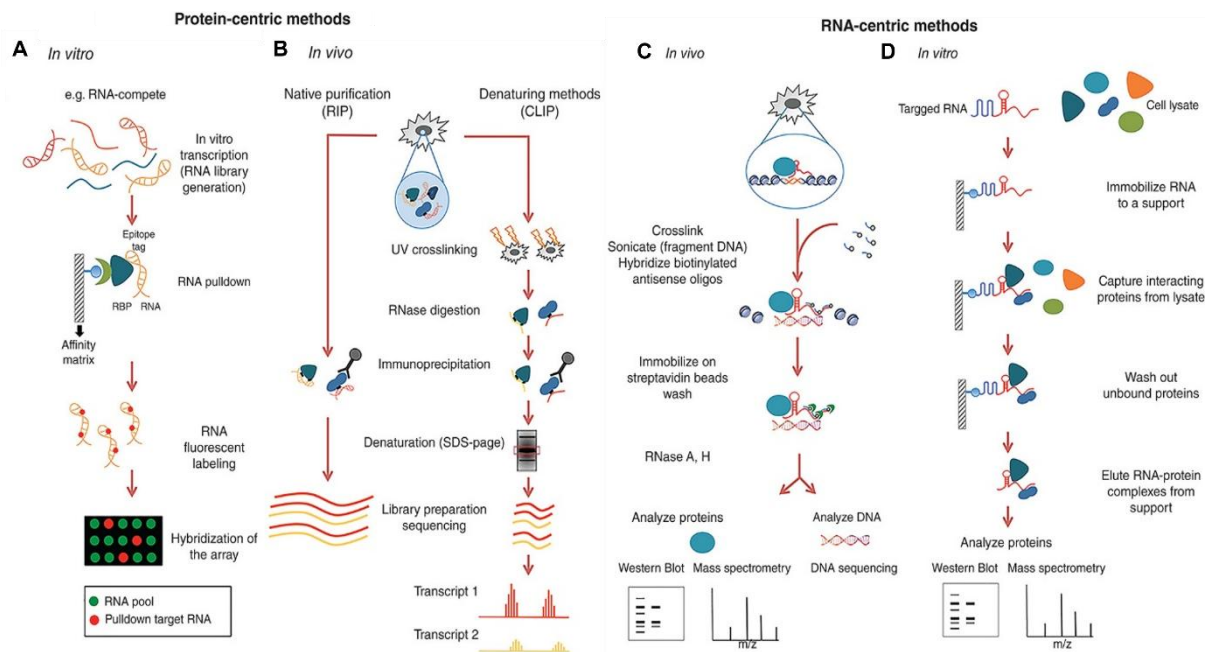


Figure 6 Experimental strategies to study lncRNA-protein interactions

Schematic overview of two complementary approaches used to identify RNA-protein interactions. (A, B) Protein-centric approaches aim to detect RNA molecules that interact with a specific protein of interest using *in vitro* (A) or *in vivo* (B) immunoprecipitation-based techniques. (C, D) RNA-centric methods are designed to identify proteins that associate with a selected RNA of interest, either *in vivo* using probe-based pull-downs (C), or *in vitro* with tagged synthetic RNAs (D). Edited figure from Marchese, D., et al. (2016)

The lncRNA ANRIL

The antisense non-coding RNA in the INK4 locus ANRIL (CDKN2B-AS1), was first identified in 2007 during the characterization of a large germ-line deletion in a French family with a history of melanoma and neural system tumor syndrome. It is transcribed antisense to the CDKN2B/CDKN2A/ARF gene locus at 9p21.3 (48). This mutation-prone hotspot has been implicated in a wide range of diseases, including various cancers and cardiovascular disorders, such as coronary atherosclerotic heart disease (CAD) and type 2 diabetes (49) (Figure 7).

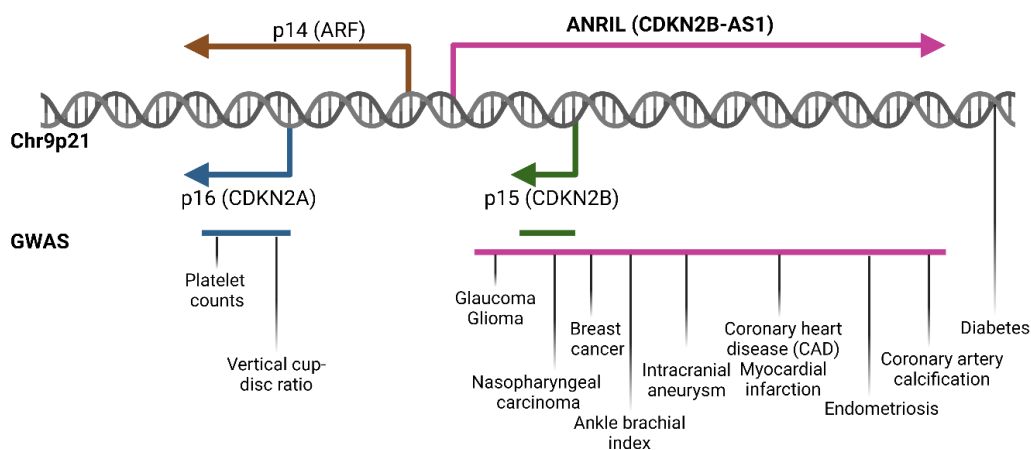


Figure 7 CDKN2A/B-ANRIL locus and associated diseases

The upper panel illustrates the genome organization of the human CDKN2A/B locus on Chromosome 9p21.3 ANRIL (CDKN2B-AS1) is transcribed antisense to the tumor suppressor p15 (CDKN2B). In addition to p15, two other tumor suppressors are transcribed from this locus, p16 (CDKN2A) and p14 (ARF). The lower panel shows the spectrum of diseases linked to SNPs located at 9p21.3, based on findings from genome-wide association studies (GWAS). Figure based on Tritto, V., et al. (2019) and Holdt, L. M. and D. Teupser (2013).

ANRIL is a lowly expressed lncRNA transcribed by RNAPII (50) (Figure 8A), consisting of 21 exons, which are alternatively spliced to generate multiple linear and circular isoforms (51) (Figure 8B). Due to clade-specific evolution, the complete set of 21 exons is present only in simians, with degeneration of exonic sequences observed in rodents, limiting the applicability of murine models to study ANRIL interactions (52-54). Several studies suggest that different isoforms form distinct functional units (54), may allowing ANRIL to interact with diverse proteins, RNA molecules, and genomic regions, thereby influencing multiple biological pathways. Most of its linear isoforms are located in the nucleus, while the circular isoforms tend to be located in the cytoplasm (Figure 8C) (53,55).

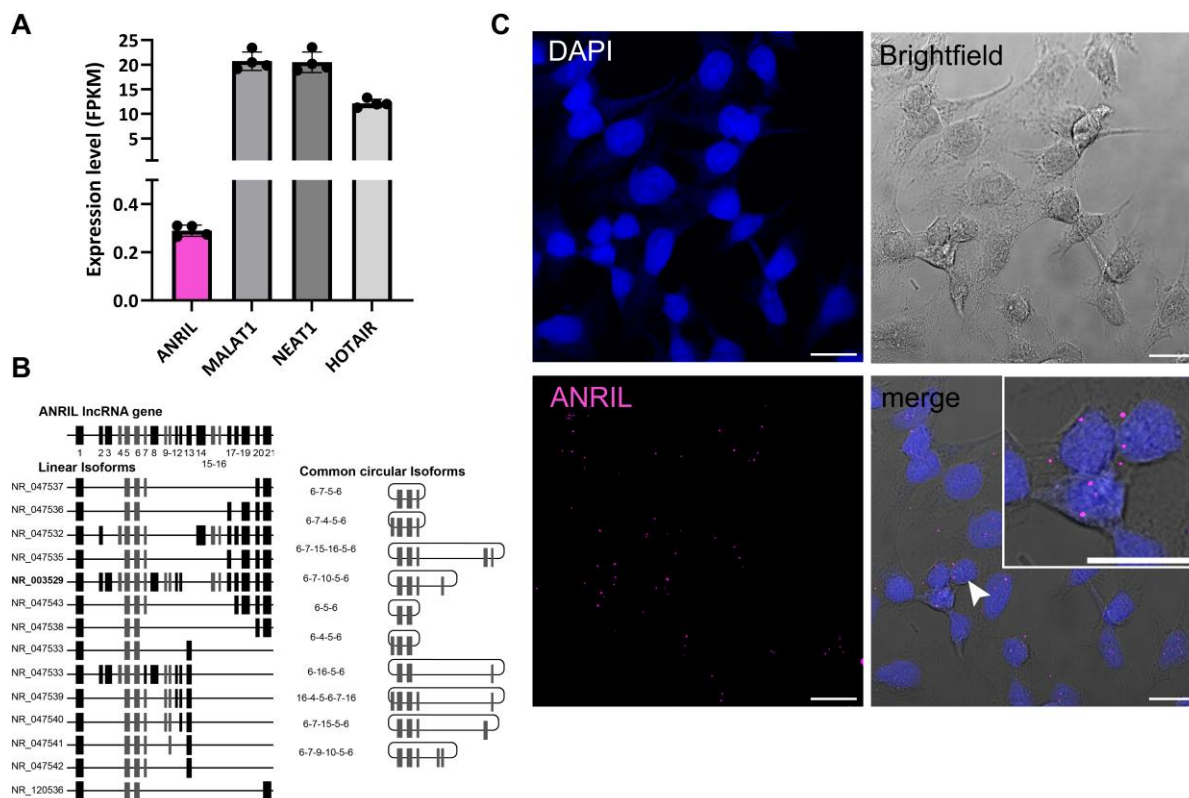


Figure 8 The lncRNA ANRIL - expression, isoforms and localization

(A) Expression level of ANRIL (CDKN2B-AS1) and other lncRNAs in HeLa Kyoto cells, treated with RLuc. Values represent calculated FPKM values (n=4). (B) Overview of known ANRIL isoforms. Exons that occur only in linear isoforms are shown in black, and exons that also occur in circular isoforms are colored gray. Figure based on Kong, Y., et al. (2018). (C) Confocal microscopy images of ANRIL expression in untreated HeLa Kyoto cells (scale bar 15 μ m).

The nuclear localization of the linear transcripts suggests their involvement in gene regulation, whereas the cytoplasmic localization of circular isoforms point to a potential roles in post-transcriptional regulation (53).

Studies have shown that ANRIL modulates gene expression through chromatin modifications and transcriptional regulation, primarily by interacting with miRNAs or RBPs. The NPInter (v5.0) ncRNA interaction database currently lists 63 ANRIL protein-interactors (56). Furthermore, a study from 2021 identified 188 direct gene targets of ANRIL (57), suggesting a broad spectrum of biological functions.

At the chromatin level, ANRIL regulates gene expression at its own locus and at distant genomic sites. At its own locus, ANRIL promotes epigenetic silencing through mediating the addition of H3K27me3 methylation and H2AK119Ub ubiquitination at the CDKN2A/ARF/ANRIL promoter (54). This occurs through interactions with key components of PRC1 and 2. Specifically, SUZ12 of PRC2 interacts with the 5' region of ANRIL (58) and CBX7 with its 3' region (59). This interaction mediates the suppression of p14ARF, p15INK4B (CDKN2B), and p16INK4A (CDKN2A) (60) (Figure 9). CDKN2A and CDKN2B encode

Introduction

cyclin-dependent kinase (CDK) inhibitors that block the interaction between CDK4/6 and Cyclin D, key regulators of the cell cycle (61). This inhibition prevents the activation of the transcription factor E2F1, thereby halting the expression of genes required for G1/S-phase transition. In contrast, ANRIL-mediated repression of CDKN2A/B relieves this inhibition, promoting cell cycle progression (54). Additionally, ARF contributes to cell cycle control by inhibiting MDM2 ubiquitin ligase, resulting in the stabilization of the tumor suppressor p53, inducing G1/S cell cycle arrest and apoptosis (62). The repression of ARF by ANRIL promotes cell cycle progression and cell survival (54). The repression of key cell cycle inhibitors is considered a major risk factor in cancer development, positioning ANRIL as a critical oncogenic regulator that drives unchecked cell division and reduced apoptosis. High ANRIL levels have been associated with a wide range of cancers, including ovarian (63,64) and breast cancer (65), promoting proliferation, migration, invasion and metastasis (53).

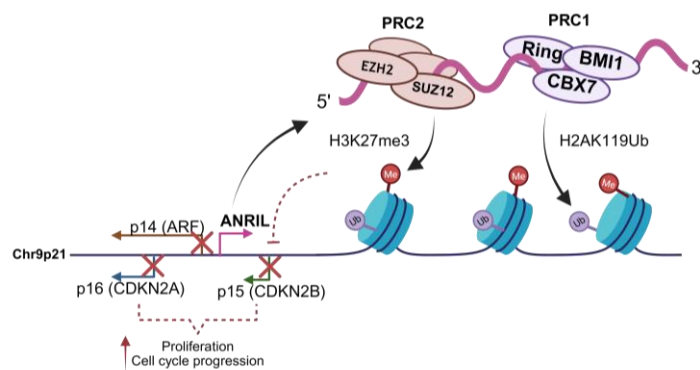


Figure 9 ANRIL-mediated histone modifications regulate the 9p21 locus

ANRIL interacts with SUZ12 of the PRC2 complex and CBX7 of the PRC1 complex, leading to transcriptional repression of the 9p21 locus. The repression is mediated by the deposition of repressive histone marks, H3K27me3 by PRC2 and H2AK119ub by PRC1. This promotes increased proliferation and cell cycle progression. Figure based on Sanchez, A., et al. (2023).

Similarly, ANRIL can induce epigenetic modifications at distant genomic loci in a PRC-dependent manner. For example, PRC2-mediated repression of the transcription factor KLF2 has been shown to promote proliferation and inhibits apoptosis in non-small lung cancer (66) and hepatocellular carcinoma (67). ANRIL also functions as a scaffold for WDR5 and HDAC3 increasing the expression of NOX1 and thereby promoting the phenotypic transition of human aortic smooth muscle cell, contributing to the progression of CAD (68).

Beyond chromatin remodeling, ANRIL also regulates inflammatory gene expression, by guiding the transcription factor Ying Yang 1 (YY1) to the promoters of interleukin (IL)-6 and IL-8, thereby further influencing CAD progression (69). A study from 2016 performed in human umbilical vein endothelial cells (HUVECs), showed that TNF- α stimulation activates and induces nuclear translocation of the NF- κ B subunit p65 (RELA) through its phosphorylation at serin 536 (69). Activated p65 binds to the

Introduction

promoter of ANRIL, upregulating its expression. RIP analysis further identified the binding between ANRIL and YY1, and CHIP-sequencing of YY1, along with ChIRP analysis of ANRIL, revealed co-occupancy at the promoter regions of IL-6 and IL-8. ANRIL knockdown reduced the binding of YY1 at these sites, supporting its role as a transcriptional guide (69) (Figure 10).

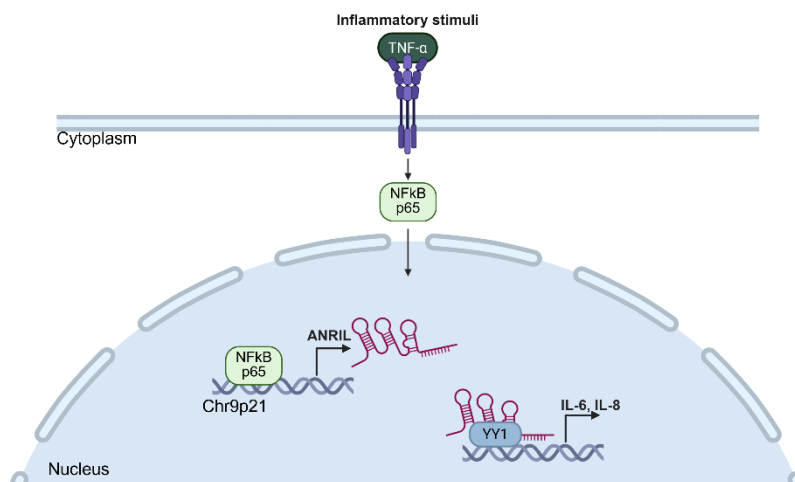


Figure 10 ANRIL regulating inflammatory response

ANRIL regulates inflammatory response. The inflammatory stimulus TNF- α triggers p65 activation and nuclear translocation, which induces ANRIL upregulation. ANRIL then guides the transcription factor YY1 to the promoter region of proinflammatory cytokines IL-6 and IL-8. Figure based on Zhou, X., et al. (2016).

Additionally, a circular isoform of ANRIL (circANRIL), comprising exons 5 to 7, acts as a protective factor during atherosclerosis by regulating ribosome biogenesis in atherosclerotic plaques (1,70). Specifically, circANRIL binds to pescadillo homologue 1 (PES1), disrupting the formation of the PeBoW complex. This complex is essential for precursor ribosomal RNA processing (71,72). The impaired function of the PeBoW causes accumulation of intermediate pre-rRNA forms, triggering nucleolar stress, which in turn activates the tumor suppressor gene p53 inducing cellular apoptosis and inhibiting proliferation (70).

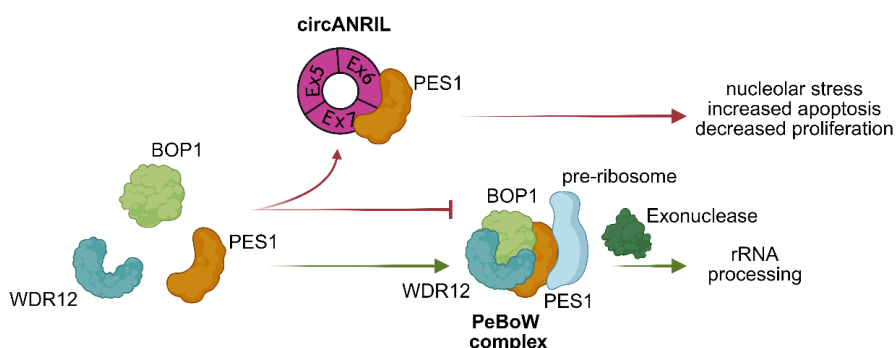


Figure 11 ANRIL regulates rRNA processing through interactions with PeBoW complex member PES1

Molecular mechanism of circANRIL (Exon 5-7) regulating ribosomal biogenesis. CircANRIL blocks the formation of PeBoW complex, by binding to PES1. The impaired function of PeBoW, leads to accumulation of intermediate pre-rRNA and the induction of nucleolar stress, increased apoptosis and decreased proliferation. Figure based on (1) Zhang, Z., et al. (2023)

Introduction

Circular isoforms of ANRIL have also been shown to interact with PRC components to regulate the INK4 locus (CDKN2A/B/ARF), shifting from gene repression to activation depending on cellular state (73). In RAF1 oncogene-induced senescence cells, the circANRIL isoform containing Exons 16-15 is upregulated. This increase reduces H3K27me3 levels at the CDKN2A/B promoters by sequestering EZH2 away from the locus, inducing the expression of CDKN2A/B. Postulating that the ratio of circANRIL and PRC proteins modulates ANRIL function, switching from a repressor to an activator in senescent cells (73).

Despite significant advances in understanding the molecular functions of ANRIL across various diseases, its full interactome remains largely unexplored. The identification of 188 direct targets, however, suggests a wide spectrum of possible regulatory mechanisms (57). Until now, most studies have relied on protein-centric methods such as CLIP, CHIP, RIP to investigate specific RBP interactions with ANRIL. Using an unbiased RNA-centric approach could uncover previously unrecognized ANRIL-binding proteins and provide insights into its broader functional potential.

In recent years, studies have shown that ANRIL expression is dynamically regulated in response to viral infections, including the oncogenic-viruses HTLV and KSHV, as well as SARS-CoV-2. In cells infected with the retrovirus human T-cell leukemia virus type I (HTLV) ANRIL expression is upregulated. HTLV causes T-cell leukemia (ATL), a malignancy unique in CD4⁺T cells. Song et al. demonstrated that ANRIL promotes the proliferation of ATL cells by formation of a ternary complex with EZH2 and p65, thereby enhancing p65 DNA-binding activity and NF- κ B signaling (74).

In contrast, infection with the gammaherpesvirus Kaposi's sarcoma-associated herpesvirus (KSHV) drastically downregulates the expression of ANRIL (75). KSHV, the causative agent of Kaposi's sarcoma, which is a highly prevalent cancer in AIDS (75,76), reduces ANRIL level through post-transcriptional mechanisms. This involves KSHV-encoded miRNAs and latency-associated proteins vCyclin and vFLIP, which presumably suppress ANRIL to evade the host immune response by blocking ANRIL-mediated induction of IL-6 and IL-8 (75).

Additionally, a recent study reported increased ANRIL expression in blood samples from patients with severe and moderate cases of severe acute respiratory syndrome coronavirus 2 (SARS-CoV-2) infections (77).

As viral infections significantly alter host gene expression, lncRNAs have emerged as critical players in modulating the host-virus interactions (78).

The role of lncRNAs in viral infections

Emerging evidence demonstrates the essential role of lncRNAs in the response to viral infections. They contribute to a wide spectrum of immune functions, ranging from immune cell development to antiviral effector responses and can also act as proviral factors (26,79). This regulation can occur through both interferon (IFN)-dependent or -independent mechanisms (80).

A recent publication demonstrated, that the virus-induced lncRNA-BTX promotes viral replication independent of the IFN pathway (81). The nuclear lncRNA-BTX is upregulated in response to viral nucleic acids in macrophages and interacts with the RBPs DHX9 and ILF3. DHX9, a nuclear DNA helicase, typically translocates to the cytoplasm during infection to support viral replication (82,83). This process is mediated by JMJD6 demethylation of DHX9. The lncRNA-BTX strengthens the interaction between DHX9 and JMJD6, thereby enhancing its cytoplasmic localization. Conversely, lncRNA-BTX restricts ILF3 antiviral role by enhancing its interaction with ILF2, thereby preventing its usual cytoplasmic translocation (81). Similarly, the lncRNA NRAV has been shown to facilitate viral replication. A 2014 study found that NRAV overexpression in H1N1-infected human alveolar epithelial cells (A549) enhances viral replication and virulence, while its knockdown suppressed viral replication (84). NRAV acts by interferon-stimulated genes through histone modifications at their transcription start sites. The authors suggested that the increased downregulation of NRAV in response to H1N1 is part of the host's antiviral innate immune response (84).

Although certain lncRNAs act independently of INF signaling, the majority are either regulated by IFNs or modulate key steps within the IFN pathway (85).

Type I interferon signaling in response to viral infections

The innate immune system serves as the host's first line of defense against a wide range of pathogens, including viruses (86-88). Recognition of pathogen-associated molecular patterns (PAMPs), such as viral nucleic acids, by pattern recognition receptors (PRRs) trigger a rapid and non-specific immune response (89,90). Among these receptors, the retinoic acid-inducible gene I (RIG-I)-like receptors (RLRs), including RIG-I and melanoma differentiation associated gene 5 (MDA-5), are key sensors of viral infection (88,90) (Figure 12A). They can detect immunostimulatory RNAs via their C-terminal (CTD) and central helicase domains (91,92), while their two N-terminal caspase activation and recruitment domains (CARD) initiate downstream signaling (89). Upon RNA binding, RLRs undergo oligomerization and interact with the CARD domain of the mitochondrial antiviral-signaling protein (MAVS) (93-95), which activates TANK-binding kinase 1 (TBK1) and I κ B kinase- ϵ (IKK ϵ) (96,97). These kinases in turn

Introduction

activate interferon regulatory factors, such as IRF3 and IRF7, and NF- κ B, leading to the induction of type I IFNs and other antiviral or immunoregulatory genes (98-100) (Figure 12A,B).

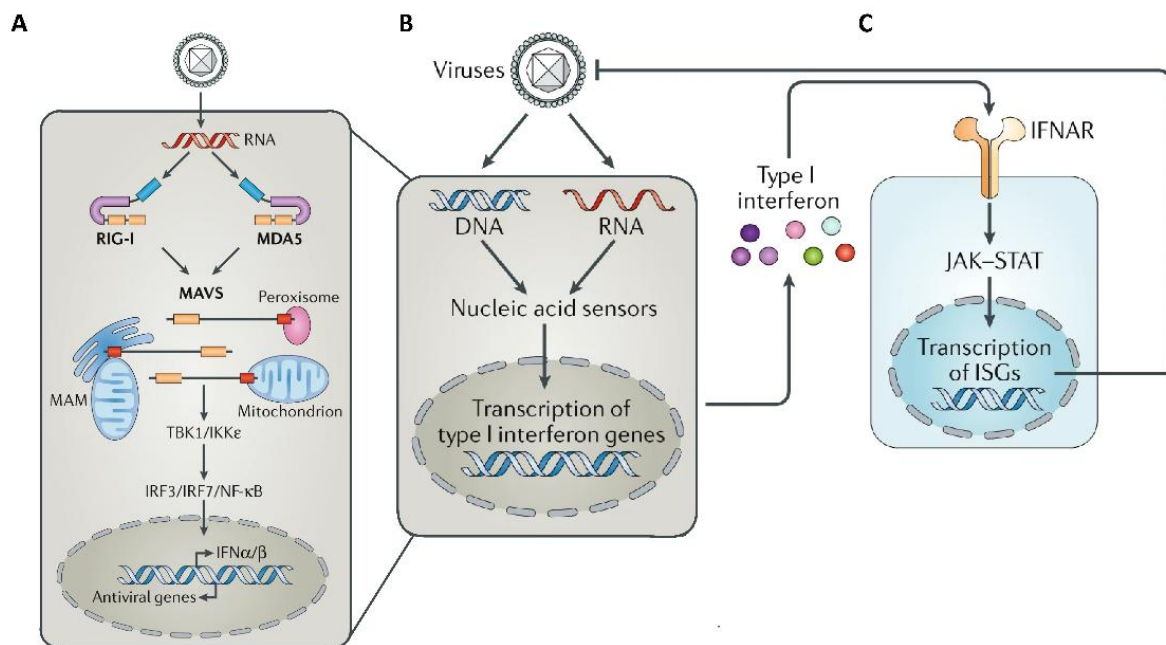


Figure 12 Type I IFN Production and Signaling

(A, B) RIG-I and MDA5 sense viral RNAs and activate MAVS. MAVS trigger TBK1 and IKK ϵ , leading to the activation of IRF3, IRF7, and NF- κ B, which induce the expression of IFNs. (C) Secreted type I IFNs bind to the IFNAR receptor on neighboring cells, activating JAK-STAT signaling pathway. This induces the expression ISGs, many of which have direct antiviral functions. Edited figure from Rehwinkel, J. and M. U. Gack (2020)

IFNs are antiviral cytokines classified into three subtypes: type I, type II and type III (87,101). Among them, the type I interferons, such as IFN- α , IFN- β , are produced by almost all nucleated cells in response to viral infection (86,102) (Figure 12B). Upon secretion, type I IFNs bind to their heterodimeric IFN- α/β receptor (IFNAR), which is composed of the subunits IFNAR1 and IFNAR2 (101) (Figure 12C). The binding activates the canonical JAK-STAT signaling pathway, through the phosphorylation of the tyrosine kinases Janus Kinase 1 (JAK1) and Tyrosin Kinase 2 (TYK2). Activated JAK1 and TYK2 subsequently phosphorylate the transcription factors STAT1 and STAT2 (STAT; signal transducer and activator of transcription) (103), which in turn form a complex with the IFN-regulatory factor 9 (IRF9), known as the IFN-stimulated gene factor 3 (ISGF3). The ISGF3 complex then translocates to the nucleus, where it binds to IFN-stimulated response elements (ISREs) in the DNA, driving the expression of IFN-stimulated genes (ISGs) (104).

Multiple studies suggest that over 450 ISGs exist, with some exhibiting broad antiviral activity, while others act in a virus-specific manner. ISGs modulate viral infections by targeting key steps of the viral

Introduction

life cycle (105,106). Based on their function, ISGs can be broadly categorized into three groups: antiviral effectors, negative regulators and positive regulators of IFN signaling (102).

Antiviral effectors include classical ISGs such as MX1, IFITs, OAS and EIF2AK2, which directly inhibit viral replication, degrade viral RNA, or interfere with translation. While positive regulators like IRFs and STATs, enhance the IFN signaling and amplify the antiviral response (102,105). For instance, the transcription factor IRF1 is induced during primary IFN-response and subsequently translocates to the nucleus to promote a secondary wave of ISG transcription (102,107). In contrast, negative regulators are essential for preventing excessive or prolonged type I IFN signaling, which could otherwise lead to chronic inflammation or autoimmune pathology (108,109). One example is the ubiquitin specific peptidase 18 (USP18), that negatively regulates type I IFN signaling by binding STAT2, blocking JAK1 activation at IFNAR2 (110,111).

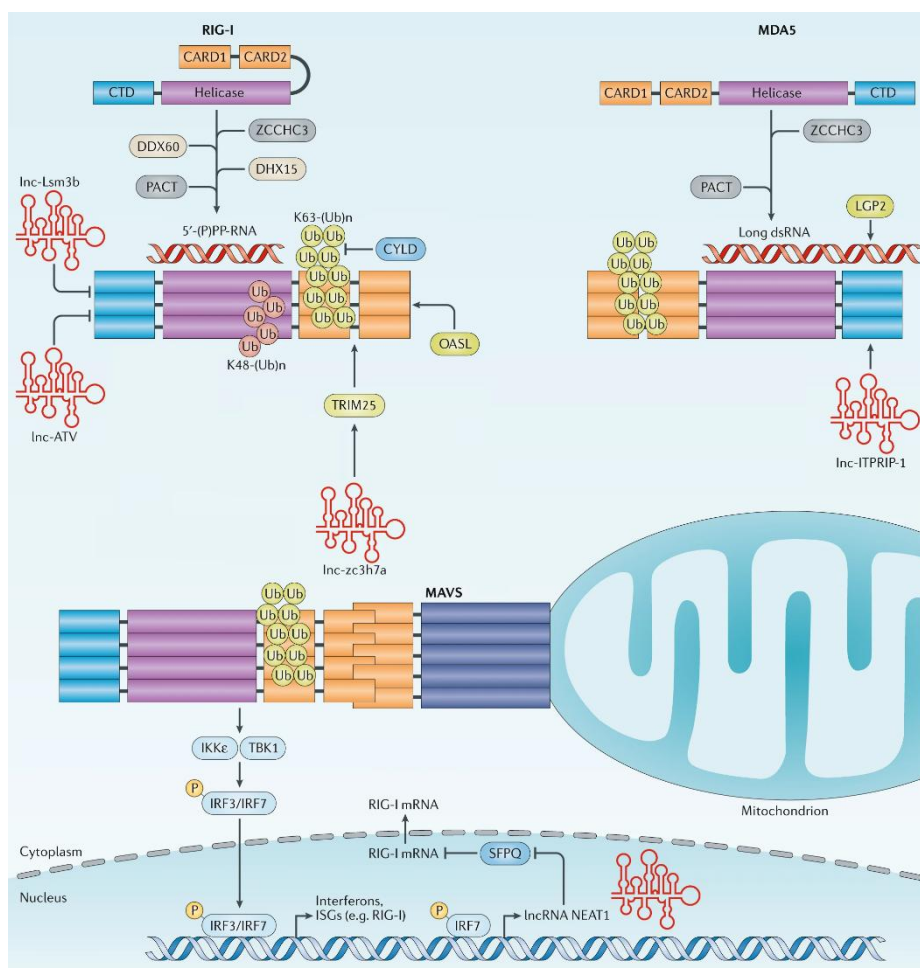


Figure 13 Regulation of RIG-I- and MDA5-mediated type I interferon signaling by lncRNAs

lncRNAs modulate RIG-I-like receptor (RLR) signaling either indirectly by altering the expression of key pathway components, like RIG-I, or directly through physical interactions with RLRs or their co-factors, such as TRIM25. These interactions can enhance or suppress type I IFN responses during viral infection. Edited figure from Rehwinkel, J. and M. U. Gack (2020).

Introduction

The type I INF signaling pathway is also regulated by virus-induced lncRNAs (Figure 13). For instance, in macrophages infected with vesicular stomatitis virus (VSV), the lncRNA *lnczc3h7a* is upregulated and promotes RIG-I signaling by acting as a scaffold for TRIM25 and RIG-I, facilitating RIG-I ubiquitination and the downstream pathway activation (112). In contrast, VSV also induces the expression of the lncRNA *lncLsm3b*, which dampens RIG-I signaling by competing with viral RNAs for RIG-I binding. This prevents RIG-I's conformational shift and activation, thereby suppressing downstream signaling during later stages of infection, potentially contributing to immune homeostasis (113). During Hantaan virus (HTNV) infection, the expression of the lncRNA *NEAT1* is upregulated through a RIG-I/IRF7-dependent positive feedback loop. Specifically, IRF7 induces the expression of *NEAT1*, which then in turn relocates the transcriptional inhibitor *SFPQ* from the RIG-I promoter to nuclear paraspeckles. This leads to increased expression of RIG-I promoting type I IFN response suppressing HTNV (114,115). Similarly, MDA5 signaling can be regulated by lncRNAs. Hepatitis C (HCV) infection induces the expression of the lncRNA *ITPRIP-1*. *ITPRIP-1* stabilizes MDA5 by binding to its CTD, stabilizing the protein and promoting its oligomerization and RNA-binding, ultimately enhancing viral RNA recognition and inhibiting HCV replication (116).

Cedar Virus

The *Paramyxoviridae* family, part of the *Mononegavirales*, consists of enveloped nonsegmented negative-sense, single-stranded RNA viruses. It is further divided into nine subfamilies, namely *Avulavirinae*, *Feraresvirinae*, *Glossavirinae*, *Ichthysvirinae*, *Metaparamyxovirinae*, *Rubulavirinae*, *Skoliivirinae*, and the largest subfamily *Orthoparamyxovirinae*, based on the most recent release of the International Committee on Taxonomy of Viruses (MSL40) (Figure 14). Within *Orthoparamyxovirinae*, the fruit bat-born genus *Henipavirus* includes the highly pathogenic, zoonotic biosafety level 4 (BSL-4) viruses Hendra (HeV) and Nipah (NiV), as well as the non-pathogenic Cedar virus (CedV) (117,118). CedV was first identified in 2012 during routine surveillance for HeV in Queensland flying foxes. Urine samples collected in 2009 from Cedar Grove, South East Queensland, showed atypical viral infection behavior and sequences distinct from HeV (117). Subsequent genomic characterization revealed that CedV shares the closest genetic relationship with HeV and NiV among the currently known *Henipavirus* genus (Figure 14).

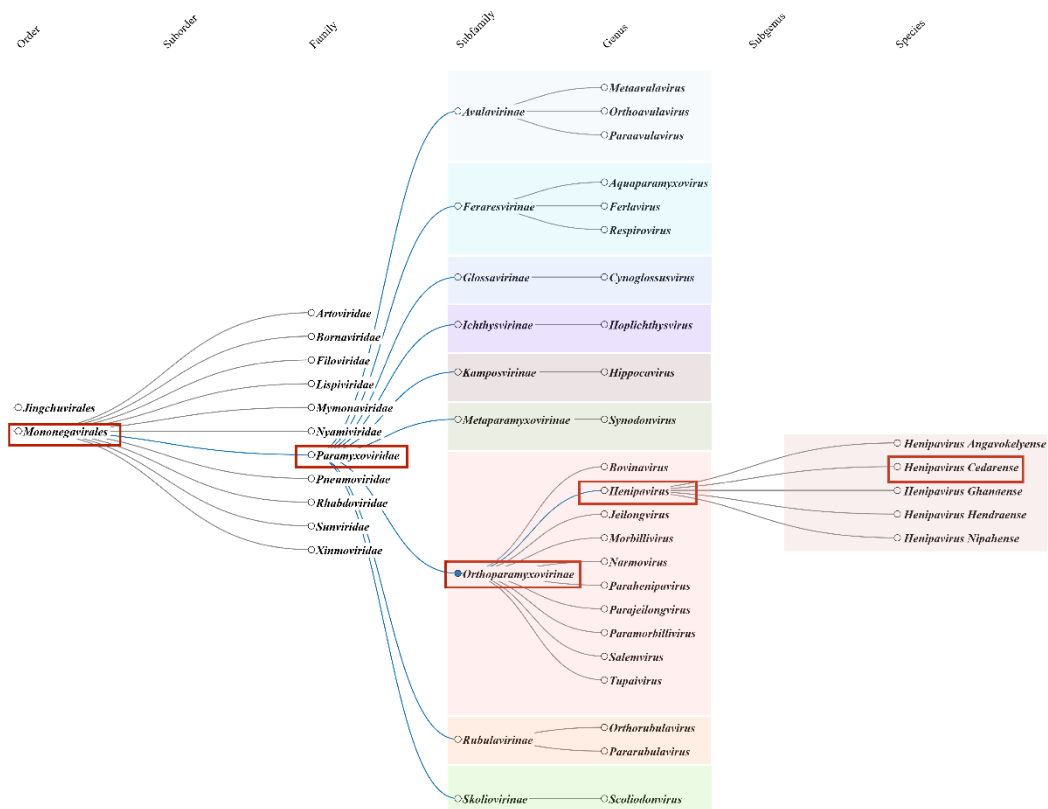


Figure 14 Phylogenetic tree of the family Paramyxoviridae

Phylogenetic tree of the *Paramyxoviridae* family, based on the most recent International Committee on Taxonomy of Viruses (ICTV) Master Species List (MSL) MSL40 (release: 2024-2025).

Introduction

The genome of CedV comprises approximately 18,162 nucleotides of single-stranded negative-sense RNA and encodes for seven proteins from six genes. Its gene order is conserved across the *Paramyxoviridae* family and, in the *Henipavirus* genus, follows a 3' to 5' direction: nucleoprotein (N), phosphoprotein (P), matrix protein (M), transmembrane-anchored fusion protein (F), glycoprotein (G), and the RNA-dependent RNA polymerase (L) (117) (Figure 15). Structurally, the viral genome forms a linear ribonucleoprotein (RNP) core, containing the L, N and P-proteins. The RNP is surrounded by the M protein, which lines the inner surface of the viral envelope. Embedded in the envelope are the two surface proteins G and F, which mediate host cell entry and membrane fusion (118) (Figure 15).

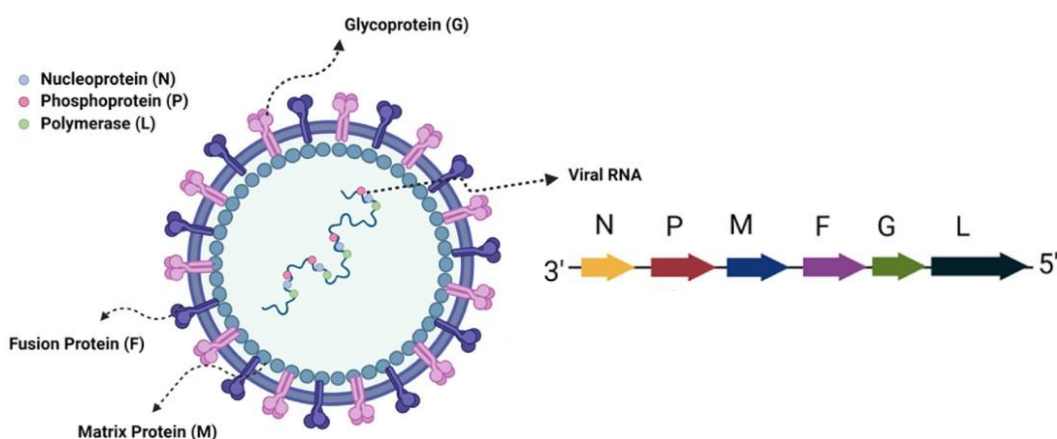


Figure 15 The structure and viral genome organization of Cedar, Nipah and Hendra virus

The *Henipavirus* structure. The nucleoprotein (N), phosphoprotein (P), and polymerase (L) proteins bind the negative-sense RNA genome to form the ribonucleoprotein (RNP) complex. The viral envelope consists of the matrix protein (M), and the two surface proteins glycoprotein (G) and fusion protein (F) which are embedded in the lipid envelope. Edited figure from Sabir, A. J., et al. (2024)

A hallmark of paramyxovirus infection is the formation of large multinucleated cells, or syncytia (119) (Figure 16A). This cell-cell fusion is mediated by the viral surface glycoproteins G and F. Upon binding of the G protein to ephrin receptors on neighboring host cells, a conformational change triggers the activation of the F protein (120-122) (Figure 16C). Cleavage of F by host proteases exposes a fusion peptide (Figure 16B), which is inserted into the target membrane, resulting in membrane fusion and syncytium formation (119,123,124) (Figure 16). Interestingly, CedV exhibits markedly lower fusogenicity compared to HeV and NiV, attributed to unique regulatory features at the G protein head/stalk interface, limiting membrane fusion and reduced syncytium formation, possibly contributing to its lower pathogenicity (125).

Introduction

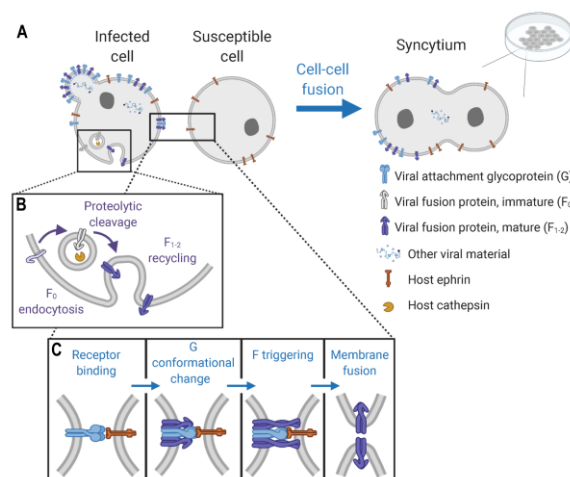


Figure 16 Molecular mechanism of henipavirus-induced syncytia

(A) Syncytia are large multinucleated cells formed through the fusion of virus-infected cells with neighboring susceptible cells. (B) The viral fusion protein F undergoes activation through cleavage by host proteases within endosomal compartments. (C) Virus-cell membrane fusion is initiated by binding of viral glycoprotein G and F proteins to ephrin receptors on host cells. Edited figure from Gamble, A., et al. (2021).

A key distinction between CedV and other paramyxoviruses is its inability to express additional nonstructural proteins from the P gene (117). In most paramyxoviruses, RNA editing introduces non-templated guanosine residues into the P gene, leading to the production of the V protein through the insertion of a single guanosine, and the W protein through the insertion of two guanosine residues (126,127). CedV, however, so far lacks evidence of such RNA editing sites and translates only the C protein, similar to other paramyxoviruses, from an alternative reading frame within the P gene (117) (Figure 17).

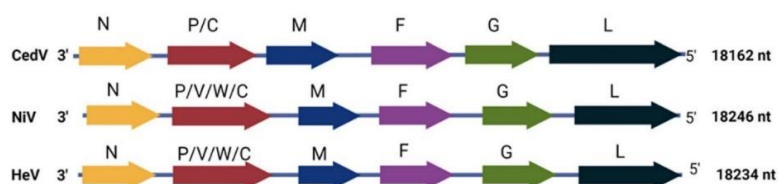


Figure 17 Comparison between different Henipavirus genomes

Comparison of the genome organization of CedV, NiV and HeV. The P gene of NiV and HeV encodes, additionally to the C protein, the proteins V and W through mRNA editing. Adapted from Sabir, A. J., et al. (2024)

Notably, the viral proteins V and W play a central role in antagonizing the host's IFN response. In particular, the V proteins of NiV and HeV V target multiple components of the IFN signaling pathway (128-131) (Figure 18). The C-terminal domain of both V protein can bind directly to MDA5, disrupting its RNA-binding ability and multimerization, thereby blocking downstream IFN signaling (132-135) (Figure 18A). Additionally, the NiV V protein maintains MDA5 in an inactive phosphorylated state by inhibiting its dephosphorylation via PP1 α/γ phosphatases (136), and further impairs MDA5 function by

Introduction

altering its helicase fold and dynamics (137). NiV V also interferes with RIG-I signaling by preventing TRIM25-mediated RIG-I ubiquitination, thereby blocking its activation and downstream signaling via MAVS (138). Beyond the upstream sensing, the V proteins also inhibit downstream IFN signaling (131) (Figure 18B). Both HeV and NiV V as well as NiV P proteins bind to STAT1 and STAT2 forming high-molecular weight complexes, blocking their phosphorylation and nuclear translocation, thereby preventing the induction of ISGs (139-141). Additionally, the W protein of NiV is also able to form similar inhibitory complexes in the nucleus and blocks the activation of IRF3 (142). Through those diverse mechanisms, HeV and NiV can efficiently suppress the host's antiviral defenses, contributing to their high pathogenicity (128).

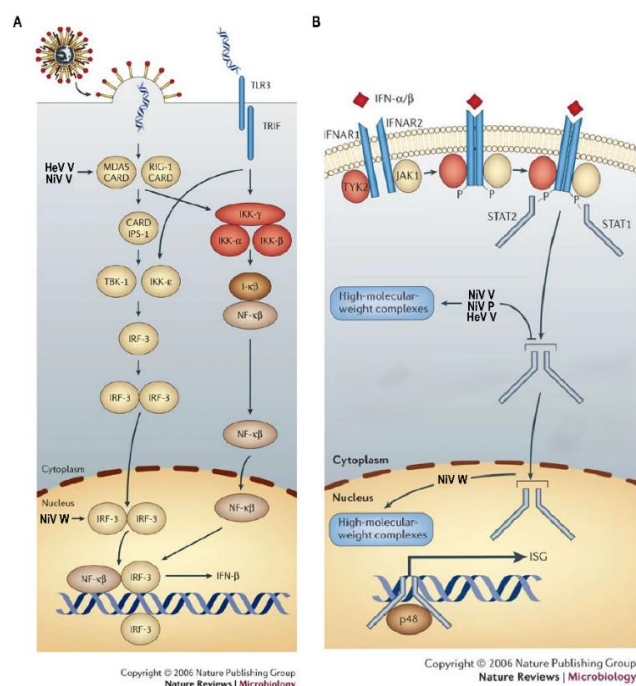


Figure 18 Antagonism of type I IFN signaling pathways by HeV and NiV proteins

(A) Schematic illustration of how V and W proteins of Hendra virus (HeV) and Nipah virus (NiV) interfere with IFN induction. The viral V proteins of both viruses inhibit activation of the cytoplasmic viral RNA sensors MDA5 and RIG-I. The viral W protein of NiV blocks the activation of IRF-3 in the nucleus. (B) Graphical representation of the inhibition of downstream IFN signaling by HeV and NiV. The NiV V and P proteins, as well as the HeV V protein, form high-molecular weight complexes with STAT1 and STAT2 in the cytoplasm, thereby preventing their phosphorylation and nuclear translocation. Additionally, the viral W protein of NiV forms similar inhibitory complexes with STAT1 in the nucleus. Edited figure from Eaton, B. T., et al. (2006)

The absence of V and W proteins in CedV likely contributes to its reduced virulence and pathogenicity, as it limits CedV ability to counteract the host's immune response (117,118). This is further supported by the inability of CedV P proteins to bind to STAT1 or STAT2, making them unable to effectively inhibit STAT-mediated IFN signaling (143). As a result, CedV remains the only known non-pathogenic henipavirus that can be safely studied under BSL-2 conditions, making CedV a valuable model to study henipavirus-host interactions and virus-induced IFN signaling.

Aims of the thesis

Due to its localization in a disease-associated hotspot, the lncRNA ANRIL has been extensively studied in cancer and cardiovascular disorders. In addition to its well-characterized action at the 9p21.3 locus, a recent study identified 188 potential ANRIL-regulated targets across the genome, linking ANRIL to the regulation of genes involved in diverse biological processes. Despite significant progress in understanding the regulatory activities of ANRIL, the full spectrum of its protein interactors remains incomplete. Hence, this study aimed to systematically characterize the ANRIL interactome shedding light on the potential molecular mechanisms underlying its regulatory functions.

Results

As ANRIL predominantly localizes in the nucleus (53) (Figure 8C), the immobilized RNA was incubated with nuclear-enriched HeLa extract, allowing potential binding partners to interact with the fragments. Pulldowns for each ANRIL fragment and the control were performed in quadruplicates. Bound proteins were subsequently detected by label-free quantitative (LFQ) proteomics (Figure 19A).

In total 310 interacting proteins across all fragments were identified (Figure 19B). In line with the experimental setup, the majority of these proteins are located in the nucleus (88%) (Figure 20A) and 227 (73%) are specifically annotated to bind RNA (Figure 20B). Of the identified proteins, 64% bound to one (36%) or two (28%) fragments, while the remaining 112 RBPs bound to three or more (Figure 20B), indicating that most of the identified proteins exhibit a target-specific binding preference.

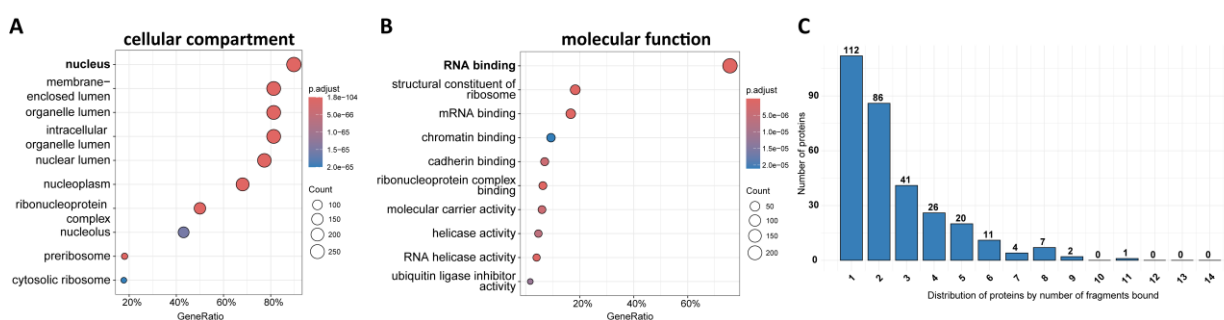


Figure 20 ANRIL-interacting proteins are predominantly located in the nucleus, bind to RNA and exhibit target-specific binding preferences

(A, B) Dot plot illustrating top ten overrepresented Gene Ontology cellular compartment (A) and molecular function (B) terms among the 310 proteins that bind to ANRIL. The color of the dots indicates the p.adjust and the size the number of proteins associated to this term. (C) Distribution of ANRIL-binding proteins by the number of fragments they bound.

Characterization of novel ANRIL-binding protein C7orf50

Among the ANRIL-binding proteins the uncharacterized protein C7orf50 was enriched at the fragments Ex6u7 (Figure 21A) and Ex16u17 (Figure 21B). To validate the binding of C7orf50 to ANRIL, N-terminally tagged GFP-C7orf50 was recombinantly expressed and transfected into HeLa Kyoto cells. The protein lysate was used to repeat the initial RNA pulldown against the fragments Ex16u17, pDEST17 control and additionally empty beads. Subsequent Western blot analysis confirmed the specific binding of GFP-C7orf50 to Ex16u17 in comparison to pDEST17 RNA and empty beads (Figure 21C). *In silico* binding predictions using AlphaFold3 (147) demonstrated that the structured domains of C7orf50 are responsible for the binding to Ex16u17 (Figure 21D) and Ex6u7 (Figure 21E). Specifically, the C-terminal structured alpha-helices of C7orf50 predominantly interact with the 5'-region of Ex16 and the 3'-region of Ex17. This C-terminal structured, contains the conserved RNA-binding domain WKF (DUF2373) (148), which showed a strong interaction with Ex16u17 (Figure 21G) and Ex6u7 (Figure 21H), but not with pDEST17 (Figure 21I). To visualize the cellular localization of C7orf50, recombinant GFP-C7orf50 was

Results

expressed in HeLa Kyoto cells and imaged using fluorescence microscopy, demonstrating its localization in large nuclear condensates, possibly nucleoli (Figure 21J). This is in line with its reported nucleolar localization by the Human Protein Atlas (<https://www.proteinatlas.org/ENSG00000146540-C7orf50>).

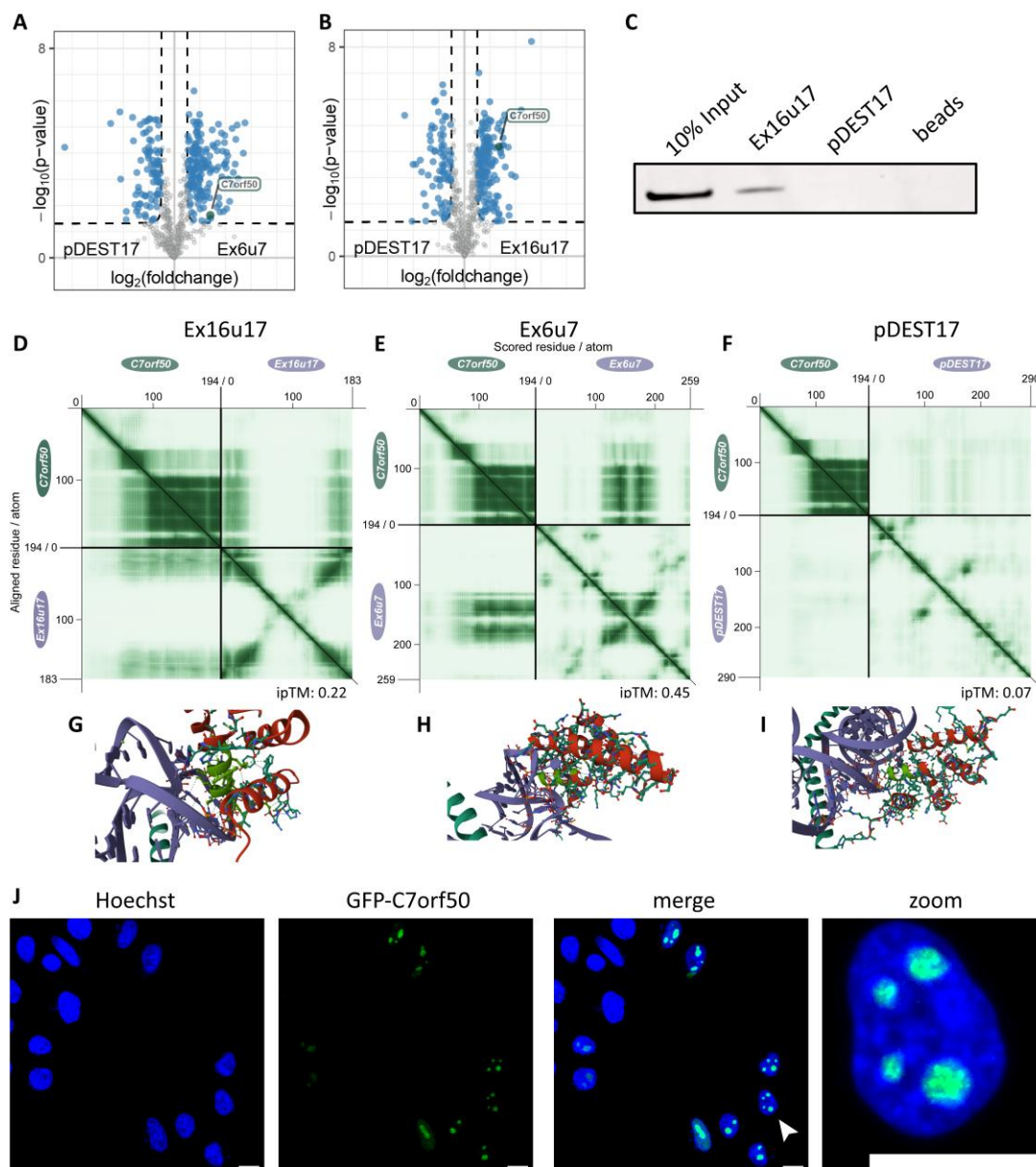


Figure 21 *C7orf50* binds specifically to the ANRIL-fragment Ex16u17 and is localized in nucleolar condensates

(A, B) Volcano plots showing the results of the RNA pull-down with the ANRIL-fragments Ex6u7 (A) and Ex16u17 (B). The identified C7orf50 protein is annotated. The dashed lines represent the enrichment threshold ($FC > 2$, $p\text{-value} < 0.05$ (Welch's t test), $n = 4$). (C) Validation of binding specificity using pull-down assay with lysate of recombinantly GFP-C7orf50 expressing HeLa Kyoto cells against the RNA fragments Ex16u17 and pDEST17 and an empty beads control. Western Blot analysis shows specific binding of GFP-C7orf50 to Ex16u17. The first lane indicates the 10% input control [1 μg]. The following lanes show the pull-down against Ex16u17, pDEST17 and empty beads control against 10 μg extract ($n=1$). (D-F) AlphaFold3 predicted aligned error (PAE) plots of C7orf50 with the ANRIL RNA-fragments Ex16u17 (D), Ex6u7 (E) and pDEST17 control (F). Calculated confidence scores (ipTM; interface predicted template modelling) are indicated below each individual plot. (G-I) AlphaFold3 predicted interaction between C7orf50 (green), WKF-domain (red) including the conserved motif (WRFQKTRQTWLL; green) and Ex16u17 (G), Ex6u7 (H) and pDEST17 control (I) (violet). (J) Fluorescence microscopy of HeLa Kyoto cells transfected with recombinant GFP-C7orf50 at 24 h post-transfection (scale bar 15 μm).

Results

To investigate how C7orf50 could function in cellular networks, GFP-treatment IPs were performed using the recombinantly GFP-tagged C7orf50. Protein-protein interactions (PPIs) were identified by comparing empty GFP-beads and GFP-beads pre-incubated with GFP-C7orf50. Both beads were further incubated with nuclear-enriched HeLa S3 extract and treated with RNase A to digest the RNA (Figure 22A). In total 1128 proteins were detected that presumably interact with C7orf50 (p-value < 0.05 (Welch's t test) and FC > 2). GO enrichment analysis of cellular compartment (GOCC) showed that 125 of the identified proteins are associated with the ribosome (Figure 22C). As nucleoli are the primary site of ribosome biogenesis (149,150), this finding aligns well with the observed cellular localization of GFP-C7orf50 (Figure 21F). Additionally, the 60S ribosomal protein L3 (RPL3) was identified as a protein-protein interactor. A recent study reported that the yeast homolog of C7orf50, Rbp95, interacts with RPL3 during 60S ribosome biogenesis, and that the absence of Rbp95 delays the maturation of early pre-60S particles (151). Furthermore, C7orf50 was found to interact, PES1, a previously described RBP of ANRIL (70), and BOP1, both members of the PeBoW-complex, which is essential for the proper processing and maturation of the large ribosomal subunit 60S (152). These findings further indicate a possible role of C7orf50 during ribosomal biogenesis in humans.

Interestingly, several GOCC-enriched terms fall under the parent term 'extracellular space' (Figure 22C), consistent with a recent publication stating that C7orf50 is secreted into the extracellular space upon cholesterol absorption (153). Reactome pathway analysis further showed that several identified proteins are associated with 'vesicle mediated transport' and 'membrane trafficking' (Supplementary Table 3), suggesting possible C7orf50 interaction partners mediating its secretion. Additionally, some of the identified proteins are associated with cell cycle-related pathways, for example 'cell cycle checkpoints' and 'mitotic metaphase and anaphase' (Supplementary Table 3), among them CDKN2A, a well-known ANRIL-regulated gene (Figure 22A). Further, an increased enrichment of terms as 'antiviral mechanism by IFN-stimulated genes', 'cytokine signaling in immune system' and 'interferon signaling' (Supplementary Table 3) could hint towards potential novel functions of C7orf50.

To identify C7orf50 protein-interactors that are RNA-dependent (RDIs), RNase-treated samples were compared to those treated with RNase inhibitors. This analysis revealed 41 RDIs of C7orf50 (Figure 22B). These RDIs were predominantly enriched in cellular components of the 'ribonucleoprotein complex' and were functional annotated with terms such as 'rRNA processing' (Figure 22D, Supplementary Table 5), reinforcing the role of C7orf50 in ribosomal biogenesis.

To explore which protein-interactions could be attributed to ANRIL, the overlap between the identified C7orf50-PPIs, C7orf50-RDIs and the full ANRIL interactome or specifically the C7orf50-binding ANRIL

Results

fragments Ex6u7 and Ex16u17 was assessed. Notably, 160 proteins (15%) of the C7orf50-PPIs overlapped with proteins identified in the full ANRIL interactome (Figure 22E), including numerous proteins involved in ‘ribosome biogenesis’ and ‘ribosome assembly’ (Supplementary Table 6), possibly hinting towards a connection between ANRIL and C7orf50 in this process. Looking closer at the C7orf50-binding ANRIL fragments, revealed that 125 PPIs (Figure 22F) and 12 RDIs (Figure 22G) showed an overlap with at least one of the fragments, with a substantial number being ribosomal proteins. Interestingly, the PPIs overlapping with Ex6u7 included spliceosomal proteins, such as pre-mRNA processing factors (PRPF), whereas proteins shared with Ex16u17 were more specifically associated with ‘translation’ (Supplementary Table 7).

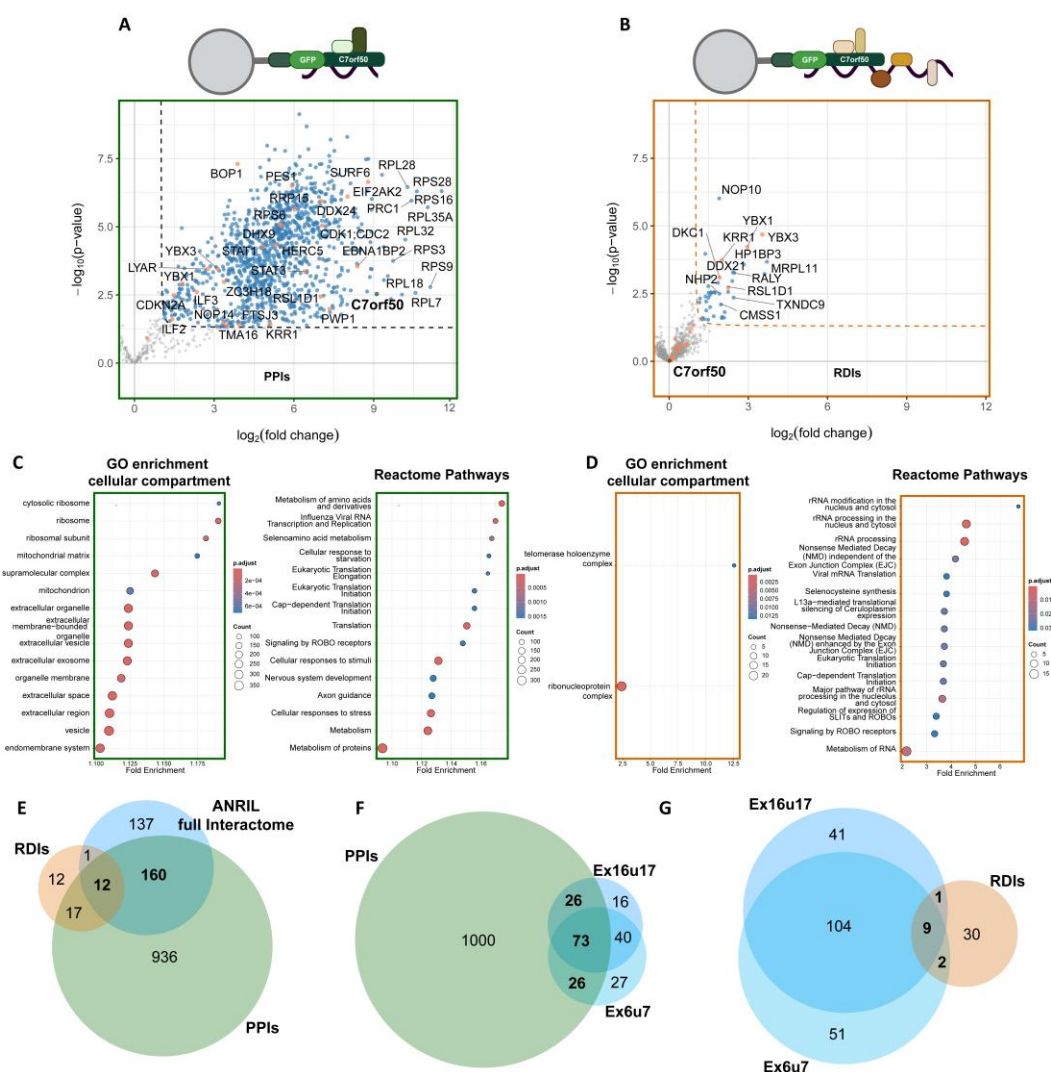


Figure 22 C7orf50 nuclear interactome reveals role in ribosome biogenesis

(A, B) Volcano plots showing the results of the GFP-treatment IP (A) Protein-Protein interactors (PPIs) and (B) RNA-dependent interactors (RDIs) of GFP-C7orf50. C7orf50 is annotated. The dashed lines represent the enrichment threshold (FC > 2, p-value < 0.05 (Welch’s t test), n = 4). (C, D) Dot plots of GO cellular compartment (left) and Reactome Pathways enrichment (right) of PPIs (C) and RDIs (D). Plots include top 15 enriched pathways. A full list of all enriched terms can be found in Supplementary Table 2-5 (E-G) Venn-Diagram depicting the protein-overlap between identified PPIs and RDIs with the full ANRIL interactome (E) or the C7orf50-binding ANRIL fragments Ex6u7 and Ex16u17, including C7orf50, with (F) showing the shared overlap between the PPIs and (G) the RDIs.

Results

Despite having distinct interactors, fragments Ex6u7 and Ex16u17 share over 50% of their protein binders, suggesting the presence of potential functional domains within ANRIL. To further investigate whether similar patterns of shared protein interactions exist across all tested ANRIL fragments, a pairwise correlation analysis based on the individual protein enrichment profiles of the fragments was performed.

Functional Domains of ANRIL

As expected, the correlation analysis confirmed the previously observed overlap of shared interactors between Ex6u7 and Ex16u17 (PCC = 0.52, Figure 23A). The strongest correlation was detected between the fragments Ex21part1 and Ex21part2 (PCC = 0.84, Figure 23B). In addition, they show a high correlation with Ex18u19 which is also located in the 3' region of ANRIL (average PCC = 0.71, Figure 23D). Beyond this, fragments composed of exons from the 5' region of ANRIL (Ex1, Ex2, Ex4u5 and Ex8part1) also exhibited similar interaction patterns (average PCC = 0.64), suggesting additional functional domains (Figure 23D).

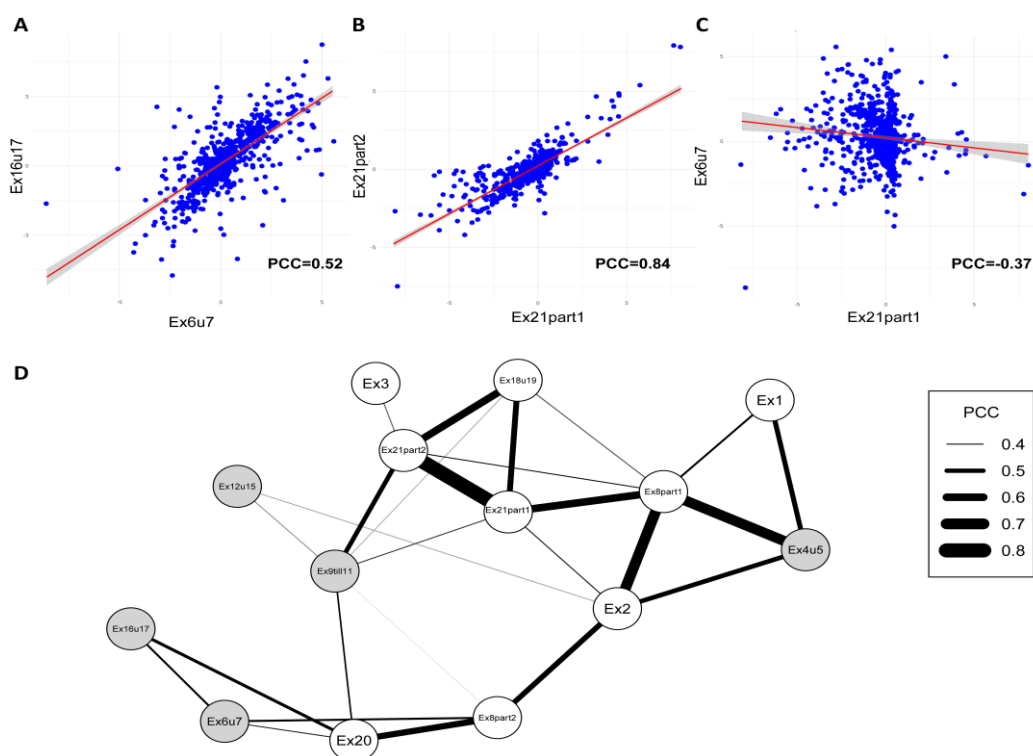


Figure 23 Functional domains of ANRIL based on correlation network analysis

(A-C) Correlation plots illustrating the relationship of selected fragments for ANRIL-interacting proteins. The x- and y-axis represent the individual protein enrichment per fragment compared to the control. The blue dots represent the detected proteins, while the red line indicates the regression trend. The grey line indicates the confidence interval around the fitted regression line. (D) Correlation network diagram showing the similarity of the interacting proteins among the different ANRIL RNA fragments. Nodes represent individual ANRIL fragments, and the thickness of the edges represents the pairwise Pearson correlation coefficient (PCC) between the binding capacities of the fragments to the individual proteins. Nodes are colored in gray if the fragment includes an exon that occurs in a circular isoform. PCCs less than 0.4 are not shown.

Results

ANRIL interacts with proteins that are involved in viral processes

To identify general biological processes (BP) that are potentially mediated through the identified ANRIL-protein interactions, GO enrichment analysis of the 310 ANRIL-associated proteins was performed (Figure 24, Supplementary Table 8). Several interactors are associated with pathways involved in chromatin remodeling, DNA damage, and ribosome biogenesis, which aligns with the previously reported functions of ANRIL (53,54,154,155). In addition, we observed enrichment of interactors associated with RNA-splicing, supporting recent findings that link ANRIL to the regulation of alternative splicing events (57). Interestingly, the analysis also revealed enrichment in RBPs that have not yet been linked directly to ANRIL, including “response to viruses” and “positive regulation of type I interferon production”, suggesting previously unrecognized functions.

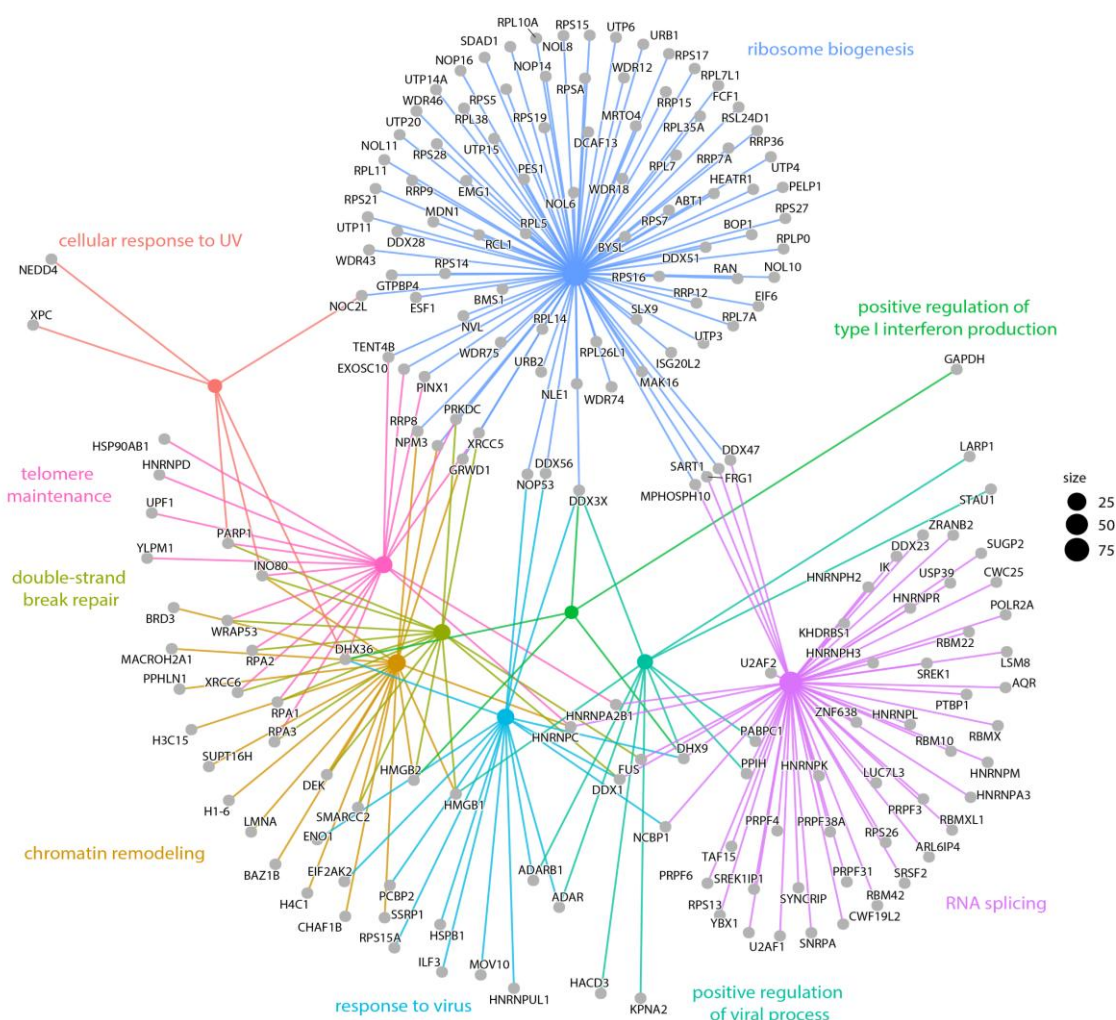


Figure 24 Biological processes of the ANRIL RBP interactome

Cnet plot illustrating selected overrepresented Gene Ontology biological process (GOBP) terms among the 310 proteins that bind to ANRIL. The colored nodes represent GOBP terms, whereas the gray dots indicate associated proteins, with colored edges connecting them to their respective GOBP terms. The size of each GOBP node reflects the number of associated proteins. A list of all the overrepresented terms can be found in Supplementary Table 8.

Results

To better understand the potential functional domains of ANRIL, it was examined whether proteins associated with specific biological functions bind to distinct ANRIL fragments. By applying unsupervised clustering based on the relative enrichment of each protein across the different ANRIL fragments, the interactors were grouped into 7 main clusters (Figure 25A), some of which had distinct cellular functions (Figure 25B). For example, Cluster 1 and Cluster 2 were enriched with proteins involved in metabolic processes, gene expression, and ribosome biogenesis (Figure 25B). While Cluster 1 consists of proteins that are predominantly involved in early rRNA processing, Cluster 2 is enriched with proteins involved in late-stage ribosome assembly, particularly during large subunit maturation (156). Within Cluster 2, several known ANRIL-binding proteins that are associated with rRNA processing were identified, including the key members of the PeBoW complex: PES1, WDR12 and BOP (72). This result aligns with a previous report suggesting that a circular ANRIL isoform comprising exons 5-7 modulates ribosomal RNA maturation by binding to PES1 (70). The PeBoW complex, including the nucleolar protein NOP14, bound to the fragment consisting of the exons 6 and 7 (Figure 25D). These findings underscore the ability of the screen to recover known ANRIL interactors. Intriguingly, Cluster 5 was enriched for processes related to immune signaling and viral regulation, with overrepresented GO terms such as “regulation of viral processes” and “defense response to symbionts” (Figure 25B, E). This result is in line with previous studies reporting that ANRIL expression is upregulated in response to inflammatory stimuli and contributes to immune gene regulation (69,157-159). Moreover, ANRIL has been shown to be differentially expressed in response to viral infections, particularly in the context of oncogenic viruses (74,75). However, these studies focused primarily on the involvement of ANRIL during oncogenesis rather than its role in viral infection or replication itself. Furthermore, DHX9 and ILF3 were found as ANRIL-interacting proteins (Figure 24, Figure 25E, F), both of which have recently been implicated in the regulation of viral processes through interactions with the virus-induced lncRNA BTX (81), underscoring the capability of lncRNAs to directly modulate viral processes.

Thus, on the basis of the overrepresentation of GO terms related to viral regulation (Figure 24, Figure 25B, Supplementary Table 8), transcriptome analysis were performed to determine whether modulation of ANRIL influences pathways involved in viral processes or immune response.

Results

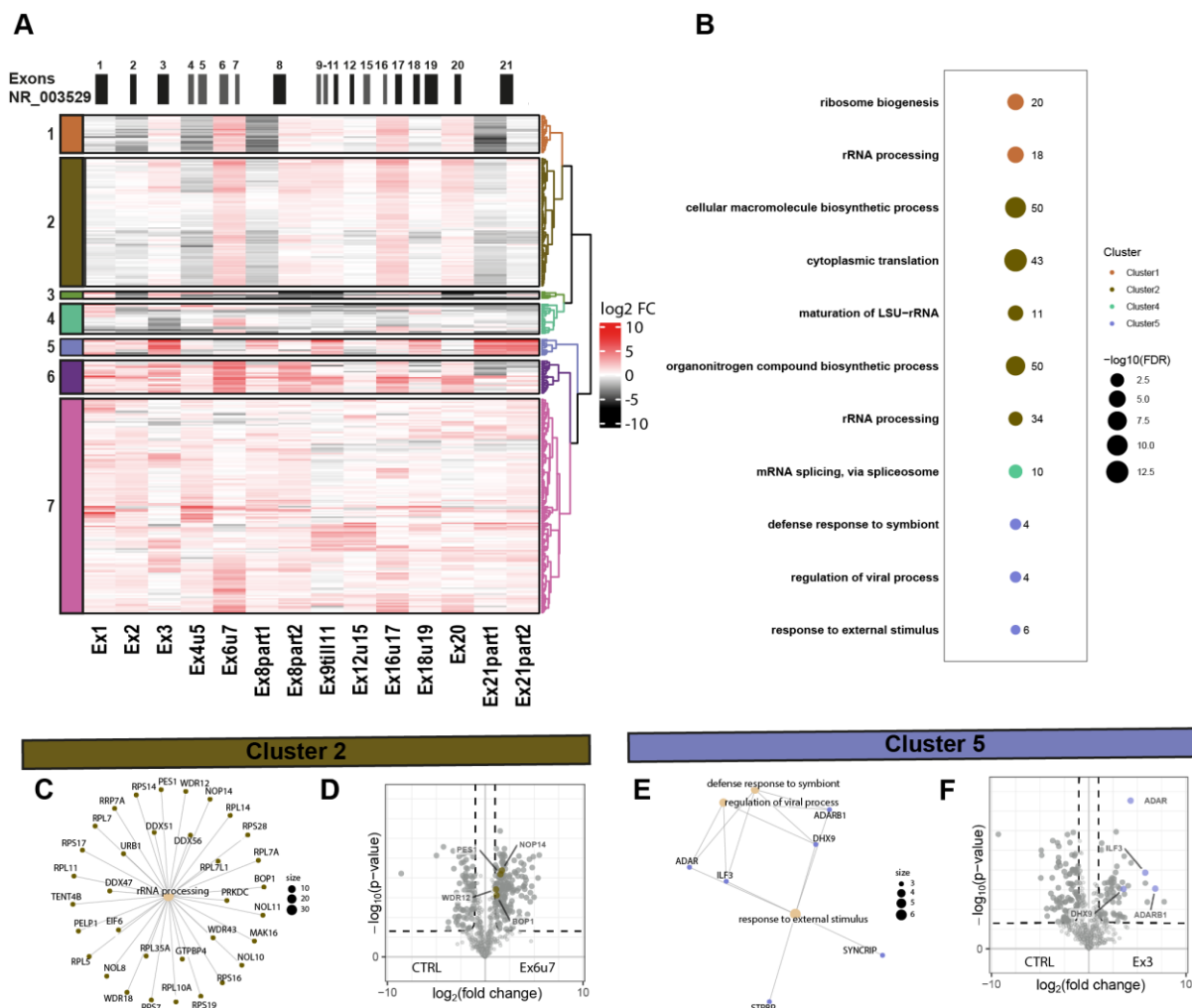


Figure 25 Functional analysis based on unsupervised clustering of ANRIL binding proteins

(A) Unsupervised clustering of the binding profiles of the enriched proteins (fold change (FC) > 2, p-value < 0.05 (Welch's t test), n = 4) revealed 7 clusters. (B) Result of GO enrichment analysis with GOBP terms. The color of the dot indicates the respective cluster, and the size corresponds to the significance (-log₁₀ FDR). The number of proteins associated with each GOBP term is stated. Clusters 6 and 7 had no overrepresentations. A list of all the overrepresented GOBP terms can be found in Supplementary Table 10 (C) Cnet plot showing proteins of Cluster 2 associated with the GOBP term "rRNA processing". (D) Volcano plot showing the results of the RNA pulldown with the Ex6u7 fragment. Subunits of the PeBoW complex are annotated. (E) Cnet plot showing proteins associated with GOBP terms related to the response to external stimuli. (F) Volcano plot depicting the results of the RNA pulldown experiment with fragment Ex3. The dashed lines represent the enrichment threshold (FC > 2, p-value < 0.05 (Welch's t test), n = 4).

ANRIL knockdown deregulates immune related pathways involved in interferon signaling and viral entry

To investigate if ANRIL regulates pathways involved in viral processes, an esiRNA-mediated knockdown against exons 4-6 targeting all known ANRIL isoforms (Figure 8B), followed by RNA-Sequencing was performed.

Despite low knockdown efficiency, esiRNA treatment led to a statistically significant downregulation of ANRIL expression ($p = 0.04$) at 24 h, whereas no significant change could be observed at 48 h ($p = 0.66$) (Figure 26A). Nevertheless, confocal microscopy confirmed a visible depletion of ANRIL signal at 48 h compared to esiRNA mock-transfected control cells (Figure 26B). To include subtle but potentially relevant transcriptional changes, RNA sequencing was performed without applying a foldchange (FC) cutoff, using instead a stringent false discovery rate (FDR) threshold of 0.01.

At 24 h, 620 genes were differently expressed ($FDR < 0.01$) upon ANRIL knockdown (Figure 26C). Reactome-analysis of the 293 downregulated genes, revealed an enrichment for immune related antiviral pathways, such as 'Interleukin-12 signaling', 'ISG15 antiviral mechanism', and 'Antiviral mechanism by IFN-stimulated genes'(Figure 26F, Supplementary Table 11). For example, Mitogen-Activated Protein Kinase 6 (MAP2K6), a key component of the p38 MAP signaling pathway that mediates cellular response to stress and inflammation, including the activation of antiviral gene expression (160,161), was significantly downregulated ($p < 0.0001$) (Figure 26F). TRIM25 an ISG15 E3 ubiquitin ligase (Figure 26F) that activates the viral RNA sensor RIG-I (89), initiating the production of type-I IFNs in response to viral infections (162,163), was also downregulated upon ANRIL knockdown ($p = 0.01$). Additionally, IFNAR1, a subunit of the type-I IFN receptor that mediates the activation of the JAK-STAT signaling pathway, leading to the expression of ISGs that inhibit viral replication (90,164) showed reduced expression ($p = 0.01$). These observations hint towards a potential role of ANRIL in antiviral immune signaling pathways.

At 48 h (Figure 26D), GOBP enrichment analysis of the 431 downregulated genes ($FDR < 0.01$), detected a downregulation of genes involved in 'viral processes' and 'regulation of viral entry into host' (Figure 26G, Supplementary Table 12). For instance, Galectin-1 (LGALS1) ($p = 0.01$), a glycan-binding protein that plays a role in the host defense against infections. LGALS1, can directly interact with pathogens or their glycans, modulating viral entry (165,166). NECTIN2, a cell adhesion molecule that can also mediate viral entry, especially for several herpesviruses such as herpes simplex virus (HSV) or pseudorabies virus (PrV) (167), was significantly downregulated in comparison to mock transfected cells ($p = 0.002$). Lastly, knockdown of ANRIL induced the downregulation of the Ephrin Type-A Receptor

Results

2 (EPHA2) ($p = 0.01$). EPHA2, acts as an entry receptor used by multiple viruses, especially herpesviruses such as Epstein-Barr Virus (EBV) and KSHV (168).

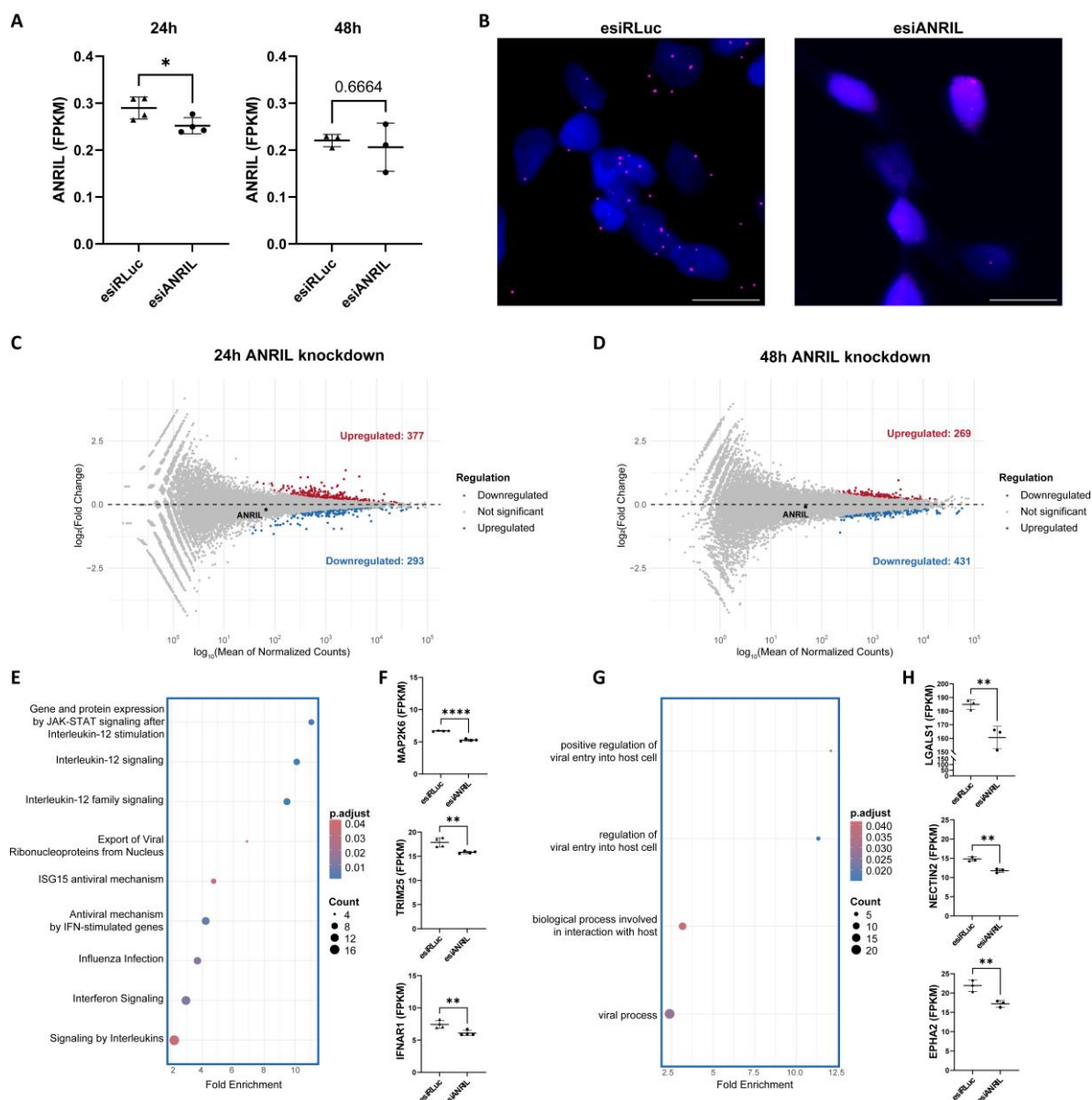


Figure 26 ANRIL knockdown leads to the downregulation of antiviral and immune pathways

(A) Expression level of ANRIL (CDKN2B-AS1) in HeLa Kyoto cells, treated with esiRNAs against RLuc (esiRLuc) and ANRIL (esiANRIL) at 24 h (left) and 48 h (right) post-transfection. Values represent calculated FPKM values ($n=3-4$). Statistical significance was determined via a two-tailed unpaired t test comparing ANRIL esiRLuc FPKM values to esiANRIL FPKM values ($n = 3$ or 4). The error bars indicate the standard deviation (SD) from the mean. (B) Confocal microscopy images of ANRIL expression in esiRLuc (left) and esiANRIL (right) treated HeLa Kyoto cells at 48h (scale bar 15 μ m). (C, D) MA plot visualizing expression fold change on log2 scale vs. log10 mean expression level of all annotated genes. Highlighted are all genes with Benjamini and Hochberg (FDR) corrected p -values < 0.01 . The upregulated genes are highlighted in red and the downregulated in blue. ANRIL (CDKN2B-AS1) is annotated in black. (E) Selected downregulated Reactome terms at 24 h post-transfection. (F, H) Selected downregulated genes at 24 h (F) and 48 h (H) post-transfection. Values represent calculated FPKM values. Statistical significance was determined via a two-tailed unpaired t test comparing ANRIL esiRLuc FPKM values to esiANRIL FPKM values ($n = 3$ or 4) (G) Selected downregulated GOBP terms at 48h post-transfection. A list of all regulated terms can be found in the Supplementary Table 11 and 10. Asterisks indicate the level of significance (p -values: * < 0.05 , ** < 0.01 , *** < 0.001 and **** < 0.0001).

Results

Given the overrepresentation of proteins involved in viral regulation interacting with ANRIL (Figure 24, Figure 25, Supplementary Table 8), and the observed downregulation of antiviral pathways upon ANRIL knockdown (Figure 26, Supplementary Table 11, Supplementary Table 12), the next step was to assess whether ANRIL itself is differentially expressed upon different viral infections.

ANRIL is differentially regulated in response to viral infection

To further investigate the potential role of ANRIL during viral infection, HeLa Kyoto cells were infected with four different non-oncogenic viruses, which represent two different genome types and thus distinct viral mechanisms: double-stranded (ds) DNA viruses (herpes simplex 1 (HSV) and pseudorabies virus (PrV)) and negative-sense single-strand (ss) RNA viruses (influenza A virus (H3N2) and cedar virus (CedV)). Since the screen was performed in HeLa cells, and the downstream analysis should also be performed in the same cell type, it was essential to initially verify whether these viruses could infect HeLa cells. Therefore, viral protein levels were assessed at 24 hours post-infection (hpi) by extracting proteins from infected and uninfected control cells (CTRL), followed by proteomic analysis. In all viral infections, an enrichment of viral proteins could be observed (Figure 27), suggesting that all viruses are in general able to infect HeLa cells.

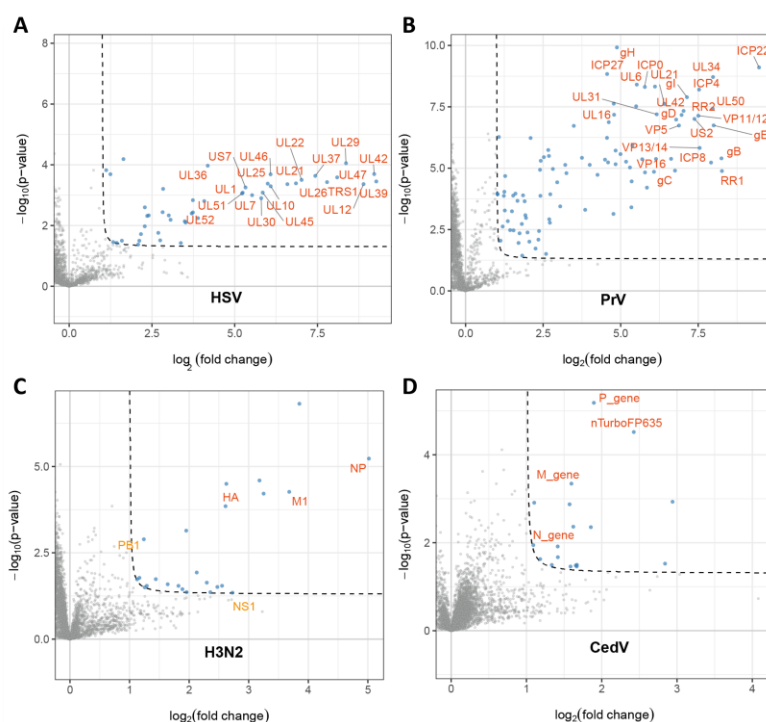


Figure 27 Proteome analysis of HeLa cells infected with four different viruses at 24 hpi

Volcano plots depicting the proteome analysis of herpes simplex virus 1 (HSV1-KOS (HSV)), recombinant pseudorabies virus PrV-Kaplan- Δ gGfp (PrV), influenza A virus (A/Victoria/3/1975(H3N2)) and recombinant cedar virus (rCedV_nTurbo-FP635 (CedV)) infected HeLa cells at 24 hpi. The dashed lines represent the enrichment threshold (FC > 2, p-value < 0.05 (Welch's t test), n = 4). Enriched viral proteins are highlighted in orange.

Results

To further assess whether ANRIL expression is regulated upon viral infection, its expression changes at 24 and 48 hpi was examined via RT-qPCR with primers targeting exons 5-6, which are present in all isoforms (Figure 8A). The expression levels were compared to those in uninfected cells (CTRL) and normalized to 18S rRNA (169,170). In line with the suppression of ANRIL expression in gammaherpesvirus KSHV-infected cells (15), we detected a statistically significant decrease in ANRIL expression in response to the dsDNA alphaherpesviruses HSV and PrV at 24 hpi (Figure 28A). This effect was even more pronounced at 48 hpi, with HSV causing marked inhibition of ANRIL expression (FC = 0.09) (Figure 28B). In contrast, infection with the ssRNA viruses H3N2 and CedV resulted in a significant upregulation of ANRIL, with CedV inducing a 1.9-fold and H3N2 a 4-fold upregulation at 48 hpi (Figure 28A, B).]

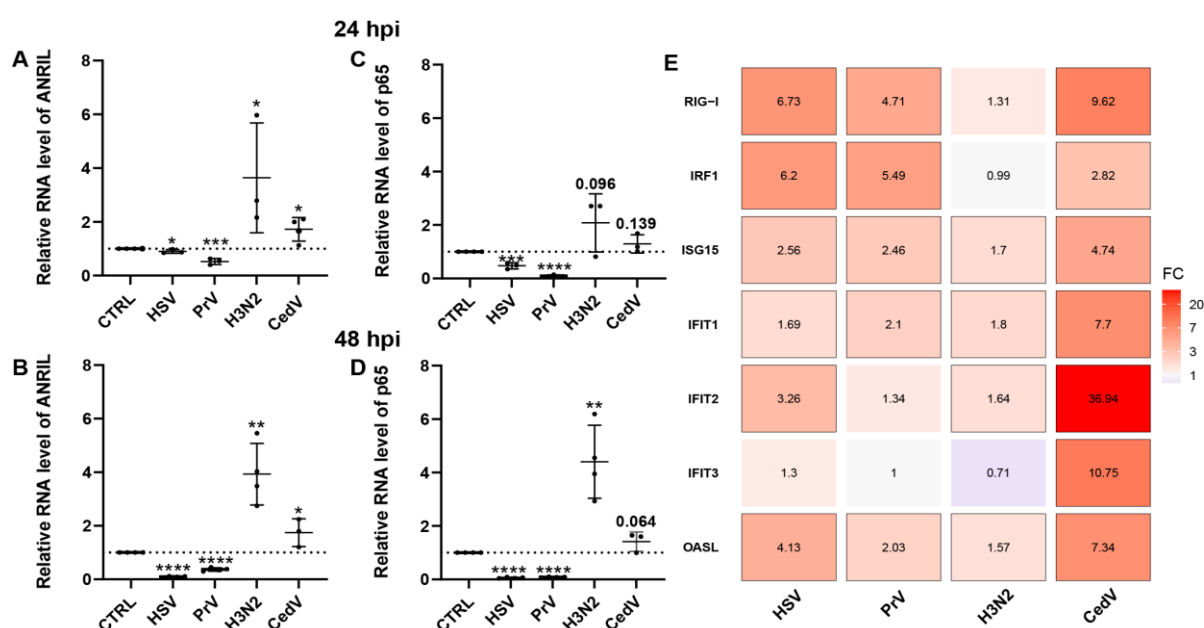


Figure 28 ANRIL is differentially expressed upon viral infection

Different viruses were used to evaluate changes in ANRIL expression upon infection. Herpes simplex virus 1 (HSV1-KOS (HSV)) and recombinant pseudorabies virus PrV-Kaplan- Δ gGfp (PrV) were used as representative dsDNA viruses, and influenza A virus (A/Victoria/3/1975(H3N2)) and recombinant cedar virus (rCedV_nTurbo-FP635 (CedV)) represented negative ssRNA viruses. RT-qPCR results of ANRIL (A, B) and p65 (C, D) in HeLa Kyoto cells infected with an MOI of 1 at 24 hpi and 48 hpi, respectively. Individual expression values were normalized to those of 18S rRNA. Statistical significance was determined via a two-tailed unpaired *t* test comparing noninfected controls (CTRL) to individual infections (*n* = 3 or 4). The error bars indicate the standard deviation (SD) from the mean. Asterisks indicate the level of significance (*p*-values: * < 0.05, ** < 0.01, *** < 0.001 and **** < 0.0001). (E) Heatmap visualizing the changes in the expression of selected innate immune response genes at 24 hpi (MOI=1). The color scale represents the fold change (FC) between the noninfected control and infected samples based on mean CPM values. Framed boxes indicate an FC > 1.5.

Viruses are known to modulate the NF- κ B signaling pathway (171), and previous studies have shown that ANRIL expression is induced through the binding of p65 in response to inflammatory stimuli (69,74,172). Therefore, p65 mRNA expression after viral infection was examined to investigate its potential role in driving the observed differential expression of ANRIL. A strong reduction in p65

Results

transcripts in response to dsDNA virus infection was detected, whereas ssRNA virus infection increased p65 mRNA expression. At 48 hpi, p65 transcripts were nearly undetectable in HSV- and PrV-infected cells. In contrast, ssRNA viruses caused upregulation, ranging from 1.4-fold (CedV) to 4-fold (H3N2) (Figure 28D). To obtain a broader view of immune regulation upon virus infection, RNA-Sequencing at 24 hpi was performed and selected immune response genes examined (Figure 28E). The strongest immune response was observed in CedV-infected cells, with a marked upregulation of RIG-I (FC = 9.6) and its downstream type-I IFN-induced proteins with tetratricopeptide repeats (IFITs) especially of IFIT2, with a 36.9-fold increase. Whereas H3N2 infection upregulated ANRIL and p65, it only slightly upregulated the investigated immune response transcripts at 24 hpi. Infection with PrV and HSV generally induced the upregulation of immune response genes at 24 hpi. However, IFIT3 was not upregulated in any of the dsDNA viruses.

Given the significant changes in ANRIL expression observed in CedV-infected cells, the identification of ANRIL binders involved in type-I IFN production, such as the DExD/H-box RNA helicases DHX36, DHX9, and DDX3X, in the initial screen (Figure 24) and the detected involvement of ANRIL in interferon pathways, it was further investigated whether ANRIL could have an antiviral role during CedV infection.

ANRIL is expressed in a time- and dose-dependent manner and associates with immune activation during CedV infection

To support the hypothesis that ANRIL is expressed in response to CedV infection, the changes in expression at different timepoints and with varying infection doses were measured (Figure 29). In line with the previous data, ANRIL was upregulated following CedV infection. At an MOI of 1, ANRIL expression increased 1.9-fold at 24 hpi and peaked at 72 hpi (2.6-fold) compared to the uninfected control, which aligns with increased CedV RNA levels (Figure 29A).

Interestingly, this pattern was mirrored by several immune response genes, which also began to increase at 24 hpi (Figure 29B). This observation is consistent with previously published transcriptomic data from CedV-infected HeLa cells (173). Interestingly, TRIM25 which was downregulated upon ANRIL knockdown and is responsible for RIG-I activation (89), shows a significant upregulation coinciding with increased ANRIL levels and strong RIG-I induction at 48 hpi (Figure 29B). Possibly hinting towards a role of ANRIL in RIG-I pathway induction. Notably, ANRIL has previously been shown to promote the expression of cytokines in response to inflammatory stimuli in CAD (89). Consistently, IL-6 expression rose from 1.5-fold at 6 hpi to 23-fold at 24 hpi, which coincided with the increase in ANRIL levels and further supported a possible connection between ANRIL induction through CedV infection and the downstream activation of immune-related genes.

Additionally, a dose-dependent increase in ANRIL expression at 48 hpi was detected, which also fitted with increased levels of CedV RNA. While infection at an MOI of 0.1 resulted in a 1.4-fold increase, infection at an MOI of 3 led to a 4.2-fold upregulation of ANRIL compared with the uninfected control (Figure 29C). These results were further confirmed via fluorescence in situ hybridization (FISH) with ANRIL-specific probes, revealing an increase in ANRIL expression at 48 hpi compared to the uninfected control (Figure 29D).

Results

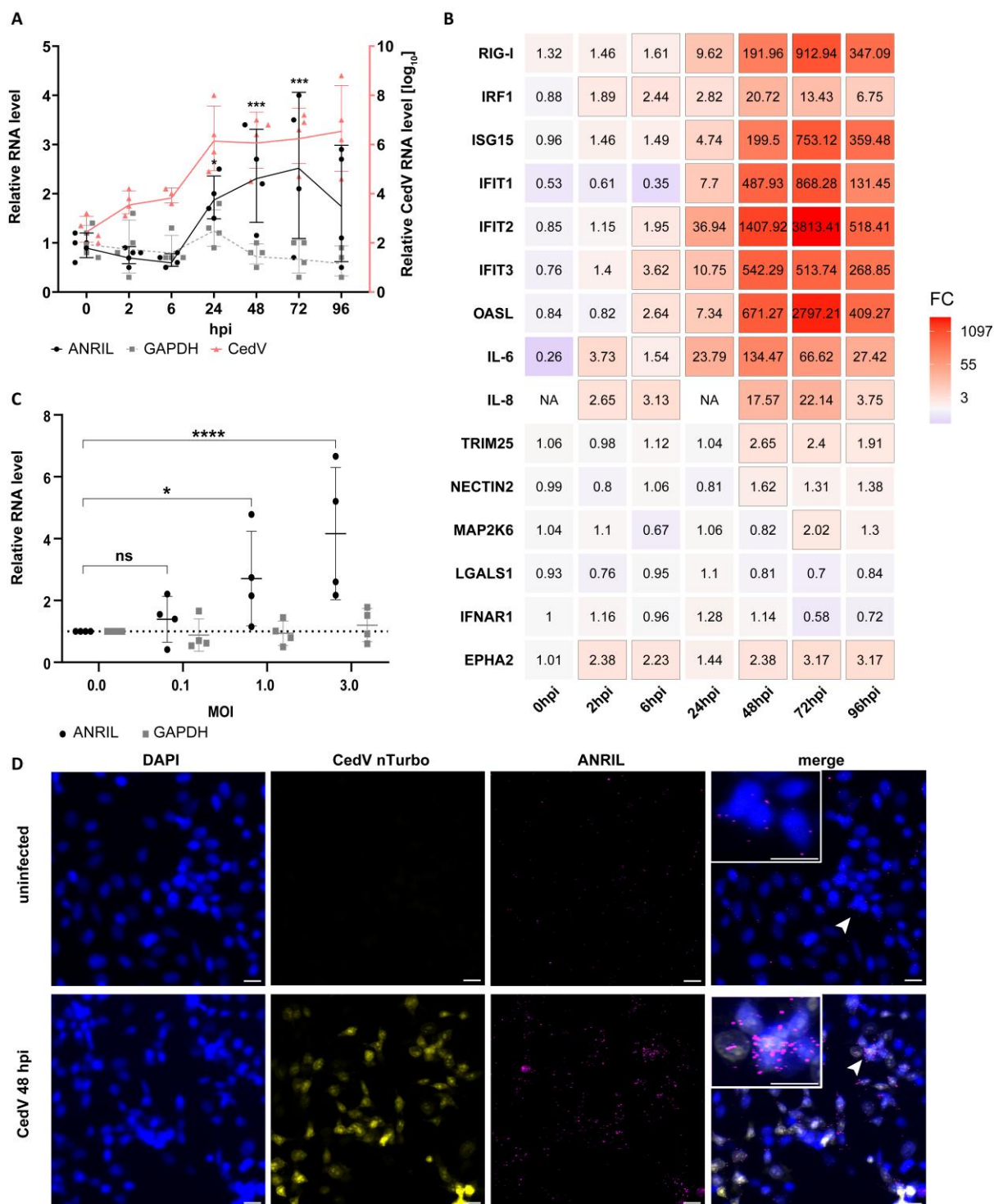


Figure 29 ANRIL is expressed dose- and time-dependent upon CedV infection and associates with immune activation

(A) RT-qPCR analysis of ANRIL expression during infection. For time-dependent expression, HeLa Kyoto cells were infected with recombinant cedar virus (rCedV_nTurbo-FP635 (CedV)) at an MOI of 1. (B) Heatmap visualizing expression changes of selected genes at different time points (MOI=1). The color scale represents the fold change (FC) between the noninfected control and infected samples based on mean CPM values ($n=4$). Framed boxes indicate an FC > 1.5. (ND = not detected) (C) For the dose response experiments, the stated MOIs were used, and RNA was extracted at 48 hpi. β -actin mRNA expression was determined for normalization. Statistical significance was calculated via 2-way ANOVA ($\alpha=0.05$, Dunnett correction, $n=4$). The error bars indicate the standard deviation (SD) from the mean. Asterisks indicate the level of significance (p -values: ns > 0.05, * < 0.05, ** < 0.01, *** < 0.001 and **** < 0.0001). (D) Confocal microscopy images of ANRIL expression in uninfected and CedV-infected (MOI=1) HeLa Kyoto cells at 48 hpi (scale bar 15 μ m).

Results

ANRIL knockdown increases CedV replication

As CedV infection increased ANRIL levels, it was determined whether changes in ANRIL expression itself affect CedV infection. To test this hypothesis, an esiRNA-mediated knockdown of ANRIL 24 hours before CedV infection at an MOI of 1 was performed, followed by RNA isolation at 24 and 48 hpi.

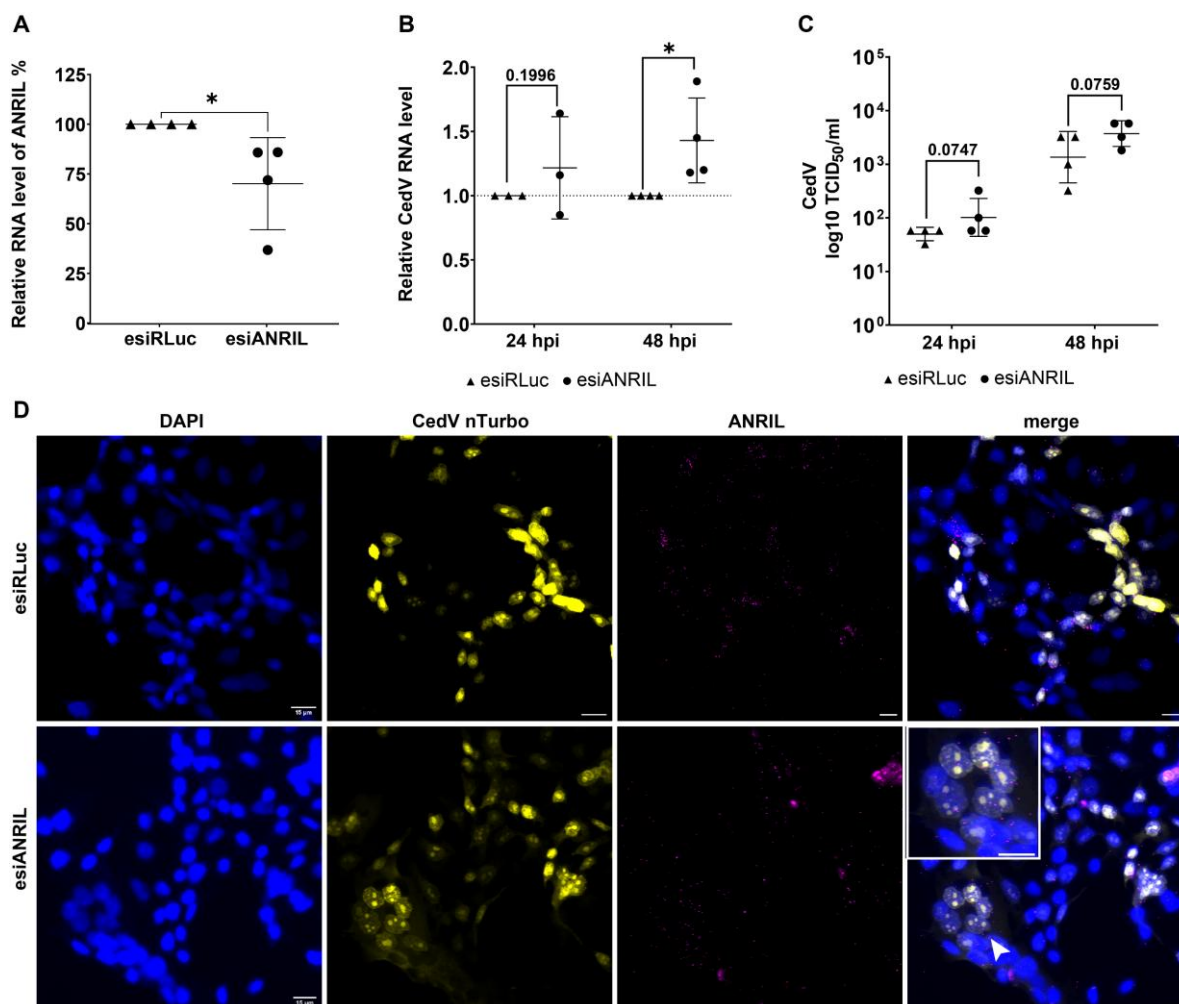


Figure 30 ANRIL knockdown increases the CedV viral RNA level and titer at 48 hpi

(A) Bar chart showing the RT-qPCR results of ANRIL knockdown via esiRNAs in HeLa Kyoto cells. ANRIL expression was normalized to that of β -actin mRNA. Statistical significance was calculated via unpaired two-tailed t test ($n=4$) (B) RT-qPCR results comparing the expression of CedV RNA after ANRIL knockdown (esiANRIL) to that of the mock-transfected control (esiRLuc) in CedV-infected HeLa Kyoto cells (MOI=1). Statistical significance was calculated via unpaired one-tailed t test ($n=3$ or 4) (C) Results of the TCID₅₀ endpoint dilution assay at 24 and 48 hpi comparing mock-transfected control (esiRLuc) and ANRIL-knockdown (esiANRIL) cells after CedV (MOI=1) infection. Statistical significance was calculated via unpaired one-tailed t test ($n=4$). The error bars indicate the standard deviation (SD) from the mean. Asterisks indicate the level of significance (p -values: ns > 0.05, * \leq 0.05). (D) Confocal microscopy images of ANRIL expression in esiRLuc and esiANRIL transfected and CedV-infected (MOI=1) HeLa Kyoto cells at 48 hpi (scale bar 15 μ m).

Results

Even though the knockdown decreased the ANRIL level to only 70.1% (Figure 30A), RT-qPCR analysis revealed that the expression of CedV RNA was significantly upregulated compared with that in mock-transfected cells (RLuc) at 48 hpi ($p = 0.04$) (Figure 30B). This was further evidenced by increased viral titers upon ANRIL knockdown (Figure 30C). Interestingly, confocal microscopy of mock-transfected (esiRLuc) and ANRIL knockdown (esiANRIL) HeLa cells infected with CedV (MOI=1) at 48 hpi showed increased occurrence of syncytia formation in the esiANRIL samples (Figure 30D). This phenotype could be attributed to the observed downregulation of LGALS1 at 48h (Figure 26H), a gene previously reported to block syncytia formation in NiV infected endothelial cells, another Henipavirus closely related to CedV (118,174). The time-course, however, didn't show a significant upregulation of LGALS1 (Figure 29B).

INO80 knockdown shows mild effect on CedV infection

The initial interactomics screen identified several proteins that could mediate the observed antiviral function of ANRIL. As described earlier, ANRIL has been shown to induce cytokine expression in response to an inflammatory stimulus. Briefly, ANRIL guides the transcription factor YY1 to the promoter of IL-6 and IL-8 (69). In contrast to previous studies (60,69,175), YY1 was not identified as a direct binder of ANRIL. However, its coactivator INO80 was found binding to Ex16u17 (Figure 31A). The INO80 Complex ATPase subunit (Q9ULG1) is a core member of the INO80 chromatin remodeling complex (176) (Figure 31E) and has been shown to associate tightly with YY1 to facilitate access to its target promoter binding sites (177,178). Indeed, treatment INO80-IPs detected the full INO80-complex, including YY1, as direct protein-protein interactors of INO80 (Figure 31B). Notably, YY1 was not identified as an RNA-dependent interactor of INO80 (Figure 31C), suggesting that ANRIL could facilitate the recruitment of INO80 to YY1, rather than serving as a direct scaffold between them. This interaction may, in turn, enable the binding of YY1 to the promoters of IL-6 and IL-8 (Figure 31F). The absence of ANRIL may reduce the interaction between INO80 and YY1, potentially impairing the activation of the immune response genes resulting in the observed increased viral replication.

Results

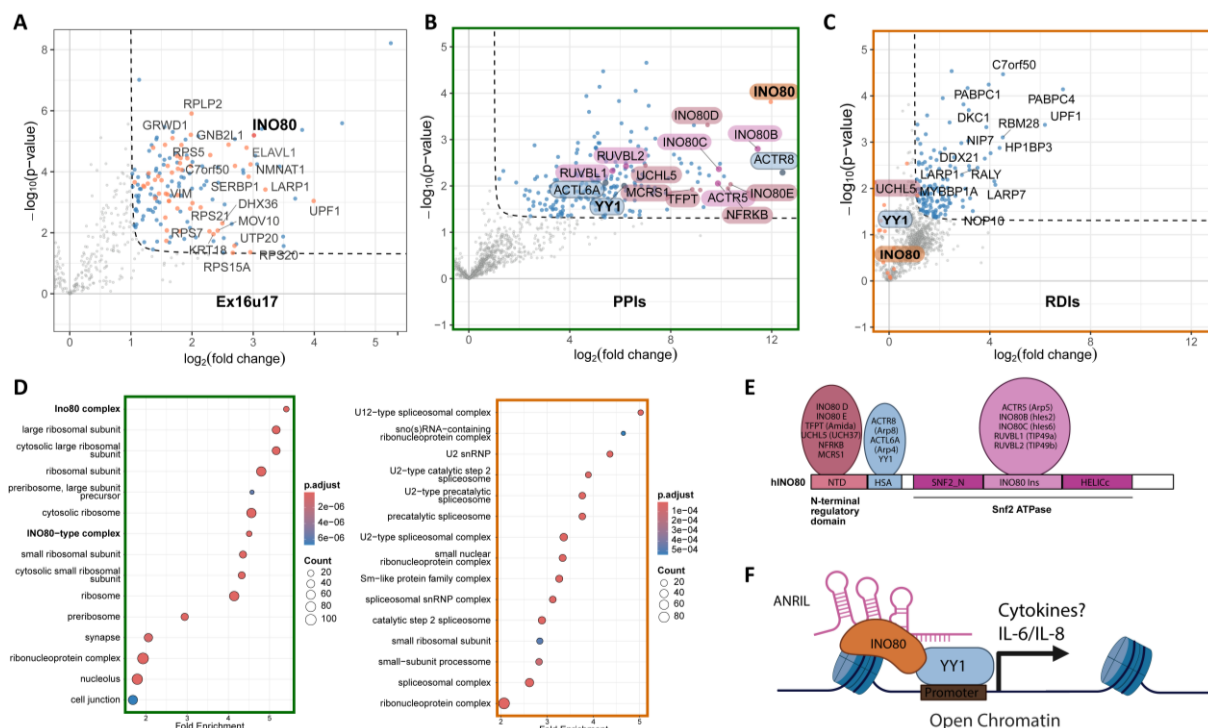


Figure 31 *INO80* interacts with *YY1*

(A) One-sided volcano plot depicting the results of the RNA pulldown experiment with ANRIL fragment Ex16u17. The dashed lines represent the enrichment threshold (FC > 2, p-value < 0.05 (Welch's t test), n = 3). Proteins found interacting with INO80 are highlighted. (B, C) Treatment IP using INO80 specific antibody. Volcano plot depicting the protein-protein interactions (PPIs) of INO80 (B) and RNA-dependent interactions (RDIs) (C) (FC > 1.5, p-value < 0.05 (Welch's t test), n = 3). (D) GO cellular compartment enrichment analysis of PPIs (left) and RDIs (right) of INO80. (E) Human INO80 complex. NTD, N-terminal domain; HSA, helicase-SANT-associated domain; SNF2_N; SNF2 family N-terminal domain; Ins, insertion domain; HELICc, Helicase C-terminal domain (adapted from Su et al. 2016) (F) Model for the interaction of ANRIL with INO80. ANRIL recruits INO80 to YY1. YY1 binds to the promoter of cytokines (IL-6, IL-8) inducing their expression.

To investigate the role of INO80 during CedV infection an esiRNA -mediated knockdown was performed. The knockdown successfully induced a statistically significant reduction of INO80 to around 30% (p = 0.0001) (Figure 32A). While proteome analysis didn't show a downregulation of immune response proteins related to IL-6 or IL-8 at 24 h, GOBP-enrichment analysis detected the downregulation of proteins involved in 'response to interleukin-7' and 'viral life cycle' (Figure 32C). Interestingly, Reactome-enrichment analysis of the upregulated proteins detected an increase in proteins involved in 'viral mRNA translation' (Figure 32C). In line with this, qPCR analysis revealed an increase in CedV RNA at 48 hpi (p = 0.07) (Figure 32D). Similarly, a slight increase in viral proteins could be detected at 48 hpi (Figure 32E). Especially the viral nucleoprotein (N_CDS) and phosphoprotein (P_CDS) showed increased expression (Figure 32E). Fluorescence microscopy at 48 hpi also visually indicates an increase in CedV replication. However, the INO80 knockdown alone was not able to induce a statistically significant increase in viral RNA or proteins or give an indication of its role during immune response induction at this point.

Results

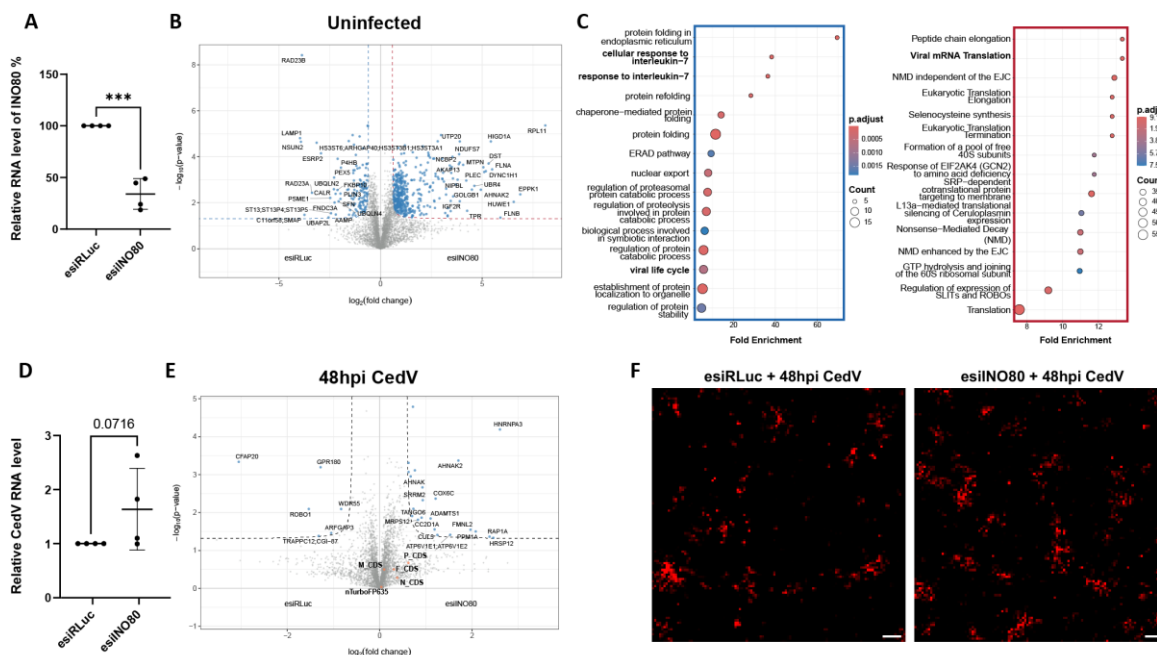


Figure 32 INO80 knockdown leads to increased CedV RNA and proteins

(A) Bar chart showing the RT-qPCR results of INO80 knockdown via esiRNAs in HeLa Kyoto cells at 48h post-transfection. INO80 expression was normalized to that of β -actin mRNA. Statistical significance was calculated via unpaired two-tailed *t* test ($n=4$). (B) Volcano plot depicting the results of the proteome-wide changes after INO80 knockdown (esiINO80) compared to mock-transfected control cells (RLuc) at 24h post-transfection. The dashed lines represent the enrichment threshold ($FC > 1.5$, p -value < 0.05 (Welch's *t* test), $n = 3$). The colors highlight the down (blue) and upregulated (red) site (C) Top15 GOBP-enrichment analysis of down (blue) and Reactome-enrichment of up (red) regulated proteins after INO80 knockdown (24h) (D) RT-qPCR results comparing the expression of CedV RNA after INO80 knockdown (esiINO80) to that of the mock-transfected control. (esiRLuc) in CedV-infected HeLa Kyoto cells (MOI=1) 48hpi. Statistical significance was calculated via unpaired one-tailed *t* test. (E) Volcano plot depicting the results of the proteome-wide changes after INO80 knockdown (esiINO80) compared to mock-transfected control cells (RLuc) at 48 hpi with CedV (MOI=1). The dashed lines represent the enrichment threshold ($FC > 1.5$, p -value < 0.05 (Welch's *t* test), $n = 3$). (F) Fluorescence microscopy of esiRLuc (left) and esiINO80 (right) treated CedV-infected (MOI=1) HeLa Kyoto cells at 48 hpi (scale bar 15 μ m).

In summary, systematic mapping of the ANRIL interactome identified a previously unrecognized role of ANRIL in interacting with proteins involved in diverse viral processes. The knockdown analysis of ANRIL further supported this, by providing evidence that ANRIL depletion leads to the downregulation of genes involved in interferon-mediated antiviral defense. Additionally, viral infection studies revealed that ANRIL expression is modulated depending on the ability of the HeLa cells to activate the NF- κ B and IFN signaling pathways. Notably, the knockdown of ANRIL resulted in increased CedV load, suggesting a possible protective role of ANRIL in antiviral immunity. Finally, the newly identified ANRIL-interacting protein INO80 was found to influence viral load, offering a first mechanistic insight into how ANRIL may regulate antiviral responses. However, further in-depth functional analysis are necessary to understand the underlying regulatory processes.

Discussion

ANRIL as a multifaceted regulator in chromatin and splicing

LncRNAs regulate gene expression through diverse mechanisms, including chromatin remodeling, transcriptional modulation, and post-transcriptional regulation (24,25). Their dysregulation has been implicated as a driving factor or contributing cause in numerous diseases, such as cancer and cardiovascular disorders. As their functions are largely mediated through interactions with proteins (37), multiple studies have sought to systematically characterize the protein interactome of lncRNAs. Recent examples include the analysis of the oncogenic lncRNAs HOTAIR (179) and MALAT1 (180) as well as the mediator of X-chromosome inactivation Xist (179). Due to its localization in a disease-associated hotspot, the lncRNA ANRIL has been studied primarily in the context of cancer and cardiovascular diseases (53,54,155). However, despite progress in understanding the regulatory activities of ANRIL, its full spectrum of protein interactors remains incomplete.

Employing an RNA-centric approach, 310 ANRIL-interacting proteins were identified, substantially expanding the current knowledge of its interactome. This included several well-known RBPs frequently identified in diverse RNA-interaction studies, such as UPF1, ELAVL1 and MOV10 (181,182).

ELAVL1 contains three RNA recognition motifs and interacts with a diverse set of lncRNAs to regulate their stability and function (183). Its third RNA recognition motif specifically binds to AU-rich elements (184). For example, ELAVL1 has been shown to interact with AU-rich elements within the Macrophage-Associated Atherosclerosis lncRNA Sequence MAARS, a regulator of macrophage apoptosis and atherosclerosis progression, by modulating ELAVL1 cytoplasmic shuttling (185). Overexpression of linear ANRIL transcripts have been linked to decreased apoptosis and increased proliferation of macrophages, whereas its predominantly cytoplasmic circular isoforms have been associated with increased apoptosis and reduced proliferation (155). Since ANRIL harbors multiple AU-rich elements and ELAVL1 bound to 11 out of 14 ANRIL fragments, covering exons present in both linear and circular isoforms, it would be of interest to investigate whether ANRIL exerts an isoform-specific regulation of ELAVL1 that contributes to these distinct effects.

The helicase MOV10 enriched at 8 out of the 14 ANRIL fragments, has been shown to interact with multiple lncRNAs, possibly influencing their stability (182,186,187). ANRIL promotes epigenetic silencing of tumor suppressor genes at its own locus through interactions with PRC1 and PRC2 components, such as CBX7, SUZ12 or EZH2 (60). While the previously described subunits of the canonical PRC1 or PRC2 complex were not identified binding to ANRIL in this screen, prior work has

Discussion

suggested that MOV10 may act as an accessory protein facilitating the recruitment of the PRC1 complex to chromatin via interaction with CBX7 (188). It has been hypothesized that MOV10 influences the secondary structure of ANRIL, promoting its ability to interact with PRC1 components (54). This idea is supported by earlier work on the interaction between ANRIL and CBX7. Although they showed a stable interaction by *in vivo* RNA-ChIP analysis their presented K_D -values in the micromolar range suggest a rather weak binding especially in the presence of competitive RNA (59). This points to the possible involvement of a stabilizing binder, such as MOV10.

Furthermore, another PRC-associated protein, WDR5, was identified as a specific interactor of the Ex6u7 fragment. WDR5 associates with multiple chromatin remodelers, including the non-canonical PRC1.6 complex (189). Previous studies have already described that ANRIL interacts with WDR5 causing epigenetic modifications at the NOX1 promoter (68). Notably, the screen revealed additional chromatin remodelers not previously reported as ANRIL interactors. These include members of the FACT complex (SSRP1, SUPT16H), the SWI/SNF component SMARCC2, and the chromatin-remodeling ATPase INO80. Additionally, the bromodomain-containing proteins BRD3 and BAZ1B were found specifically binding to fragments Ex3 and Ex6u7, respectively. Numerous studies have demonstrated that lncRNAs modulate gene expression by interacting with multiple chromatin-modifying complexes, either through directing histone or DNA modifications or by altering nucleosome positioning and composition (190). For instance, the lncRNA HOTAIR represses target gene expression by binding the PRC2 complex at its 5' end and the LSD1 complex at its 3' end (191). Similarly, distinct conserved repeat domains of Xist interact with multiple chromatin modifiers during X-inactivation (192). These findings suggest that ANRIL indeed could be involved in chromatin remodeling also in a PRC-independent manner.

Several splicing factors (SFs) were identified that interact with ANRIL, including the serine/arginine-rich protein SRSF2, and the heterogeneous nuclear ribonucleoproteins (hnRNP) PTBP1 (HNRNP-K) together with multiple other hnRNPs. Consequently, among the biological processes enriched in the dataset, splicing emerged as a particularly prominent category. Several lncRNAs are known to regulate splicing through interactions with SFs (193). For example, MALAT1 recruits SRSF2 to the Protein kinase C δ , promoting alternative splicing causing enhanced survival and proliferation of injured neuronal cells. Notably, one of the Clusters identified in the screen was specifically enriched with proteins associated with the functional annotation term "mRNA splicing, via spliceosome", suggesting that certain fragments of ANRIL may be involved in mediating those splicing processes. This is further supported by a recent study investigating ANRIL's genomic occupancy, which found that 40.3% of ANRIL binding sites are located in intronic regions and that 24% of ANRIL-associated genes are alternatively spliced (57).

Discussion

The screen also recovered several previously reported ANRIL interactors, such as HNRNPD (AUF1) (194,195), IGF2BP3 (196), FUS (197) and members of the PeBoW complex (70), providing confidence that the screen is able to capture known, but also yet uncharacterized interactors.

Numerous proteins involved in 'ribosome biogenesis' and 'rRNA processing' were found binding to ANRIL, suggesting a potential role of ANRIL in these processes. The PeBoW complex, composed of PES1, BOP1 and WDR12, plays an important role in ribosome biogenesis by coordinating several essential steps, including 28S rRNA processing (152) and pre-rRNA transcription (198). By promoting ribosome biogenesis, the complex contributes to the regulation of cell cycle progression and cell proliferation (71). Interestingly, BOP1 is elevated in patients with atherosclerosis (199,200). Previous work by Holdt et al. demonstrated that a circular isoform of ANRIL (circANRIL), consisting of the exons 5 to 7, can bind to PES1, preventing the formation of the PeBoW complex and thereby the exonuclease mediated processing of 47S pre-rRNA to 28S and 5.8S rRNA in the nucleolus. Specifically, they performed a pulldown of stably expressed circANRIL containing a BoxB sequence, enabling the capture of circANRIL-bound proteins from whole-cell lysates via high-affinity purification using λ N-peptide-coupled beads. This approach identified 32 specific circANRIL-interacting proteins, 38% of which were linked to ribosome biogenesis and assembly, including PES1. They further demonstrated that ANRIL binds to the C-terminal domain of PES1 via RNA regions with high pre-rRNA sequence homology, thereby competing with the pre-rRNA-binding site of PES1 and inhibits the formation of the complex. This disruption leads to reduced proliferation and increased apoptosis in vascular smooth muscle cells (VSMC), contributing to an atheroprotective effect (70). Although a different pulldown approach was used in this study, using *in vitro* transcribed linear ANRIL fragments, PES1 in addition to all other members of the PeBoW complex could be identified at the expected fragment Ex6u7. This demonstrates that while *in vivo* methods provide valuable insights into native protein interactions, *in vitro* approaches are still able to identify meaningful interactors.

Increasing evidence supports the role of lncRNAs in regulating ribosome biogenesis, with their dysregulation impacting protein synthesis and disease progression (201,202). The presence of various proteins involved in 'ribosomal biogenesis' emphasizes the need to further investigate the role of ANRIL during this process and its potential impact on disease. A particularly interesting candidate for further investigations is the largely uncharacterized protein C7orf50, which has also been previously associated with ribosome biogenesis.

C7orf50 interaction with ribosomal proteins links ANRIL to 60S maturation

C7orf50 was identified binding to the ANRIL-fragments Ex6u7 and Ex16u17. The specific binding could be validated using GFP tagged C7orf50 for Ex16u17, but not for Ex6u7 (data not shown). *In silico* predictions using AlphaFold3 suggested binding of C7orf50 to both fragments, whereas no interaction was predicted with the pDEST17 control. However, it should be noted that the interface predicted template modelling (ipTM)-scores for all predictions were below 0.6 (147), indicating a high likelihood of inaccuracy. Low ipTM-scores may be caused by large, disordered regions within the protein (203), as well as from the use of RNA target sequences, given that most prediction tools are primarily trained on protein datasets rather than RNA structures (204). To further validate the specific binding of C7orf50 to ANRIL, different fragments of C7orf50 should be amplified to narrow down the binding site. A 2019 study identified a conserved RNA-binding domain called DUF2373 (WKF) at the C-terminus of C7orf50, where mutations in this domain led to decreased RNA-binding ability (148). Consistently, the *in silico* predictions indicate that this domain is largely responsible for the interaction with the ANRIL fragments. It would therefore be interesting to examine whether expressing only this domain is sufficient to bind the fragments. Further, CLIP-qPCR analysis against C7orf50 using different primer pairs along ANRIL would further validate the binding *in vivo* (205,206).

Fluorescence microscopy following GFP-C7orf50 overexpression indicated its localization in large nuclear condensates, possibly nucleoli. This observation is consistent with recent findings showing that the yeast homolog of C7orf50, Rbp95, colocalizes with the nucleolar marker NOP58 (151). As nucleoli are the primary site of ribosome biogenesis (149,150), it was not surprising to see a number of ribosomal proteins interacting with C7orf50. Supporting this, the C7orf50 interactome included several human homologs of proteins previously identified in a TurboID proximity labeling study of the yeast homolog Rbp95. This study showed the physical proximity of Rbp95 to ribosomal assembly factors (AFs) involved in pre-60S maturation (151). Notably, these included Nop7 and Ytm1, which are the yeast homologs of PES1 and WDR12. As Rbp95 participates in 60S subunit maturation through interactions with the Npa1 complex and the ribosomal protein Rpl3 (151), it would be of interest to investigate whether the human homolog C7orf50 fulfills similar functions in human cells. Additionally, it would be interesting to investigate if ANRIL may act as a scaffold for the interaction between C7orf50 and Rpl3, as this protein was identified interacting with both C7orf50 and the C7orf50-binding ANRIL fragments Ex6u7 and Ex16u17. Even though the interaction between C7orf50 and Rpl3 seems to be a direct protein-protein interaction rather than an RNA-dependent interaction based on the IP-MS data.

ANRIL as a protective factor during CedV infection

Viral infections induce widespread remodeling of the host cell transcriptome, including significant changes in lncRNA expression profiles (207). Increasing evidence shows that lncRNAs themselves can influence infection outcomes by modulating antiviral signaling pathways or through direct regulation of viral replication (79). ANRIL, in particular, has been shown to regulate the immune response by modulating inflammatory gene expression and the activation of the NF- κ B signaling pathway (69,172). While differential expression of ANRIL has been reported in various viral infections (74,75,77), no direct functional link between ANRIL expression and viral infection outcomes has been demonstrated. Intriguingly, the presented study revealed recurring enrichment of immune and virus-associated terms, indicating a potential role of ANRIL in host-pathogen interactions. For example, several ANRIL-interacting proteins are annotated with virus-related GO terms such as 'positive regulation of viral process' and 'response to virus' and immune-related pathways including 'response to interleukin-7' and 'positive regulation of type I interferon production'. Additionally, ANRIL knockdown induced the downregulation of multiple genes involved in interferon signaling and viral entry. While the knockdown efficiency of ANRIL using self-prepared esiRNAs was moderate, resulting in only subtle changes in gene expression, no FC cutoff was applied in the bioinformatic analysis. Instead, a stringent FDR threshold of 0.01 was used to capture even minor, but still interesting transcriptional alterations (208). However, these findings should be only considered indicative, and further validations using RT-qPCR or a stronger ANRIL knockdown are required to confirm specific regulatory effects. Thus, the transcriptome analysis serves only as a complementary line of evidence supporting the potential role of ANRIL in immune regulation and antiviral response.

Building on these findings, infection experiments with both dsDNA and ssRNA viruses showed that ANRIL is differentially regulated in a virus-dependent manner, further supporting the regulatory interplay between lncRNAs and viral infections. Consistent with previous observations in gammaherpesvirus KSHV-infected cells (75), ANRIL expression was drastically suppressed in response to the dsDNA alphaherpesviruses HSV and PrV. In KSHV, this downregulation is mediated by viral miRNAs that directly target ANRIL (75). Given that most herpesviruses encode miRNAs (209,210), this mechanism might be common during herpesvirus infections. Additionally, dsDNA viruses are known to induce the shutoff of selected host transcripts to hijack the cellular machinery and evade host immunity (211). This global suppression may involve key components of the NF- κ B pathway as well as the IFN signaling pathway. ANRIL expression has previously been shown to be driven by the NF- κ B subunit p65 in response to an inflammatory stimulus (69,172). The reduced expression of p65 in HSV- and PrV-infected cells may therefore also contribute to ANRIL suppression. This hypothesis is further supported

Discussion

by the observations in ssRNA virus infections, where both p65 and ANRIL were upregulated. Interestingly, while H3N2 is known to inhibit IFN signaling, it can redirect the antiviral NF- κ B pathway for this purpose (212). This is also reflected in the data, where H3N2 induced an increase in p65, while IFN pathway activation remained low. In contrast, CedV lacks the ability to counteract the IFN response because of the absence of IFN-antagonistic V and W proteins and the lower affinity of its phosphoprotein P for STAT1 (118). Accordingly, CedV induced the upregulation of both p65 and IFN signaling. Together, the observations suggest that ANRIL expression is regulated in a virus-dependent manner, potentially through the ability of the host cell to induce the NF- κ B and IFN signaling pathways. Several lncRNAs have been shown to be differentially expressed in response to innate immune activation. For example, NEAT1 is induced via the RIG-I-IRF7 signaling pathway during Hantaan virus infection and subsequently modulates the antiviral response (114). Similarly, ZAP-IT1 is upregulated in an IFN-dependent manner during Zika virus infection, and its knockdown enhances viral replication (213). In line with these observations, time-course analysis of CedV infection revealed that ANRIL upregulation coincides with increased expression of immune response genes, particularly those involved in IFN signaling. However, the causality of this relationship remains to be clarified.

ANRIL can promote inflammatory gene expression by guiding the transcription factor YY1 to the promoters of IL-6 and IL-8 (CXCL8) (69). Consistently, an increase in cytokine expression corresponding to an increase in the ANRIL level at 24 hpi for IL-6 and 48 hpi for IL-8 was observed. While YY1 was not among the ANRIL-binding proteins detected in the interactome screen, the INO80 Complex ATPase Subunit (INO80) was identified. Previous studies have demonstrated that INO80 binding to YY1 is essential for the DNA-binding and transcriptional activity of YY1 (177,214). INO80 treatment-IPs confirmed its interaction with all INO80 complex members, including YY1. While some lncRNAs, such as linc-MYH, have been shown to inhibit the interaction between INO80 and YY1 (215), it could be hypothesized that ANRIL may instead facilitate INO80 recruitment to YY1 target sites, leading to the expression of cytokines. The observed increased nuclear expression and localization of ANRIL in response to CedV infection further indicates a possible role in transcriptional regulation. Additionally, a functional role for INO80 in antiviral defense is suggested by the increased CedV RNA levels upon INO80 knockdown at 48 hpi. However, further analyses are needed to access the functional interplay between INO80, YY1 and ANRIL during viral infection. For example, ChIP analysis of YY1 and INO80 before and after CedV infection, combined with ANRIL knockdown, could identify shared and altered target sites. Co-IP analysis following ANRIL depletion would further help determine whether ANRIL is a necessary factor for stabilizing the interaction between YY1 and INO80. Lastly, investigating the direct effect of YY1 knockdown on CedV infection could clarify its role as a direct mediator of cytokine induction.

Discussion

Additionally to INO80, several proteins involved in innate immunity and viral replication, including members of the DExD/H-box RNA helicase family (DHX36, DHX9, and DDX3X) as well as ILF3 and ILF2 were identified as ANRIL-interacting proteins. These proteins have been implicated in regulating innate immunity and viral replication (216,217). Recently, it was shown that the lncRNA-BTX enhances viral replication, by regulating the subcellular localization of DHX9 and ILF3 (81). The association of ANRIL with these proteins could indicate a broader role in antiviral defense, although the precise molecular interplay remains to be defined. Like NEAT1 and ZAP-IT1, whose knockdown resulted in increased viral infection (114,213), we observed that ANRIL knockdown, despite its low efficiency, led to increased levels of CedV RNA and viral titers. Notably, transcriptome analysis following ANRIL knockdown identified the downregulation of several genes involved in 'viral entry', including LGALS1 (Galectin-1). Previous studies have demonstrated a protective role of Galectin-1 against the paramyxovirus NiV, where it inhibits the formation of cell-cell fusion and syncytia (166,174,218). Supporting this, increased syncytia formation was observed in CedV-infected cells upon ANRIL knockdown. Together, these findings provide initial evidence supporting a role for ANRIL in antiviral immunity in response to CedV infection, however more in-depth analyses are required to fully understand the underlying molecular mechanisms.

In summary, by systematically mapping the ANRIL interactome, the study provides a valuable resource for understanding the multifaceted roles of ANRIL in cellular regulation. The identification of a diverse range of interacting proteins, including chromatin modifiers, splicing regulators, proteins involved in ribosomal biogenesis and immune-related proteins, not only expands the understanding of ANRIL's molecular functions, but also opens new avenues for research into its role in health and disease.

Conclusion

In this study, I identified 310 ANRIL-interacting proteins using a quantitative RNA-interactomics screen, including both known and novel binding partners. Among the novel candidates, I further characterized the mostly uncharacterized protein C7orf50 and identified its interaction with proteins involved in ribosomal biogenesis. Combining the ANRIL interactome data with transcriptome-wide changes after ANRIL knockdown, I uncovered a novel function of ANRIL in viral infections. Specifically, functional analysis revealed a virus-specific regulation of ANRIL expression, with dsDNA viruses markedly downregulating and ssRNA viruses upregulating ANRIL levels. In Cedar virus infection, I identified a time- and dose-dependent regulation of ANRIL, and knockdown experiments provided the first indications of an antiviral role, as viral RNA and titers increased upon ANRIL depletion. Preliminary results further suggested that INO80, another ANRIL-interacting protein identified in this study, also increased viral RNA.

Taken together, the RNA-protein interaction screen significantly expands the known ANRIL interactome and provides a basis for further exploring its role in health and disease. Future investigations should focus on validating the newly identified interactors, establish robust knockdown/knockout and overexpression systems, and test viral infection outcomes in ANRIL-modulated models. Expanding these studies to a broader range of viruses with distinct host immune responses will help to better define ANRIL's role in antiviral defense. Additionally, the characterization of promising candidate proteins and determination whether their effects are mediated by ANRIL will be key to uncovering the underlying regulatory pathways.

Material and Methods

Materials

Buffers and Solutions

Table 1 *Buffers and Solutions*

Buffer and Solutions	Composition
RPMI cell growth medium	RPMI-1640 media 1% Pen-Strep 1% L-glutamine 10% FBS
HH-Buffer	800 mM Tris/HCl pH 7.9 0.22 M MgCl ₂ *6 H ₂ O 10 mM spermidine 50 mM DTT 1.2 g*ml ⁻¹ BSA 25 mM NTP mix in Rnase-free H ₂ O
Buffer A	10 mM HEPES/KOH pH 7.6 1.5 mM MgCl ₂ 10 mM KCl in H ₂ O
Buffer A+	Buffer A 0.1% IGEPAL CA-630 1 mM PMSF 1 μM pepstatin A 1 μg/ml leupeptin 0.5 mM DTT in H ₂ O
Buffer C+	420 mM NaCl 20 mM HEPES/KOH pH 7.6 20% glycerol 2 mM MgCl ₂ 0.2 mM EDTA pH 8.0 0.1% IGEPAL CA-630 1 mM PMSF 1 μg/ml leupeptin 1 μM pepstatin A 0.5 mM DTT in H ₂ O
RNA binding buffer	100 mM NaCl 50 mM HEPES/KOH pH 7.6 0.5% IGEPAL CA-630 10 mM MgCl ₂ in RNase-free H ₂ O
RNA wash buffer	250 mM NaCl 50 mM HEPES/KOH pH 7.6 0.5% IGEPAL CA-630 10 mM MgCl ₂ Complete Protease Inhibitor Cocktail Tablets in H ₂ O
Elution buffer	1× LDS 100 mM DTT

Material and Methods

Buffer and Solutions	Composition
Coomassie blue G-250	0.25% Coomassie blue G-250 10% acetic acid 43% ethanol
Destaining Buffer	50% ethanol 25 mM ammonium bicarbonate pH 8.0
Reduction Buffer	10 mM DTT 50 mM ABC buffer pH 8.0
Alkylation Buffer	50 mM IAA 50 mM ABC buffer pH 8.0
Trypsin Buffer	1 µg of mass spectrometry-grade trypsin 50 mM ABC buffer, pH 8.0
TE buffer	10 mM Tris HCl pH 8.0 1 mM EDTA pH 8.0
RIPA buffer	50 mM Tris/HCl pH 7.5 1% v/v IGEPAL CA-630 0.5% v/v Sodiumdeoxycholate 150 mM NaCl in UP H ₂ O
PBS-T	1x PBS 0.1% Tween in UP H ₂ O
Reconstitution buffer (SP3)	50 mM HEPES-NaOH 100 mM NaCl 1 mM EDTA 0.5% SDC 1% Triton X-1000, pH 8.0

Antibodies

Table 2 Antibodies

Target	Host	Product No.	Manufacturer	Dilution
Primary Antibodies				
Anti-GFP	Mouse	11814460001	Roche	1:1000
Anti-INO80	Rabbit	18810-1-AP	proteintech	1 µg
Secondary Antibodies				
IRDye 680RP anti-Mouse	Goat	926-68070	LI-COR	1:10.000

Reagents

Table 3 Reagents

Material	Product No.	Manufacturer
Acetonitrile (ACN)	20048320	VWR
Ammonium bicarbonate buffer, pH 8.0 (ABC)	A6141-500G	Sigma–Aldrich
BlueEye Prestained Protein Marker (10-245kDa)	PS-104	Jena Bioscience
Bradford (5x)	500-0006	Bio-Rad
BSA (20 mg/ml)	B9000S	New England BioLabs
cComplete EDTA-free Protease Inhibitor	5056489001	Roche

Material and Methods

Material	Product No.	Manufacturer
Coomassie blue G-250	902120 (HS-605)	Biozym
DPBS	14190144	Gibco
DTT	D0632-25G	Sigma–Aldrich
Dynabeads MyOne Streptavidin C1	10202333	Thermo Fisher Scientific
Ethanol ROTIPURAN> 99.8%	9065.3	Carl ROTH
Fetal Bovine Serum (FBS)	10270-106	Gibco
Formic Acid 98%	84865.180	VWR
Geneticin G418 - Sulfat 50mg/ml	A6798	AppliChem
GenRuler 1kB DNA Ladder	SM0311	Thermo Scientifc
GFP-Trap_M	gtm-20	Chromotek
Glasgow's MEM medium (GMEM)		Cell Bank, FLI
Glycerol	3783.1	Carl ROTH
HF-Polymerase		IMB CF
Hoechst 33342	62249	Thermo Fisher Scientific
ibidi mounting medium	50001	ibidi
IGEPAL CA-630	I8896-100ML	Sigma–Aldrich
Iodoacetamide (IAA)	I6125-10G	Sigma–Aldrich
Isopropanol (2-Propanol) >99.5%	CP41.3	Carl ROTH
LB Agar (Luria/Miller), granulated	6675.2	ROTH
LB Broth (Luria/Miller)	X968.2	ROTH
LCMS-grade ethanol	1.11727.1000	Merck
LCMS-grade H ₂ O	23595.328	VWR
Leupeptin	51867.03 (50 mg)	SERVA Electrophoresis GmbH
L-Glutamin (200 mM)	G7513-100ML	Sigma–Aldrich
Lipofectamine RNAiMAX	12323563	Thermo Fisher Scientific
Methanol	208643.20	VWR
MgCl ₂ *6 H ₂ O	M2670-500G	Sigma–Aldrich
MnCl ₂ [200mM] (10x)	B0786A	New England BioLabs
MW 25.000 Linear polyethylenimine	23966-2	Polysciences Inc.
NEB® 5-alpha Competent E. coli (High Efficiency)	C2987H	New England BioLabs
Newborn Calf Serum (NCS)	S-NC-NZ-035	Serana Europe GmbH
NTP Bundle (100 mM)	NU-1014S.1	Jena Bioscience
NuPage MES buffer (20x)	NP0002	Thermo Scientific
NuPAGE Novex 4–12% Bis-Tris gradient SDS gel	10472322	Thermo Scientific
NuPAGE™ LDS-Probenpuffer (4x)	11559166	Thermo Fisher Scientific
OptiMEM	11058021	Thermo Fisher Scientific
Paraformaldehyde (PFA)	0335.3	Carl Roth
Penicillin-Streptomycin (Pen-Strep)	P0781-100ML	Sigma–Aldrich
Pepstatin A	52682.03	SERVA Electrophoresis GmbH
Phenol/Chloroform 5:1, pH 4,3-4,7	P1944-100ml	Sigma–Aldrich
Phenylmethylsulfonyl fluoride (PMSF)	32395.03 (25 g)	SERVA Electrophoresis GmbH

Material and Methods

Material	Product No.	Manufacturer
Poly-L-lysine	P8920-100ML	Sigma–Aldrich
Ponceaus S Staining Solution	A40000279	Thermo Scientific
ProLong™ Glass Antifade Mountant	P10144	Thermo Fisher Scientific
Protein A magnetic Dynabeads	10002D	Invitrogen
Proteinase K solution	59895	Invitrogen
RiboLock RNase Inhibitor (40 U/μl)	EO0382	Thermo Fisher Scientific
Ribonuclease A from bovine pancreas Type I-AS, 50-100 Kunitz units/mg protein (RNase A)	R5503-100MG	Sigma-Aldrich
RNase III	M0245S	New England Biolabs
ROTI®PreMix PBS	0890.2	ROTH
RPMI-1640 media	31870025	Gibco
Sera-Mag Carboxylate-Modified Magnetic Particles (Hydrophilic) (50mg/ml)	24152105050250	GE Healthcare
Sera-Mag Carboxylate-Modified Magnetic Particles (Hydrophobic) (50mg/ml)	44152105050250	GE Healthcare
ShortCut buffer (10x)	B0245S	New England BioLabs
Skim Milk Powder (MP)	70166-500G	Sigma-Aldrich
SOC Outgrowth Medium	B9020S	New England BioLabs
Spermidine	S2626-5G	Sigma–Aldrich
SYBR™ Safe	10328162	Invitrogen
T7 RNA Polymerase, HC (200 U/μL)	EP0113	Thermo Fisher Scientific
Taq Polymerase		IMB CF
Triton X-100	A16046.AE	Fisher Scientific
Trypsin (Proteomics Grade)	EC 3.4.21.4	Serva
TRYPsin 0.25% EDTA	25200056	Sigma–Aldrich
Tryptose-Phosphat-Bouillon	11500546	Invitrogen
Tween 20	P7949-100ML	Sigma-Aldrich
UltraPure™ DNase/RNase-Free Distilled Water	10977049	Invitrogen

Commercial assays

Table 4 Commercial assays

Material	Product No.	Manufacturer
Agilent High Sensitivity DNA Kit	5067-4626	Agilent
dsDNA High Sensitivity Kit	Q32851	Invitrogen
First Strand cDNA Synthesis Kit	K1612	Thermo Fisher Scientific
Gateway™ LR Clonase™ II Enzym-Mix	10134992	Invitrogen
microRNA Assay-Kit	15401563	Thermo Fisher Scientific
Power SYBR Green PCR Master Mix	4367659	Thermo Fisher Scientific
Q Sepharose Fast Flow Kit	17-0510-10	Cytiva
QIA RNeasy Mini Kit (50)	74104	Qiagen
QIAGEN Plasmid Midi Kit (25)	12143	Qiagen
QIAprep Spin Miniprep Kit (50)	27104	Qiagen

Material and Methods

Material	Product No.	Manufacturer
QuantSeq 3' mRNA-Seq FWD Kit	191.96	Lexogen
RNA 6000 Nano Kit	NC1783726	Agilent
RNase-Free DNase Set (250)	79256	Qiagen
Thermo Scientific™ Pierce™ BCA Protein Assay Kits	10678484	FisherSci
TruSeq stranded mRNA LP Sample Prep Kit		Illumina
ViewRNA™ ISH Cell Assay Kit	VA6-3189669	Thermo Fisher Scientific

Consumables

Table 5 Consumables

Material	Product No.	Manufacturer
μ-Dish 35 mm Imaging Chamber	81156	Ibidi
12 mm cover slips	YX03.2	Carl Roth
Amersham™ Protran 0.45 NC nitrocellulose	15259794	Fisher Scientific
Aurora Ultimate™ 25×75 C18 UHPLC column		ionopticks
Deepwell plate (96/1000 μl)	951032603	Eppendorf
Empore disk-C18, 47 MM	12145004	Empore
MultiScreenHTS BVFilterplatte (96 well)	MSBVN1210	Merck
Tissue culture dish 100x20	353003	Corning
Tissue culture plate 12-well	353043-1	Corning
Tissue culture plate 24-well	353047-1	Corning
Tissue culture plate 6-well	353046-1	Corning

Instruments

Table 6 Instruments

Device	Manufacturer
2100 Bioanalyzer	Agilent
CFX Opus 96 Real-Time PCR System	Bio-Rad
CO2 Incubator MCO-19AIC	SANYO
Concentrator Plus	Eppendorf
DMi8 (Thunder)	Leica
DynaMag2	Thermo Scientific
Easy nLC 1000 system	Thermo Fisher Scientific
Fresco 21	Thermo Scientific
GloMax Discover Microplate Reader	Promega
Illumina NextSeq2000	Illumina
Leica Stellaris 8 confocal microscope	Leica Microsystems
Multifuge X3R	Thermo Fisher Scientific
Nanodrop 2000	Thermo Fisher Scientific
nanoElute HPLC	Bruker
NanoPhotometer	Implen
Odyssey® CLx Imaging Systems	LI-COR

Material and Methods

Device	Manufacturer
PC 3001 VARIO select	VACUUBRAND
Ultraspec 2100 Pro Spectrophotometer	Amersham Bioscience
Q Exactive Plus mass spectrometer	Thermo
Qubit 4.0 fluorometer	Thermo Fisher Scientific
Thermocycler Tprofessional BASIS (+Modul)	Biometra Analytik Jena
Thermocycler Tprofessional TRIO 48	Biometra Analytik Jena
Thermomixer comfort	Eppendorf
timsTOF HAT	Bruker

Primers

Table 7 Primers

Fragment	Name	Sequence (5'-3')
esiRNA Primers		
esiANRIL	ANRIL_for	TCACTATAGGGAGAGAAGTTAAATAATTTTCCTGT
	ANRIL_rev	TCACTATAGGGAGACACCCCGTCTCTACTGTTACC
esiINO80	INO80_for	TCACTATAGGGAGAGAACTGACCAGCCGACAGAAG
	INO80_rev	TCACTATAGGGAGACTTGCCATTCTGCTGGAGAT
esiRLuc	RLuc_for	TCACTATAGGGAGAGGATAACTGGTCCGAGTGGT
	RLuc_rev	TCACTATAGGGAGACCCATTCCATCCCATGATTCAA
Fragment Preparation for ANRIL Interactome Screen		
pDEST17_350nt	T7_pDEST17 for 350nt	CGTTAATACGACTCACTATAGGATCGGTTCGATCGACGCTCTC
	pDEST17_apt rev1	CATGGCCCCGCCGCGACTATCTTACGCACTTGCATGATTCTGGTCGGTCCCATGGATCCCGATCCTCTACGCCGGAC
pDEST17_750nt	T7_pDEST17 for 785bp	CGTTAATACGACTCACTATAGGTGAAGCTGTCCCTGATGGTC
	pDEST17_apt rev1	CATGGCCCCGCCGCGACTATCTTACGCACTTGCATGATTCTGGTCGGTCCCATGGATCCCGATCCTCTACGCCGGAC
Exon 1	T7-Ex1-fw	CGTTAATACGACTCACTATAGGAGCTACATCCGTCACCTGACACGGCCCTAC
	Ex1-Apt-rev	CATGGCCCCGCCGCGACTATCTTACGCACTTGCATGATTCTGGTCGGTCCCATGGATCCCTAGTCCGGCGCCAGGCCG
Exon 2	T7-Ex2-fw	CGTTAATACGACTCACTATAGGGACTATTTGCCACGACATTTCAAAGG
	Ex2-Apt-rev	CATGGCCCCGCCGCGACTATCTTACGCACTTGCATGATTCTGGTCGGTCCCATGGATCCAGCAATAGGTGTGGCCCTCAG
Exon 3	T7-Ex3-fw	CGTTAATACGACTCACTATAGGGCAATTTATAGCACTGATCTG
	Ex3-Apt-rev	CATGGCCCCGCCGCGACTATCTTACGCACTTGCATGATTCTGGTCGGTCCCATGGATCCCTGCTGCCACCTTCTGCTG
Exon 4_5	T7-Ex4and5-fw	CGTTAATACGACTCACTATAGGATATTGAGAAACCACAG
	Ex4and5-Apt-rev	CATGGCCCCGCCGCGACTATCTTACGCACTTGCATGATTCTGGTCGGTCCCATGGATCCCTCTCTTTCCAAGAAAATTC
Exon 6_7	T7-Ex6and7-fw	CGTTAATACGACTCACTATAGGGGTTCAAGCATCAC
	Ex6and7-Apt-rev	CATGGCCCCGCCGCGACTATCTTACGCACTTGCATGATTCTGGTCGGTCCCATGGATCCCTGTCAAATTTCTCTATCC
Exon 8.1	T7-Ex8.1-fw	CGTTAATACGACTCACTATAGGTCTCTCCAATGAACGCC
	Ex8.1-Apt-rev	CATGGCCCCGCCGCGACTATCTTACGCACTTGCATGATTCTGGTCGGTCCCATGGATCCGTTCTAAGTGACTTCAG
Exon 8.2	T7-Ex8.2-fw	CGTTAATACGACTCACTATAGGTTGGACTGATGGAACG

Material and Methods

Fragment	Name	Sequence (5'-3')
	Ex8.2-Apt-rev:	CATGGCCCCGCCCGCGACTATCTTACGCACTTGCATGATTCTGGTCGGTCCCATGGATCC CTTGAATTGTTTCTCCAG
Exon 9_11	T7-Ex9to11-fw	CGTTAATACGACTCACTATAGGATATGACACATTCATAA
	Ex9to11-Apt-rev	CATGGCCCCGCCCGCGACTATCTTACGCACTTGCATGATTCTGGTCGGTCCCATGGATCC CTGGAGTGTGACTGCACTG
Exon 12_15	T7-Ex12and15-fw	CGTTAATACGACTCACTATAGGACAGGGTCTCACTC
	Ex12and15-Apt-rev	CATGGCCCCGCCCGCGACTATCTTACGCACTTGCATGATTCTGGTCGGTCCCATGGATCC CTATGTAGATCATGGATTTG
Exon 16_17	T7-Ex16and17-fw	CGTTAATACGACTCACTATAGGGTGGAGAACTTCAG
	Ex16and17-Apt-rev	CATGGCCCCGCCCGCGACTATCTTACGCACTTGCATGATTCTGGTCGGTCCCATGGATCC CAGTGGTGGATGTTGTAG
Exon 18_19	T7-Ex18and19-fw	CGTTAATACGACTCACTATAGGGATCTTAACATAGACG
	Ex18and19-Apt-rev	CATGGCCCCGCCCGCGACTATCTTACGCACTTGCATGATTCTGGTCGGTCCCATGGATCC CTACTGGATCACAGACCAT
Exon 20	T7-Ex20-fw	CGTTAATACGACTCACTATAGGTATCTTACAGACAGCAAG
	Ex20-Apt-rev	CATGGCCCCGCCCGCGACTATCTTACGCACTTGCATGATTCTGGTCGGTCCCATGGATCC TTATGCAGTAGCTACAAG
Exon 21.1	T7-Ex21.1-fw	CGTTAATACGACTCACTATAGGGTTAGGAAATTGAAATAC
	Ex21.1-Apt-rev	CATGGCCCCGCCCGCGACTATCTTACGCACTTGCATGATTCTGGTCGGTCCCATGGATCC TGATGATGATGATAATGATG
Exon 21.2	T7-Ex21.2-fw	CGTTAATACGACTCACTATAGGTCATCATCATCATTATCATCACCATAG
	Ex21.2-Apt-rev	CATGGCCCCGCCCGCGACTATCTTACGCACTTGCATGATTCTGGTCGGTCCCATGGATCC TTTTTATTGTCTGAGCCAGTTTTATTTTG
Sequencing Primer		
GFP	EGFP_C	CATGGTCCTGCTGGAGTTCGTG
qPCR primer		
ANRIL	ANRIL_Ex5_for	ACACATCAAAGGAGAATTTTCTTGG
	ANRIL_Ex5_rev	GTACTGACTCGGGAAGGATTC
INO80	INO80_for	GGGAGAGCCACCAGAGATAC
	INO80_rev	ACAACCTGGTCTGAGTAGCC
HSV	HSV_KOS_ICP8_for	CCACGCCACCAGGCTGATGAC
	HSV_KOS_ICP8_rev	TGCTTACGGTCAGGTGCTCCG
PrV_gB	PrV_gB_for	ACAAGTTCAAGGCCCATCTAC
	PrV_gB_rev	GTCYGTGAAGCGGTTCTGTAT
H3N2_M1	H3N2_M1_for	AGATGAGCCTTCTAACCGAGGTCTG
	H3N2_M1_rev	AGCAAAGACATCTTCAAGTCTCTG
CedV	CedV_Pgene_for	TGCATTGAGCGAACCCATATAC
	CedV_Pgene_rev	GCACGCTTCTTGACAGAGTTGT
p65	NFKB1_p65_for	TGAACCGAAACTCTGGCAGCTG
	NFKB1_p65_rev	CATCAGCTTGCGAAAAGGAGCC
18S-rRNA	18S_rRNA_qPCR_for	CCAGTAAGTGCGGGTCATAAGC
	18S_rRNA_qPCR_rev	GCCTCACTAAACCATCCAATCGG
β-Actin	β-actin_for	TGTACGCCAACACAGTGCTG
	β-actin_rev	GCTGGAAGGTGGACAGCGA

Material and Methods

Fragment	Name	Sequence (5'-3')
GAPDH	GAPDH_for	GTCTCCTCTGACTTCAACAGCG
	GAPDH_rev	ACCACCCTGTTGCTGTAGCCAA

Methods

Cell culture

HeLa S3 and HeLa Kyoto cells were grown in RPMI-1640 media (Gibco) supplemented with 1% Pen-Strep (Sigma–Aldrich), 1% L-glutamine (Sigma–Aldrich) and 10% FBS (Gibco). BSR-T7/5 cells were grown in Glasgow’s MEM medium (GMEM) (Cell Bank, FLI) containing 10% NCS (Serana Europe GmbH), tryptose phosphate (Invitrogen) and 1% Pen-Strep (Sigma–Aldrich). Additionally, cells were supplemented once a week with Geneticin (G418 sulfate; 1mg/mL [AppliChem]). Cells were propagated after reaching around 80-90% confluency, in desired dilution (1:2 – 1:20). Briefly, the old medium was aspirated, the cells washed with 1x DPBS (Gibco), detached using 0.25% trypsin (Sigma–Aldrich) and resuspended in fresh media. All cell lines were kept in a humidified incubator at 37 °C, 5% CO₂ and 70% humidity.

Plasmids

The pUC19 ANRIL (NR_003529.3) vector was purchased from GenScript and used as a template to amplify exons for the RBPome screen as well as the esiRNA for the ANRIL knockdown. C7orf50 (Q9BRJ6; GDEhKL_012) and INO80 (Q9ULG1; GDEh81132) pDONR223 vectors, containing recombination sites for LR-cloning, were obtained from the IMB ORFeome library (IMB).

Nuclear extract preparation from cell lines

HeLa S3 cells were grown in RPMI-media in a humidified incubator at 37 °C, 5% CO₂ and 70% humidity. Nuclear extracts were prepared as described previously (180,219). Briefly, the cells were collected in 50 ml tubes and centrifuged for 5 min at 400 × g at RT (Multifuge X3R [Thermo Fisher Scientific]). The pellets were washed with PBS (Gibco) and pooled, followed by centrifugation at 400 × g for 5 min at RT (Multifuge X3R [Thermo Fisher Scientific]). To lyse the cells, the pellets were resuspended in five volumes of cold Buffer A (10 mM HEPES/KOH pH 7.6, 1.5 mM MgCl₂, and 10 mM KCl in H₂O) and incubated on ice for 10 min to induce swelling. After centrifugation at 500 × g for 5 min at 4 °C (Multifuge X3R [Thermo Fisher Scientific]), the pellets were resuspended in two volumes of Buffer A+ (Buffer A supplemented with 0.1% IGEPAL CA-630 [Sigma–Aldrich], 1 mM PMSF [SERVA Electrophoresis GmbH], 1 μM pepstatin A [SERVA Electrophoresis GmbH], 1 μg/ml leupeptin [SERVA Electrophoresis GmbH], 0.5 mM DTT [Sigma–Aldrich]). To extract nuclear proteins, the cell suspension was transferred

Material and Methods

into a douncer and homogenized with 50 strokes using a type B pestle. The homogenized samples were pooled and centrifuged at $1.500 \times g$ for 15 min at $4\text{ }^{\circ}\text{C}$ (Multifuge X3R [Thermo Fisher Scientific]). The cytoplasmic supernatant was transferred into 2 ml tubes and centrifuged at maximum speed for 1 h at $4\text{ }^{\circ}\text{C}$ (Fresco 21 [Thermo Scientific]). The resulting supernatant was pooled, and glycerol was added to a final concentration of 10% before storing aliquots at $-80\text{ }^{\circ}\text{C}$ after snap-freezing them in liquid nitrogen. For the nuclear fraction, the pellet was washed in 10 volumes of PBS (Gibco), centrifuged at $3.900 \times g$ for 5 min at $4\text{ }^{\circ}\text{C}$ (Multifuge X3R [Thermo Fisher Scientific]), and resuspended in two volumes of Buffer C+ (420 mM NaCl, 20 mM HEPES/KOH pH 7.6, 20% glycerol, 2 mM MgCl_2 , 0.2 mM EDTA pH 8.0 in H_2O supplemented with 0.1% IGEPAL CA-630, 1 mM PMSF, 1 μM pepstatin A, 1 $\mu\text{g}/\text{ml}$ leupeptin, 0.5 mM DTT [Sigma–Aldrich]). The samples were transferred into 2 ml tubes and incubated on a rotation wheel at $4\text{ }^{\circ}\text{C}$ for 1 h, followed by centrifugation at maximum speed for 1 h at $4\text{ }^{\circ}\text{C}$ (Fresco 21 [Thermo Scientific]). The supernatants were pooled, and aliquots were snap-frozen in liquid nitrogen before being stored at $-80\text{ }^{\circ}\text{C}$. The protein concentration was determined via Bradford with a premixed solution (Bio-Rad) via a photometer (Amersham Bioscience) and calculated using a linear regression on the basis of a standard dilution series of BSA (Sigma–Aldrich).

Preparation of RNA Fragments for the ANRIL interactome

ANRIL fragments were prepared using the workflow published by Butter et al. (146). In total, 14 nonoverlapping fragments (with lengths ranging from 223-409 nt) were PCR amplified via HF-DNA polymerase (Protein Production, IMB Mainz) with specific primers (Table 7), which contained a T7 promoter sequence at the 5'-end and a minimal S1 aptamer sequence (145) at the 3'-end. A 350 nt control fragment was amplified from a pDEST17 vector (Thermo Fisher Scientific). The correct size of the PCR products were validated via agarose gel electrophoresis. To synthesize the RNA, the DNA template was *in vitro* transcribed overnight at $37\text{ }^{\circ}\text{C}$ using 200 units of T7 RNA polymerase (Thermo Fisher Scientific), 1x HH buffer (800 mM Tris/HCl pH 7.9, 0.22 M $\text{MgCl}_2 \cdot 6\text{ H}_2\text{O}$ [Sigma–Aldrich], 10 mM spermidine [Sigma–Aldrich], 50 mM DTT [Sigma–Aldrich], 1.2 $\text{g} \cdot \text{ml}^{-1}$ BSA [New England BioLabs]), 25 mM NTP mix [Jena Bioscience]) in RNase-free H_2O . Successful transcription was verified by agarose gel electrophoresis. The RNA was purified by phenol-chloroform extraction as previously described (180). In brief, RNA was diluted in RNase-free H_2O and roughly mixed with 5:1 phenol/chloroform (Sigma–Aldrich). The mixture was centrifuged for 2 min at $9.600 \times g$ at RT, and the aqueous phase was transferred into a new tube. The RNA was precipitated by adding absolute ethanol, followed by incubation at $-80\text{ }^{\circ}\text{C}$ for 10 min. The sample was subsequently centrifuged at $4\text{ }^{\circ}\text{C}$ for 1 h at $21.100 \times g$ (Fresco 21 [Thermo Scientific]), after which the supernatant was removed. The pellet was air-dried and

Material and Methods

resuspended in RNase-free H₂O. The RNA concentration was determined with a microvolume spectrophotometer (Nanodrop 2000 [Thermo Fisher Scientific], NanoPhotometer [Implen]).

Pulldown

For each sample, 6 µg of S1-tagged RNA was immobilized on 25 µl of paramagnetic streptavidin beads (Dynabeads MyOne Streptavidin C [Thermo Fisher Scientific]) in RNA binding buffer (100 mM NaCl, 50 mM HEPES/KOH pH 7.6, 0.5% IGEPAL CA-630 [Sigma–Aldrich], 10 mM MgCl₂, and RNase-free H₂O) at 4 °C for 30 min on a rotation wheel. A magnetic rack (DynaMag2 [Thermo Scientific]) was used to wash the beads three times with RNA binding buffer to remove unbound RNA. The beads were then incubated with 400 µg of nuclear HeLa S3 extract and 20 µg of yeast tRNA (Thermo Fisher Scientific) as a competitor in RNA wash buffer (250 mM NaCl, 50 mM HEPES/KOH pH 7.6, 0.5% IGEPAL CA-630, 10 mM MgCl₂, Complete Protease Inhibitor Cocktail Tablet [Roche] and RNase-free H₂O) at 4 °C for 30 min on a rotation wheel. Following incubation, the beads were washed three times with RNA wash buffer to remove unbound proteins via a magnetic rack. The bound proteins were then eluted via resuspension in 1× elution buffer (1× LDS [Thermo Fisher Scientific] supplemented with 100 mM DTT [Sigma–Aldrich]) and incubated at 70 °C for 10 min at 1400 rpm via a Thermomixer (Eppendorf). The experiment was conducted in two batches (Ex1 to Ex8part1 with CTRL1 and Ex9till11 to Ex21part2 with CTRL2) with four biochemical replicates per RNA fragment.

Mass spectrometry sample preparation and measurement

Pulldowns, Immunoprecipitations (IP) and Proteome samples were prepared for mass spectrometry following a previously published in-gel sample preparation protocol (180,220). For proteome measurements 20 to 25 µg of protein extract was resuspended in 1× elution buffer (1× LDS [Thermo Fisher Scientific] supplemented with 100 mM DTT [Sigma–Aldrich]) and incubated at 70 °C for 10 min at 1400 rpm via a Thermomixer (Eppendorf).

The proteins were separated on a NuPAGE Novex 4–12% Bis-Tris gradient SDS gel (Thermo Scientific) for 8 min at 180 V in 1× NuPage MES buffer (Thermo Scientific) and stained with Coomassie blue G-250 (0.25% Coomassie blue G-250 [Biozym], 10% acetic acid, 43% ethanol) prior to overnight destaining in H₂O. The minced gel lanes were transferred into a 1.2 µm 96-well filter plate (Merck) containing destaining buffer (50% ethanol in 25 mM ammonium bicarbonate (ABC) buffer, pH 8.0 [Sigma–Aldrich]) and incubated at 37 °C for 15 min. After each incubation, the buffer was removed using a vacuum pump and replaced with fresh buffer until the samples were completely destained. The gel pieces were incubated in 50 mM ABC buffer for 10 min at 37 °C, followed by three dehydration steps with 100% acetonitrile (ACN) (VWR) at 25 °C for 10 min each. Proteins were reduced (10 mM DTT [Sigma–Aldrich],

Material and Methods

50 mM ABC buffer pH 8.0, 56 °C, 60 min, 300 rpm) and alkylated (50 mM IAA [Sigma–Aldrich], 50 mM ABC buffer pH 8.0, RT, 45 min, in the dark). The gel pieces were again incubated in ABC buffer (pH 8.0) and dehydrated. Trypsin digestion was performed overnight at 37 °C with 1 µg of mass spectrometry-grade trypsin (Serva) in 50 mM ABC buffer, pH 8.0. The peptides were extracted twice using 30% ACN in H₂O, followed by three dehydration steps with 100% ACN via centrifugation (300 × g, Heraeus Multifuge X3R [Thermo Fisher Scientific]). The extracted peptides were transferred into 1.5 ml reaction tubes, dried with a Concentrator Plus (Eppendorf) and loaded onto self-made StageTips (221) with two layers of methanol-activated C18 material (Empore). For pulldowns and IPs peptides were separated on a self-packed Reprisil C18 (Dr. Maisch GmbH, 20 cm, 75 µm) capillary column (New Objective) via an Easy nLC 1000 system (Thermo Fisher Scientific) with an 88-min optimized gradient increasing from 2% to 32% ACN in 0.1% formic acid at 225 nl*min⁻¹. The capillary was mounted on a Q Exactive Plus mass spectrometer (Thermo) and operated with a Top10 data-dependent MS/MS acquisition in the Orbitrap analyzer.

For proteome measurements peptide concentration was determined prior to loading using BCA protein assay (Fisher Scientific). Shortly, eluted peptides and BSA standard dilution series (Sigma–Aldrich) were incubated for 30 min at 60 °C in a Thermomixer (Eppendorf) at 300 rpm. Absorbance was measured via GloMax Discover Microplate Reader (Promega) at 560 nm, and peptide concentrations calculated based on linear regression of the BSA standard curve. A total of 400 ng peptides were separated on an Aurora Ultimate™ 25×75 C18 UHPLC column (ionopticks) using a nanoElute HPLC system (Bruker). Separation was conducted with a 100-min gradient at a constant flow rate of 300 nl*min⁻¹ with increasing ACN concentration from 2% MS-grade ACN/0.1% formic acid (0-2 min) to 17% (2-67min), 27% (67-88 min), 95% (88-97 min) and 4% (97-100 min). The capillary was mounted on a timsTOF HT mass spectrometer (Bruker) operated in a standard PASEF data-dependent acquisition mode with a cycle time of 1.1 sec.

The raw files were processed with MaxQuant (version 1.6.5.0 for the ANRIL interactome screen and 2.4.2.0 for all other datasets) and searched against the SwissProt (42,338 entries) and Trembl (54,436 entries) (UP000005640, v20200117) *Homo sapiens* databases. To detect RNase A in the treatment-IPs, a custom FASTA file containing the *Bos taurus* amino acid (AA) sequence (NP_001014408.2) was included. For viral protein identification, the following FASTA files were used: PrV-Kaplan (JF797218.1; 2011), H3N2 A/Victoria/1975 (ASM3860483v1 (GCA_038604435.1); 2014) and Herpes simplex virus 1 (BK012101.1; 2020). For recombinant CedV, the nucleotide sequences of all viral proteins (JQ001776.1), including the reporter gene nTurboFP635, were translated into all possible reading

Material and Methods

frames using the built in Six-frame translation tool of MaxQuant (2.4.2.0), with a minimal AA length of 20. Data analysis was performed using R-studio (version [2023.06.1]).

LR recombination to N-terminally tag C7orf50

To tag and express C7orf50, the ORF of C7orf50 (Q9BRJ6; GDEhKL_012) was obtained from the IMB ORFeome library (IMB) and recombined into a V10-pcDNA4/GFP destination vector using the Gateway™ LR Clonase™ II Enzym-Mix (Invitrogen). Shortly, 150 ng of the entry vector pDONR223 was combined with 150 ng destination vector and 1 µl LR clonase II enzyme mix, adjusted to 4 µl with TE buffer (pH 8). The reaction was incubated at 25 °C for 1 h and terminated by adding 1 µl Proteinase K solution (Invitrogen), followed by a 10 min incubation at 37 °C. The recombinant products were transformed in 50 µl NEB® 5-alpha (New England BioLabs) and validated by sequencing.

Bacterial transformation and plasmid extraction

For routine plasmid propagation, constructs were transformed into chemically competent *E. coli* bacterial cells via heat shock. Briefly, NEB® 5-alpha cells (New England BioLabs) were thawed on ice, mixed with desired amount of plasmid DNA and incubated on ice for 30 min. To introduce the plasmids into the bacterial cells, cells were heat shocked for 30 sec at 42 °C, followed by recovery in 300 µl SOC outgrowth medium (New England BioLabs). Cells were incubated at 37 °C for 1 h to express antibiotic resistance, plated onto LB agar plates containing the appropriate antibiotic and incubated overnight at 37 °C. For smaller amounts of plasmid, extraction was prepared with the Plasmid Mini Kit from Qiagen according to the manufacturer's instructions.

For larger amounts, the Plasmid Midi Kit from Qiagen was used, with some alterations to use without an ultracentrifuge. Shortly, 100 ml overnight culture was harvested by centrifugation at 4816 × g for 15 min at 4 °C (Multifuge X3R [Thermo Fisher Scientific]). Bacterial pellets were resuspended in 4 ml Buffer P1 and incubated for 5 min at RT after addition of 4 ml Buffer P2 to allow cell lysis. Lysis was neutralized by adding 4 ml chilled Buffer P3 and incubation for 15 min on ice, followed by a 30 min centrifugation at 4816 × g (Multifuge X3R [Thermo Fisher Scientific]). The cleared supernatant was passed through a mesh band and loaded onto a Buffer QBT-equilibrated QIAGEN tip to filter out residual cell debris. The column was washed twice with 10 ml Buffer QC and DNA eluted with 5 ml Buffer QF into a 15 ml tube. DNA was precipitated by adding 3.5 ml isopropanol (Carl ROTH) and splitting the sample into 2 ml tubes followed by a centrifugation at maximum speed for 30 min at 4 °C (Fresco 21 [Thermo Scientific]). Pellets were washed with 400 µl 70% ethanol, combined into one tube, and centrifuged again for 10 min at 4 °C at maximum speed (Fresco 21 [Thermo Scientific]). The resulting pellet was air-dried and dissolved in 500 µl H₂O.

Material and Methods

Plasmid concentrations were determined using a microvolume spectrophotometer (NanoPhotometer [Implen]) or via the dsDNA High Sensitivity Kit with a Qubit 4.0 Fluorometer (Thermo Fisher Scientific). Correct sequences were validated via Sanger (Eurofins) or Whole Plasmid sequencing (Eurofins).

Linear polyethylenimine (PEI) transient transfection of GFP-C7orf50

Linear polyethylenimine (PEI, MW 25.000; Polysciences) was used to express GFP-tagged C7orf50 in HeLa Kyoto cells. One day prior to the transfection, 2×10^6 HeLa Kyoto cells were seeded into a 10 cm cell culture dish. For transfection, 72 μ l PEI was mixed with 428 μ l 1x OptiMEM (Thermo Fisher Scientific) in one tube and 18 μ g plasmid in 500 μ l 1x OptiMEM was added to a separate tube. Both reactions were incubated for 5 min at RT before being combined and incubated for an additional 20 min at RT. Meanwhile, growth medium was replaced with 1x OptiMEM. The transfection mix was added dropwise to the cells, which were then incubated for 6 h at 37°C and 5% CO₂ in a humidifier incubator. After the incubation, the transfection medium was replaced with fresh growth medium, and protein extraction was performed after 48 h.

Extracting protein from eukaryotic cells

Radioimmunoprecipitation assay (RIPA) buffer (50 mM Tris/HCl pH 7.5, 1% v/v IGEPAL CA-630, 0.5% v/v Sodiumdeoxycholate, 150 mM NaCl in UP H₂O) supplemented with 1 mM pepstatin A (SERVA Electrophoresis GmbH), 1 mg/ml leupeptin (SERVA Electrophoresis GmbH), 100 mM PMSF (SERVA Electrophoresis GmbH) and 0.5 M EDTA was used to extract proteins from HeLa Kyoto cells. Briefly, cells were detached, transferred into 2 ml tubes and centrifuged at 300 \times g for 5 min (Fresco 21 [Thermo Scientific]). Pellets were resuspended, depending on its size, in 100-200 μ l supplemented RIPA buffer and incubated for 30 min on ice. Samples were vortexed and centrifuged for 10 min at 4 °C at 10.000 \times g (Fresco 21 [Thermo Scientific]). Supernatants were transferred into new tubes and 10% glycerol (Carl Roth) was added. Protein concentration was determined either by Bradford with a premixed solution (Bio-Rad) via a photometer (Amersham Bioscience) or BCA protein assay (Fisher Scientific) measured on a GloMax Discover Microplate Reader (Promega). A linear regression on the basis of a standard dilution series of BSA (Sigma–Aldrich) was used to calculate protein concentration. Samples were snap-frozen in liquid nitrogen before being stored at -80 °C.

Western Blot for the validation of C7orf50 binding to ANRIL

To validate the binding of C7orf50 to ANRIL, the initial RNA pulldown was repeated using HeLa Kyoto extract containing N-terminally tagged GFP-C7orf50 and the RNA fragments Ex16u17 and pDEST17 including an empty beads control. For the RNA fragments, 6 μ g of S1-tagged RNA was immobilized on

Material and Methods

25 µl of paramagnetic streptavidin beads (Dynabeads MyOne Streptavidin C [Thermo Fisher Scientific]) in RNA binding buffer (100 mM NaCl, 50 mM HEPES/KOH pH 7.6, 0.5% IGEPAL CA-630 [Sigma–Aldrich], 10 mM MgCl₂, and RNase-free H₂O) at 4 °C for 30 min on a rotation wheel. As a control, an equivalent volume of beads was incubated with RNA binding buffer under identical conditions, but without RNA. A magnetic rack (DynaMag2 [Thermo Scientific]) was used to wash the beads three times with RNA binding buffer to remove unbound RNA. The beads were then incubated with 10 µg of HeLa Kyoto extract containing GFP-C7orf50 and 20 µg of yeast tRNA (Thermo Fisher Scientific) as a competitor in RNA wash buffer (250 mM NaCl, 50 mM HEPES/KOH pH 7.6, 0.5% IGEPAL CA-630, 10 mM MgCl₂, Complete Protease Inhibitor Cocktail Tablets [Roche]) at 4 °C for 30 min on a rotation wheel. Following incubation, the beads were washed three times with RNA wash buffer to remove unbound proteins via a magnetic rack. The bound proteins were then eluted via resuspension in 1× elution buffer (1× LDS [Thermo Fisher Scientific] supplemented with 100 mM DTT [Sigma–Aldrich]) and incubated at 70 °C for 10 min at 1400 rpm via a Thermomixer (Eppendorf). Additionally, 10% Input was prepared in 1 x elution buffer.

For the western blot, eluted samples were loaded onto a NuPAGE Novex 4–12% Bis-Tris gradient SDS gel (Thermo Scientific) and separated for 45 min at 180 V in 1× NuPage MES buffer (Thermo Scientific). As a marker for later size orientation 4 µl of BlueEye prestained protein marker (Jena Bioscience) was used. Proteins were transferred onto a 0,45 µm nitrocellulose membrane (Fisher Scientific) via wet transfer in 1x transfer buffer (20% EtOH absolut, 10% transferbuffer in DI H₂O). Prior to antibody detection, the membrane was stained with Ponceaus S (Thermo Scientific) to confirm proper transfer. Membrane was blocked with 10% skim milk powder (MP; Sigma-Aldrich) in PBS-T (0.1% Tween 20 [Sigma-Aldrich]) for 1 h at RT. The blocking solution was discarded and replaced with 5% MP-PBS-T including 1:1000 primary anti-GFP antibody (Roche) and incubated overnight at 4 °C while gently rocking. On the next day, the membrane was washed three times for 10 min in PBS-T at RT. The membrane was then incubated for 1 h at RT with 5% MP-PBS-T containing 1:10.000 fluorescent secondary anti-Mouse antibody (IRDye 680RP, LI-COR). Before detection, the membrane was washed three times in PBS-T and imaged using the Odyssey® CLx Imaging Systems (LI-COR).

Treatment-Immunoprecipitation (IP)

GFP-IP C7orf50

To identify interacting proteins of C7orf50, 14 µL GFP-Trap_M beads (Chromotek) were washed three times with 200 µl RNA wash buffer (250 mM NaCl, 50 mM HEPES/KOH pH 7.6, 0.5% IGEPAL CA-630, 10 mM MgCl₂, Complete Protease Inhibitor Cocktail Tablet [Roche]) using a magnetic rack (DynaMag2 [Thermo Scientific]). For the bead-only control (CTRL), 45 µl GFP beads were incubated with 355 µl RNA

Material and Methods

wash buffer. For C7orf50, 90 μ l GFP beads pre-incubated with 900 μ g GFP-C7orf50 total cell extract in 400 μ l RNA wash buffer. All samples were incubated for 30 min on a rotation wheel at 4 °C. Following incubation, all samples were placed back into the magnetic rack, supernatant discarded, and beads washed three times with 200 μ l RNA wash buffer. Each condition was then divided into four replicates with 10 μ l beads per reaction. All samples were incubated with 170 μ g HeLa S3 nuclear-enriched extract in 200 μ l RNA wash buffer for 3 h on a rotation wheel at 4 °C. After the incubation, samples were washed three times with 200 μ l of RNA wash buffer supplemented with either 50 μ g/ μ l RNase A (Sigma-Aldrich) or 0.02 U/ μ l RiboLock RNase Inhibitor (Thermo Fisher Scientific). One set of C7orf50 pre-incubated beads and the CTRL were treated with RNase A to detect protein-protein interactors (PPIs), while the other set of C7orf50-beads was treated with RiboLock (RDIs) to preserve RNA-dependent interactors. Finally, the bound proteins were eluted by resuspension in 1 \times elution buffer (1 \times LDS [Thermo Fisher Scientific] supplemented with 100 mM DTT [Sigma–Aldrich]) and incubated at 70 °C for 10 min at 1400 rpm using a Thermomixer (Eppendorf).

All samples were further processed for mass spectrometry via SP3 digestion protocol. Briefly, samples were adjusted to 100 μ l with reconstitution buffer (50 mM HEPES-NaOH, 100 mM NaCl, 1 mM EDTA, 0.5% SDC, 1% Triton X-100 [Fisher Scientific], pH 8.0). Proteins were reduced with 10 mM DTT (Sigma–Aldrich) for 30 min at 60 °C and 800 rpm on a Thermomixer (Eppendorf), then alkylated with 25 mM IAA (Sigma–Aldrich) for 25 min at RT and 800 rpm. Paramagnetic beads (1:1 mix of hydrophilic/hydrophobic Carboxylate-Modified Magnetic Particles [GE Healthcare]) were washed twice with LCMS-grade H₂O (VWR). Per sample 2 μ l beads (50 μ g/ μ l) plus 150 μ l 50% LCMS-grade ethanol (Merck) was added and samples incubated for 15 min at RT and 1000 rpm. Supernatants were discarded and beads washed three times with 180 μ l 80% ethanol (Merck) by resuspending twice and incubation for 1 min at RT and 500 rpm. Proteins were digested with 500 ng trypsin (Serva) in 50 mM ABC (Sigma–Aldrich) at 37 °C for 3 h at 1000 rpm. After the digestion, the supernatant was collected, and peptides eluted by adding 100 μ l 0.5% formic acid and incubation for 15 min at RT and 1000 rpm. Afterwards, the supernatant was collected and pooled. Eluted peptides were further concentrated through self-made StageTips and measured on the Q Exactive Plus mass spectrometer (Thermo).

INO80-IP using Protein A beads

To detect proteins interacting with INO80, an INO80-specific antibody (Thermo Fisher Scientific) was coupled to Protein A magnetic Dynabeads (Invitrogen). Briefly, a total of 435 μ l Protein A beads were washed three times with 500 μ l RNA wash buffer, resuspended in 435 μ l buffer and divided into 12 tubes (30 μ l/tube). Eight samples were incubated with 500 μ l RNA wash buffer containing 1 μ g of INO80 antibody, while four samples were incubated without the antibody as the CTRL. All remaining

steps were performed as described above, with the exception that the samples were further processed using the in-gel protocol.

Alphafold3 binding prediction and visualization of C7orf50 to ANRIL

The interaction between C7orf50 and the ANRIL fragments Ex6u7, Ex16u17 or the control RNA fragment pDEST17 were modeled using the web interface of Alphafold3 (147). As an input the C7orf50 AA sequence (NP_001127867.1) was uploaded together with the RNA sequence of Ex6u7 (NR_003529; position: 1130-1388), Ex16u17 (NR_003529; position: 2592-2774) or the 350 nt control RNA sequence of pDEST17 and a Magnesium-Ion (Mg^{2+}). The Predicted Aligned Error (PAE) plot was visualized using the PAE Viewer webserver (222), by uploading the predicted AlphaFold3 crystallographic information file (.cif) model_0.cif as the structure file and the parameters file (full_data_0.json) for the scores. To visualize the binding in 3D, the predicted .cif files were uploaded to the RCSB PDB Mol* 3D Viewer (223). For all predictions the models with the highest confidence ipTM-scores were used. However, it should be noted that all predictions had ipTM-scores below 0.6 indicating a high possibility of inaccuracy (Ex6u7 ipTM = 0.45; Ex16u17 ipTM = 0.22; pDEST17 ipTM = 0.07).

Fluorescence microscopy to detect C7orf50 localization

To detect the cellular localization C7orf50, 8×10^4 HeLa Kyoto cells were seeded into a high 35 mm ibidi μ -Dish dish (Ibidi) and directly transfected with GFP-tagged C7orf50 vector using PEI. Briefly, 1.46 μ g of GFP-C7orf50 were mixed with 3.8 μ l PEI (MW 25.000; Polysciences) in 200 μ l OptiMEM (Thermo Fisher Scientific) and incubated for 20 min at RT. The transfection mix was added dropwise to the cells and incubated for 24 h at 37°C and 5% CO₂ in a humidifier incubator. Cells were fixed using 4% PFA in PBS for 20 min. After washing the cells with 1 ml PBS, fixation was quenched for 5 min with NH₄Cl. Cells were permeabilized with 0.2 % Triton X-100 (Fisher Scientific) in PBS for 15 min. Cells were washed three times with PBS and stained with Hoechst 33342 (1:20.000, Thermo Fisher Scientific) for 10 min. Lastly, cells were washed with PBS and covered with ibidi mounting medium (Ibidi). Images were acquired on via fluorescence microscopy (DMi8, Leica) with a 20x objective lens and further processed via Fiji ImageJ (version 2.14.0/1.54g).

EsiRNA induced knockdown

Targeted endoribonuclease-prepared siRNAs (esiRNAs) were generated as previously described (224,225). For the knockdown of INO80, target regions were adopted from the MISSION esiRNA homepage (Merk). For ANRIL, a region spanning exons 4-6 (100% of isoforms) and a low risk of cross-silencing of other genes was selected (quality score = 0-5) via the Deqor design algorithm (226). An

Material and Methods

esiRNA against Renilla luciferase (RLuc) was used as a control. The selected target regions were amplified using gene-specific primers with generic overhangs using the HF-Polymerase (IMB CF). In a second PCR, amplicons were equipped with T7 promoter sequences at both the 5' and 3' ends. Individual primer sequences can be found in Table 7. These amplicons were further transcribed *in vitro* overnight at 37 °C using 200 units of T7 RNA polymerase (Thermo Fisher Scientific), 1x HH buffer (800 mM Tris/HCl pH 7.9, 0.22 M MgCl₂*6 H₂O [Sigma–Aldrich], 10 mM spermidine [Sigma–Aldrich], 50 mM DTT [Sigma–Aldrich], 1.2 g*ml⁻¹ BSA [New England BioLabs]), 25 mM NTP mix [Jena Bioscience]), in RNase-free H₂O. The resulting single-stranded RNA was annealed to form double-stranded RNA (dsRNA), which was subsequently digested into ~21 bp fragments using RNase III (New England Biolabs). The small dsRNA fragments were purified via a Q Sepharose Fast Flow Kit (Cytiva). The concentration was measured with a Qubit microRNA kit (Thermo Fisher Scientific) on a Qubit 4.0 fluorometer (Thermo Fisher Scientific) following the manufacturer's instructions.

For esiRNA transfections, cells were seeded one day prior to transfection at densities appropriate for the respective plate format (Table 8). For each well, esiRNA and Lipofectamine RNAiMAX (Thermo Fisher Scientific) were separately mixed with OptiMEM (Thermo Fisher Scientific). Depending on the plate format, the amounts of esiRNA and Lipofectamine RNAiMAX were adjusted accordingly and are listed in Table 8. Both solutions were first incubated at RT for 5 min and then combined and incubated for another 20 min at RT. The cell medium was replaced with OptiMEM, and the transfection mixture was added to each well. After 6 h of incubation at 37 °C (5% CO₂, 70% humidity), the transfection medium was replaced with RPMI-media. The knockdown efficiency was determined by RT-qPCR.

Table 8 Specific conditions for esiRNA transfections

Experiment	Plate format	Seeding density	esiRNA conc.	OptiMEM	Lipofectamine RNAiMAX	OptiMEM
RNA-Seq ANRIL knockdown	6 well	2.5*10 ⁵ cells	1 µg	250 µl	9 µl	250 µl
Proteome INO80 knockdown	12 well	1.5*10 ⁵ cells	300 ng	50 µl	3 µl	50 µl
Microscopy / ANRIL / INO80 knockdown CedV infection	24 well	1-1.5*10 ⁵ cells	250 ng	50 µl	3 µl	50 µl

RT-qPCR

A total of 3*10⁶ to 5*10⁶ cells were harvested at the desired timepoint via the RNeasy Mini Kit (Qiagen) according to the manufacturer's instructions. DNA was digested on-column via DNase I (Qiagen). The RNA integrity was validated through agarose gel electrophoresis and microvolume spectrophotometer (NanoPhotometer [Implen]). A total of 0.5 to 1 µg of extracted RNA was reverse transcribed into cDNA using the oligo(dT)18 primer with the First Strand cDNA Synthesis Kit (Thermo Fisher Scientific) following the manufacturer's instructions. RT-qPCR was performed with Power SYBR Green PCR Master Mix (Thermo Fisher Scientific) on a CFX Opus 96 Real-Time PCR System (Bio-Rad), with 40 cycles of 15

Material and Methods

s at 95°C followed by 60 s at 60°C. Primers used for each experiment were ordered at Eurofins Genomics and are listed in Table 7. The mRNA expression level was calculated using the ($2^{-(\Delta\Delta Cq)}$) method (227). 18S rRNA or β -actin was used for normalization as indicated. The samples were measured in technical triplicates. GraphPad Prism 10 (10.2.1) was used for statistical analysis and plotting.

RNA View Fluorescence in situ hybridization (FISH)

Microscopy samples were prepared using the ViewRNA™ ISH Cell Assay Kit (Thermo Fisher Scientific) following the manufacturer's protocol. To visualize ANRIL, the ViewRNA™ target-specific probe set Type 6 (Alexa Fluor 647) against human CDKN2B-AS1 (VA6-3189669) was used. In brief, 1.5×10^5 HeLa Kyoto cells were seeded onto poly-L-lysine (Sigma–Aldrich)-coated 12 mm cover slips (Carl Roth) in a 24-well plate. Cells were treated as indicated in the figure legend. At the desired time-point cells were fixed with 4% paraformaldehyde (PFA) (Carl Roth) and dehydrated with increasing concentrations of ethanol (50–100%). The samples were stored at -20 °C in 100% ethanol. Nuclei were stained with DAPI. Cover slips were mounted onto microscopy slides using ProLong™ Glass Antifade Mountant (Thermo Fisher Scientific) and dried overnight at RT in the dark. Images were acquired on a Leica Stellaris 8 confocal microscope (Leica Microsystems) with a 63x/1.4 oil immersion objective lens and further processed via Fiji ImageJ (version 2.14.0/1.54g).

RNA-Seq (TruSeq) to investigate transcriptome-wide changes after ANRIL knockdown

For RNA-Seq, HeLa Kyoto cells (5.5×10^5) of quadruplicates per treatment, control (esiRLuc) and ANRIL knockdown (esiANRIL), were harvested at 24 and 48 h post-transfection. RNA was extracted using the RNeasy Mini Kit (Qiagen) according to the manufacturer's instructions. The integrity of extracted RNA was checked on a 2100 Bioanalyzer using the RNA 6000 Nano Kit (Agilent). NGS libraries were prepared with Illumina's TruSeq stranded mRNA LP Sample Prep Kit following Illumina's standard protocol (Part # 15031047 Rev. E) but using $\frac{1}{4}$ of the reagents according to the in-house protocol of the Genomics CF (IMB Mainz). 250 ng total RNA was used as starting material and libraries were amplified in 10 PCR cycles. Libraries were profiled using the High Sensitivity DNA Kit on a 2100 Bioanalyzer (Agilent) and quantified using the dsDNA High Sensitivity Kit and Qubit 4.0 Fluorometer (Invitrogen). All samples were pooled together in an equimolar ratio. Sequencing was performed by the Genomics CF at IMB Mainz on an Illumina NextSeq2000. From the pool, 750 pM with 1% PhiX were sequenced on a P2-100 flowcell, PE for 2 x 50 cycles plus 2 x 8 cycles for the dual index read. The data was analyzed using the in-house RNA-Seq pipeline of the Bioinformatics Core Facility. In brief, the general quality of the raw reads was assessed (FastQC, 0.11.9r0), the reads were screened for potential contaminants (FastqScreen, 0.15.3r1), and the adapters were trimmed (cutadapt, 4.4r0). The reads were mapped to

Material and Methods

the GENCODE genome assembly (GRCh38.canonical_assembly.genome.fa) using STAR 2.7.3ar0. Subread (2.0.3r0) was employed for read counting, utilizing GENCODE gencode.v35.annotation.gtf to associate reads with transcript annotations. FPKM calculation was performed via DESeq2 (1.36.0) in R (3.6.0). Additionally, the following tools were used: deepTools (3.5.1r0), MultiQC (1.21r0), Qualimap (2.3r0), rMATS (4.1.2r0), RSeQC (5.0.1r0) and SAMtools (1.17r0).

Viral Infections

HeLa Kyoto cells (80–90% confluence) were infected with recombinant pseudorabies virus (PrV-Kaplan- Δ Ggfp, PrV) (228), influenza A virus (H3N2 A/Victoria/1975, H3N2), herpes simplex virus 1 (HSV1-KOS, HSV) or recombinant cedar virus (rCedV_nTurbo-FP635, CedV) (229). Infections were performed at multiplicities of infection (MOI) of 0.1, 1, or 3, which were determined on the basis of titrations of the respective viral stocks. The cells were incubated for 60 min at 37 °C with 5% CO₂. Following incubation, the inoculum was removed, and the cells were maintained in RPMI-medium. The RNA and protein samples were collected at time points ranging from 0 to 96 hpi, as specified in the individual experiments. Viral supernatants from infected HeLa cells were collected at 24 and 48 hpi and stored at -80 °C until the TCID₅₀ was determined.

RNA sequencing (Quant-seq) for viral infection studies

The sequencing libraries were generated with the QuantSeq 3' mRNA-Seq FWD Kit (Lexogen, #191.96) according to the manufacturer's instructions. In brief, HeLa Kyoto cells of each infection (HSV, PrV, H3N2, CedV and mock CTRL) were harvested in biological quadruplicate at the desired timepoint. The RNA integrity was checked by agarose gel electrophoresis and on a 2100 Bioanalyzer with an RNA 6000 Nano Kit (Agilent). A total of 150 ng of total RNA was used as input, and the libraries were amplified using 15 PCR cycles. Libraries were profiled via the High Sensitivity DNA Kit on a 2100 Bioanalyzer (Agilent) and quantified via the dsDNA High Sensitivity Kit with a Qubit 4.0 Fluorometer (Thermo Fisher Scientific). The samples were pooled in an equimolar ratio. The sequencing was performed by the Genomics Core Facility on an Illumina NextSeq2000. From the pool, 750 pM with 1% PhiX were sequenced on a P2-100 flow cell with 100 cycles plus 2 × 8 cycles for the dual index read. The data was analyzed using the in-house RNA-Seq pipeline of the Bioinformatics Core Facility. In brief, the general quality of the raw reads was assessed (FastQC, 0.11.9r0), the reads were screened for potential contaminants (FastqScreen, 0.15.3r1), and the adapters were trimmed (cutadapt, 4.4r0). The reads were mapped to the GENCODE genome assembly (GRCh38.canonical_assembly.genome.fa) using STAR 2.7.3ar0. Subread (2.0.3r0) was employed for read counting, utilizing GENCODE gencode.v35.annotation.gtf to associate reads with transcript annotations. As 3'-end sequencing was

Material and Methods

performed, the default RPKM calculation was replaced with counts per million (CPM) via DESeq2 (1.36.0) in R (3.6.0). Additionally, the following tools were used: deepTools (3.5.1r0), MultiQC (1.21r0), Qualimap (2.3r0), rMATS (4.1.2r0), RSeQC (5.0.1r0) and SAMtools (1.17r0).

Determination of TCID₅₀

To determine the TCID₅₀ of CedV, 1×10^4 BSRT7/5 cells were seeded into a 96-well plate and incubated overnight. The growth medium was subsequently replaced with 100 μ l of GMEM-medium (Cell Bank, FLI) and 100 μ l of a 10-fold serially diluted virus-containing supernatant. Titrations for each sample were performed in quadruplicate. The cells were incubated for 48 h at 37 °C with 5% CO₂. The plates were then fixed with 4% PFA, and infection was assessed via fluorescence microscopy (DMI8, Leica) on the basis of the fluorescence signal of the recombinant virus. Viral titers were quantified according to the Spearman and Kärber method (230). GraphPad Prism 10 (10.2.1) was used for statistical analysis and plotting.

Bioinformatic analysis

Gene Ontology (GO) enrichment analysis with biological process (BP), cellular compartment (CC), molecular function (MF) terms was performed via the enrichGO function of the ClusterProfiler R package (version 4.6.2) (231) and the annotation from the org.Hs.eg.db R package (version 3.16.0). Reactome analysis was performed using the enrichPathway function of the ReactomePA package (version 1.52.0) (232). To plot enriched GO and Reactome terms, either the dotplot function of the graphics package (version 4.5.0) or the cnetplot function of the enrichplot package (version 1.18.4) was used. A correlation network diagram was generated on the basis of Pearson correlation coefficients (PCCs) calculated from the log₂-fold changes in all enriched proteins across all fragments. The PCC values were computed using the cor function from the R stats package (version 4.2.2) with default parameters. A network diagram was then plotted via the qgraph function from the qgraph R package (version 1.9.8), which included only connections with PCC values greater than 0.4. Julius AI (version 1.0.45) was used to visualize the correlation plots. The unsupervised clustering heatmap was generated with the ComplexHeatmap R package (version 2.14.0). The enriched proteins were clustered into 7 clusters via hierarchical clustering with the hclust function from the R stats package (version 4.2.2), which implements “ward. D2” as the agglomeration method. Heatmaps comparing the viral infections and CedV time kinetic were generated using the ggplot function of the ggplot2 package (version 3.4.2). The data used are based on the log₂-fold change (FC) between the uninfected control and infected samples calculated from the mean CPM values determined via QuantSeq 3' mRNA-Seq V2.

Declaration of Generative AI and AI-assisted technologies in the writing process

During the preparation of this thesis the Large Language Models (LLM) ChatGPT, DeepL and Perplexity were used. ChatGPT and DeepL was used to enhance readability of the text and Perplexity to find research papers. Content assisted by the LLMs were reviewed and edited by the author who takes full responsibility for the content in this thesis. Julius AI was used to prepare the correlation plots shown in Figure 23.

Appendix

Supplementary Table 1 Protein binding profile across ANRIL RNA fragments.....	72
Supplementary Table 2 GOCC enrichment of C7orf50 protein-protein interactors.....	73
Supplementary Table 3 Reactome enrichment of C7orf50 protein-protein interactors.....	74
Supplementary Table 4 GOCC enrichment of C7orf50 RNA-dependent interactors.....	74
Supplementary Table 5 Reactome enrichment of C7orf50 RNA-dependent interactors.....	74
Supplementary Table 6 GOBP ANRIL interactome vs C7orf50 PPIs and RDIs.....	75
Supplementary Table 7 GOBP and GOCC terms for C7orf50 overlap with ANRIL fragments Ex6u7 and Ex16u17	75
Supplementary Table 8 GOBP of ANRIL interacting proteins	76
Supplementary Table 9 Protein distribution across clusters identified by unsupervised clustering.....	76
Supplementary Table 10 GOBP enrichment analysis of biological processes in individual clusters	77
Supplementary Table 11 Reactome downregulated genes 24h ANRIL knockdown.....	77
Supplementary Table 12 GOBP downregulated genes 48h ANRIL knockdown.....	78

Appendix

Supplementary Tables

Supplementary Table 1 Protein binding profile across ANRIL RNA fragments

No. fragments bound	No. proteins	Protein names
1	112	ABT1, ANXA2, ARL6IP4, BAZ1B, BCKDHB, BOP1, BRD3, BTBD1, C1orf131, CASP14, CEBPZ, CWC25, CWF19L2, CYR61, DDX23, DDX28, DDX47, DDX51, DEK, DHX36, EMD, GAPDH, GPATCH8, GTPBP2, HADHA, HADHB, HMGB2, HNRNPA2B1, HNRNPA3, HNRNPAB, HNRNPD, HNRNPH3, HNRNPK, HNRNPM, HNRNPUL1, IGF2BP3, IMP4, INO80, KPNA3, LMNA, LSM8, MDN1, NKAP, NOC3L, NOP14, NOP16, PAPD5, PCBP2, PELP1, PES1, PIP, PIP4K2A, PNISR, POLR2A, PPIB, PPIH, PRDX1, PRPF3, PRPF31, PRPF38A, PRPF4, PRPF6, PTBP1, RAE1, RBM34, RBM42, RBMXL1, RCL1, RPA3, RPL14, RPL15, RPL21, RPL22, RPL23, RPL32, RPL38, RPL7A, RPS13, RPS15A, RPS2, RPS3A, RRP12, RRP36, RRP7A, RRP8, SAFB2, SART1, SDAD1, SENP3-EIF4A1, SMARCC2, SMC1A, SNRPC, SREK1, SREK1IP1, SRRT, SRSF2, SSRP1, STAU1, TEX10, TGM3, TWISTNB, TXN, U2AF1, U2AF2, USP39, WDR12, WDR18, WDR5, YBX1, ZCCHC7, ZNF668, ZNF770
2	86	ALDOA, ANKRD11, ATP5A1, ATP5B, BMS1, C3orf17, C7orf50, CHAF1B, CIRH1A, COL1A2, DCD, DNTTIP2, EIF2AK2, EIF6, EMG1, ENO1, ESF1, EXOSC10, FRG1, GTPBP4, IK, IMP3, ISG20L2, KIAA0020, KPRP, KRT6B, MAK16, MPHOSPH10, MRTO4, NCBP1, NOC2L, NOL10, NOL11, NOL6, NPM3, PABPC1, PABPC4, PINX1, POLR1B, PPAN-P2RY11, RBM10, RBMX, RPA2, RPL10A, RPL11, RPL12, RPL13A, RPL18, RPL18A, RPL28, RPL3, RPL30, RPL35A, RPL39P5, RPL4, RPL5, RPL7, RPL7L1, RPL9, RPLP0, RPLP1, RPS11, RPS14, RPS15, RPS17, RPS19BP1, RPS29, RPS4X, RPS9, RRP15, RRP9, RSL24D1, SF1, SNRPA, SUB1, SUPT16H, TUBB4B, URB2, UTP11L, UTP14A, UTP15, UTP3, WDR46, WDR75, YWHAZ, ZRANB2
3	41	ABCF1, ACTG1, AQR, DCAF13, EIF5B, GNB2L1, HACD3, HEATR1, HIST1H4A, HIST2H3A, HNRNPDL, HNRNPH2, HSP90AB1, HSPB1, JPH1, LUC7L3, NLE1, NOL8, NVL, RAN, RBM22, RPA1, RPL26L1, RPLP2, RPS10, RPS16, RPS18, RPS19, RPS20, RPS21, RPS28, RPS3, RPS5, RPS7, RPSA, SUGP2, URB1, WDR43, WDR89, XPC, ZNF638
4	26	BYSL, C11orf57, DDX1, DDX3X, DDX56, EEF1A1P5, FAM207A, FIBP, GLTSCR2, GRWD1, H2AFV, HIST1H1T, HMGB1, HNRNPL, KHDRBS1, KPNA1, KPNA2, LARP1, MRPL34, PLEC, RAD23B, RPF1, RPS12, RPS27, VIM, ZNF30
5	20	BAG2, CHERP, CRYZ, DHX9, FCF1, PIP4K2B, PKP3, PNO1, POLR2E, SSBP1, TAF15, TECR, UTP20, UTP6, WDR74, WRAP53, XRCC5, XRCC6, ZFR, ZNF346
6	11	AKAP8, EWSR1, HNRNPR, ILF2, KRT18, NMNAT1, PARP1, PRKDC, SERBP1, SYNCRIP, TAF13
7	4	FUS, H2AFY, ILF3, TAOK1
8	7	ADAR, ADARB1, MOV10, PPHLN1, STAU2, STRBP, YLPM1
9	2	RPS26, UPF1
11	1	ELAVL1

Appendix

Supplementary Table 2 GOCC enrichment of C7orf50 protein-protein interactors

ID	Description	GeneRatio	BgRatio	RichFactor	FoldEnrichm	zScore	pvalue	p.adjust	qvalue	geneID	Count
GO:0031982	vesicle	362/1107	407/1381	0,88943489	1,10958409	5,28936193	2,6831E-08	4,0157E-06	3,0536E-06	RPS28/RPS9/	362
GO:0043230	extracellular organelle	291/1107	323/1381	0,90092879	1,12392291	5,11267406	5,0672E-08	4,0157E-06	3,0536E-06	RPS28/RPS9/	291
GO:0065010	extracellular membrane-bounded organelle	291/1107	323/1381	0,90092879	1,12392291	5,11267406	5,0672E-08	4,0157E-06	3,0536E-06	RPS28/RPS9/	291
GO:1903561	extracellular vesicle	291/1107	323/1381	0,90092879	1,12392291	5,11267406	5,0672E-08	4,0157E-06	3,0536E-06	RPS28/RPS9/	291
GO:0070062	extracellular exosome	289/1107	321/1381	0,90031153	1,12315286	5,06036874	6,9413E-08	4,4008E-06	3,3464E-06	RPS28/RPS9/	289
GO:0005576	extracellular region	331/1107	372/1381	0,88978495	1,11002079	4,98814081	1,4048E-07	7,4219E-06	5,6437E-06	RPS28/RPS9/	331
GO:0005840	ribosome	125/1107	131/1381	0,95419847	1,19037768	4,60187421	1,7233E-07	7,8042E-06	5,9344E-06	RPS28/RPS9/	125
GO:0005615	extracellular space	312/1107	350/1381	0,89142857	1,11207123	4,87569937	2,4571E-07	9,7365E-06	7,4038E-06	RPS28/RPS9/	312
GO:0099080	supramolecular complex	198/1107	216/1381	0,91666667	1,14355616	4,61555373	5,1666E-07	1,8198E-05	1,3838E-05	PRC1/RPL28/	198
GO:0012505	endomembrane system	313/1107	354/1381	0,88418079	1,10302951	4,51664684	1,8454E-06	5,8499E-05	4,4484E-05	RPS28/RPL1E	313
GO:0031090	organelle membrane	243/1107	271/1381	0,89667897	1,11862119	4,37646532	2,8486E-06	8,2092E-05	6,2424E-05	RPS28/RPS3/	243
GO:0044391	ribosomal subunit	107/1107	113/1381	0,94690265	1,18127603	4,04071343	5,3622E-06	0,00014165	0,00010771	RPS28/RPS9/	107
GO:0022626	cytosolic ribosome	84/1107	88/1381	0,95454545	1,19081054	3,71691403	2,4407E-05	0,00059336	0,0004512	RPS28/RPS9/	84
GO:0005739	mitochondrion	184/1107	204/1381	0,90196078	1,12521034	3,89228927	2,6205E-05	0,00059336	0,00059336	RPS3/LDHA/I	184
GO:0005759	mitochondrial matrix	97/1107	103/1381	0,94174757	1,17484498	3,70633301	3,3103E-05	0,00069957	0,00053197	RPS3/SDHA/	97
GO:0120025	plasma membrane bounded cell projection	130/1107	142/1381	0,91549296	1,14209194	3,5918321	8,4154E-05	0,00149885	0,00113976	RPL28/RPS3/	130
GO:0099081	supramolecular polymer	105/1107	113/1381	0,92920354	1,15919611	3,54854327	8,5108E-05	0,00149885	0,00113976	PRC1/KRT19/	105
GO:0099512	supramolecular fiber	105/1107	113/1381	0,92920354	1,15919611	3,54854327	8,5108E-05	0,00149885	0,00113976	PRC1/KRT19/	105
GO:0036464	cytoplasmic ribonucleoprotein granule	77/1107	81/1381	0,95061728	1,18591009	3,46506883	9,0903E-05	0,00151665	0,00115329	RPL28/PABP1	77
GO:0099513	polymeric cytoskeletal fiber	82/1107	87/1381	0,94252874	1,17581895	3,40406305	0,00013652	0,00216387	0,00164545	PRC1/KRT19/	82
GO:0030054	cell junction	228/1107	259/1381	0,88030888	1,09819924	3,52289478	0,00016732	0,0024687	0,00184772	RPS28/RPS9/	228
GO:0042995	cell projection	137/1107	151/1381	0,90728477	1,13185209	3,44953862	0,00017133	0,0024687	0,00187724	RPL28/RPS3/	137
GO:0031410	cytoplasmic vesicle	163/1107	182/1381	0,89560044	1,11728064	3,41185455	0,00022525	0,00297524	0,00226243	HUWE1/HSP1	163
GO:0097708	intracellular vesicle	163/1107	182/1381	0,89560044	1,11728064	3,41185455	0,00022525	0,00297524	0,00226243	HUWE1/HSP1	163
GO:0015935	small ribosomal subunit	56/1107	58/1381	0,96551724	1,20449802	3,19713709	0,0002537	0,00321694	0,0024622	RPS28/RPS3/	56
GO:0010494	cytoplasmic stress granule	47/1107	48/1381	0,97916667	1,2215259	3,13883233	0,0002673	0,00325906	0,00247825	PABP1/G3B	47
GO:0098588	bounding membrane of organelle	103/1107	112/1381	0,91964286	1,147269	3,26683814	0,0003241	0,00380514	0,0028935	RPS28/RPS2E	103
GO:0031967	organelle envelope	150/1107	168/1381	0,89285714	1,1138534	3,16379488	0,0006103	0,00690943	0,00525405	RPS3/LDHB/	150
GO:0019866	organelle inner membrane	78/1107	84/1381	0,92857143	1,15840754	3,01011832	0,00085006	0,00929205	0,00706585	RPS3/LDHB/	78
GO:0005773	vacuole	57/1107	60/1381	0,95	1,18514002	2,94620248	0,00092097	0,00952613	0,00724385	SLC7A5/ZC3A	57
GO:0030055	cell-substrate junction	102/1107	112/1381	0,91071429	1,13613047	3,01975432	0,00093158	0,00952613	0,00724385	RPS9/RPS16/	102
GO:0005740	mitochondrial envelope	82/1107	89/1381	0,92134831	1,14939659	2,92780735	0,00123271	0,01194388	0,00908235	RPS3/LDHB/	82
GO:0005925	focal adhesion	100/1107	110/1381	0,90909091	1,13410528	2,9458289	0,00124337	0,01194388	0,00908235	RPS9/RPS16/	100
GO:0031966	mitochondrial membrane	81/1107	88/1381	0,92045455	1,1482816	2,88846693	0,00143887	0,01303201	0,00990978	RPS3/LDHB/	81
GO:0035770	ribonucleoprotein granule	81/1107	88/1381	0,92045455	1,1482816	2,88846693	0,00143887	0,01303201	0,00990978	RPL28/PABP1	81
GO:0000323	lytic vacuole	53/1107	56/1381	0,94642857	1,1806846	2,77360937	0,00189609	0,01624489	0,01235292	SLC7A5/ZC3A	53
GO:0005764	lysosome	53/1107	56/1381	0,94642857	1,1806846	2,77360937	0,00189609	0,01624489	0,01235292	SLC7A5/ZC3A	53
GO:0045202	synapse	142/1107	161/1381	0,88198758	1,10029345	2,72046817	0,00310964	0,02511894	0,01910091	RPS28/RPS9/	142
GO:0015629	actin cytoskeleton	57/1107	61/1381	0,93442623	1,16571149	2,65992049	0,00311461	0,02511894	0,01910091	MYH9/MYL6/	57
GO:0022627	cytosolic small ribosomal subunit	35/1107	36/1381	0,97222222	1,21286259	2,60032437	0,00316958	0,02511894	0,01910091	RPS28/RPS9/	35
GO:0005783	endoplasmic reticulum	141/1107	160/1381	0,88125	1,09937331	2,68602451	0,00348989	0,02654381	0,0201844	RPS28/RPL1E	141
GO:0005743	mitochondrial inner membrane	69/1107	75/1381	0,92	1,14771454	2,64314125	0,00351685	0,02654381	0,0201844	RPS3/LDHB/	69
GO:0005874	microtubule	56/1107	60/1381	0,93333333	1,16434809	2,6153327	0,00367815	0,02701831	0,02054522	PRC1/CTC3/	56
GO:0070161	anchoring junction	130/1107	147/1381	0,88435374	1,10324527	2,66078226	0,00375018	0,02701831	0,02054522	RPS9/RPS16/	130
GO:0030424	axon	55/1107	59/1381	0,93220339	1,16293847	2,57022991	0,00433861	0,03056311	0,02324075	HSP90A1/P	55
GO:0031984	organelle subcompartment	85/1107	94/1381	0,90425532	1,12807281	2,58445901	0,00453329	0,03124025	0,02375566	RPS28/RPS2E	85
GO:0005929	cilium	33/1107	34/1381	0,97058824	1,21082417	2,5010025	0,0047377	0,03195429	0,02429863	HSP90AA1/C	33
GO:0140535	intracellular protein-containing complex	122/1107	138/1381	0,88405797	1,10287629	2,55951314	0,00519286	0,03429453	0,02607819	CCT3/HSP90	122
GO:0005794	Golgi apparatus	72/1107	79/1381	0,91139241	1,13697643	2,51937014	0,00551312	0,03566653	0,02712148	HUWE1/TCF/	72
GO:0042175	nuclear outer membrane-endoplasmic reticulum membrane network	76/1107	84/1381	0,9047619	1,12870478	2,44569559	0,00711233	0,04509217	0,03428892	RPS28/RPS2E	76
GO:0030027	lamellipodium	22/1107	22/1381	1	1,24751581	2,35148724	0,00739254	0,0459497	0,03494099	PABP1/CTT	22
GO:0015934	large ribosomal subunit	51/1107	55/1381	0,92727273	1,15678739	2,38428834	0,00829717	0,04956844	0,03769276	RPL35A/RPL1	51
GO:0005774	vacuolar membrane	30/1107	31/1381	0,96774194	1,20727336	2,34528448	0,0086002	0,04956844	0,03769276	SLC7A5/CLTC	30
GO:0042470	melanosome	30/1107	31/1381	0,96774194	1,20727336	2,34528448	0,0086002	0,04956844	0,03769276	HSP90A1/C	30
GO:0048770	pigment granule	30/1107	31/1381	0,96774194	1,20727336	2,34528448	0,0086002	0,04956844	0,03769276	HSP90A1/C	30

Appendix

Supplementary Table 3 Reactome enrichment of C7orf50 protein-protein interactors

ID	Description	GeneRatio	BgRatio	RichFactor	FoldEnrichm	zScore	pvalue	p.adjust	qvalue	geneID	Count
R-HSA-14307	Metabolism	241/901	256/1076	0.94140625	1.1242543	5.16502097	1.7992E-08	6.2547E-06	4.8755E-06	RPS28/RPS9	241
R-HSA-89538	Cellular responses to stimuli	216/901	228/1076	0.94736842	1.1313745	5.06790149	2.3692E-08	6.2547E-06	4.8755E-06	RPS28/RPS9	216
R-HSA-71291	Metabolism of amino acids and derivatives	117/901	119/1076	0.98319328	1.17415757	4.56885589	6.3447E-08	9.2812E-06	7.2347E-06	RPS28/RPS9	117
R-HSA-72766	Translation	158/901	164/1076	0.96341463	1.15053734	4.74915513	7.0312E-08	9.2812E-06	7.2347E-06	RPS28/RPS9	158
R-HSA-39249	Metabolism of proteins	337/901	368/1076	0.91576087	1.09362785	5.0218062	1.2814E-07	1.3532E-05	1.0478E-05	RPS28/RPS9	337
R-HSA-22627	Cellular responses to stress	199/901	211/1076	0.94312796	1.12631042	4.64108959	3.4017E-07	2.9935E-05	2.3344E-05	RPS28/RPS9	199
R-HSA-16827	Influenza Viral RNA Transcription and Replication	96/901	98/1076	0.97959184	1.16985662	4.00012623	2.735E-06	0.0002063	0.00016081	RPS28/RPS9	96
R-HSA-24085	Selenoamino acid metabolism	87/901	89/1076	0.97752809	1.16739204	3.73954551	1.3007E-05	0.00085845	0.00066917	RPS28/RPS9	87
R-HSA-96751	Nervous system development	136/901	144/1076	0.94444444	1.1278826	3.73966198	3.3648E-05	0.00154203	0.00120202	RPS28/RPS9	136
R-HSA-97110	Cellular response to starvation	81/901	83/1076	0.97590361	1.16545204	3.55864081	3.6067E-05	0.00154203	0.00120202	RPS28/RPS9	81
R-HSA-72613	Eukaryotic Translation Initiation	90/901	93/1076	0.96774194	1.15570513	3.56299523	4.4737E-05	0.00154203	0.00120202	RPS28/RPS9	90
R-HSA-72737	Cap-dependent Translation Initiation	90/901	93/1076	0.96774194	1.15570513	3.56299523	4.4737E-05	0.00154203	0.00120202	RPS28/RPS9	90
R-HSA-42247	Axon guidance	134/901	142/1076	0.94366197	1.12694815	3.68251656	4.4749E-05	0.00154203	0.00120202	RPS28/RPS9	134
R-HSA-37617	Signaling by ROBO receptors	99/901	103/1076	0.96116505	1.14785082	3.57876799	4.9059E-05	0.00154203	0.00120202	RPS28/RPS9	99
R-HSA-15684	Eukaryotic Translation Elongation	79/901	81/1076	0.97530864	1.16474151	3.49688709	5.0483E-05	0.00154203	0.00120202	RPS28/RPS9	79
R-HSA-96330	Response of EIF2AK4 (GCN2) to amino acid deficiency	79/901	81/1076	0.97530864	1.16474151	3.49688709	5.0483E-05	0.00154203	0.00120202	RPS28/RPS9	79
R-HSA-15682	L13a-mediated translational silencing of Ceruloplasmin expression	89/901	92/1076	0.9673913	1.1552864	3.53246104	5.2569E-05	0.00154203	0.00120202	RPS28/RPS9	89
R-HSA-72706	GTP hydrolysis and joining of the 60S ribosomal subunit	89/901	92/1076	0.9673913	1.1552864	3.53246104	5.2569E-05	0.00154203	0.00120202	RPS28/RPS9	89
R-HSA-90105	Regulation of expression of SLTs and ROBOs	97/901	101/1076	0.96039604	1.14693245	3.51822578	6.6949E-05	0.00186049	0.00145026	RPS28/RPS9	97
R-HSA-16825	Influenza Infection	105/901	110/1076	0.96039604	1.14693245	3.51822578	6.6949E-05	0.00206031	0.00160660	RPS28/RPS9	105
R-HSA-15690	Peptide chain elongation	76/901	78/1076	0.97435897	1.16360739	3.4027696	8.3298E-05	0.00209435	0.00163256	RPS28/RPS9	76
R-HSA-19282	Viral mRNA Translation	75/901	77/1076	0.97402597	1.16320971	3.37098029	9.8333E-05	0.00216333	0.00168633	RPS28/RPS9	75
R-HSA-24085	Selenocysteine synthesis	75/901	77/1076	0.97402597	1.16320971	3.37098029	9.8333E-05	0.00216333	0.00168633	RPS28/RPS9	75
R-HSA-12764	Eukaryotic Translation Termination	75/901	77/1076	0.97402597	1.16320971	3.37098029	9.8333E-05	0.00216333	0.00168633	RPS28/RPS9	75
R-HSA-17993	SRP-dependent cotranslational protein targeting to membrane	83/901	86/1076	0.96511628	1.1525695	3.34539146	0.00013682	0.0028896	0.00225246	RPS28/RPS9	83
R-HSA-72685	Formation of a pool of free 40S subunits	82/901	85/1076	0.96470588	1.15207939	3.31352764	0.00016015	0.00325229	0.0025517	RPS28/RPS9	82
R-HSA-97595	Nonsense Mediated Decay (NMD) independent of the Exon Junction Complex (EJC)	79/901	82/1076	0.96341463	1.15053734	3.21666316	0.00025595	0.0047971	0.00373937	RPS28/RPS9	79
R-HSA-92780	Nonsense-Mediated Decay (NMD)	88/901	92/1076	0.95652174	1.14230565	3.23717452	0.00026348	0.0047971	0.00373937	RPS28/RPS9	88
R-HSA-97595	Nonsense Mediated Decay (NMD) enhanced by the Exon Junction Complex (EJC)	88/901	92/1076	0.95652174	1.14230565	3.23717452	0.00026348	0.0047971	0.00373937	RPS28/RPS9	88
R-HSA-12667	Developmental Biology	203/901	223/1076	0.91031209	1.08712293	3.31404179	0.00036526	0.00642865	0.00501116	RPS28/RPS9	203
R-HSA-11694	Antiviral mechanism by IFN-stimulated genes	52/901	53/1076	0.98113208	1.17169602	2.90742116	0.00075642	0.01288354	0.01004279	TUBA1C/OA5	52
R-HSA-69620	Cell Cycle Checkpoints	61/901	63/1076	0.96825397	1.15631661	2.90013555	0.00094861	0.01565201	0.01220083	H2BC21/SFN	61
R-HSA-16825	Immune System	193/901	213/1076	0.90610329	1.08209449	3.03421269	0.0010723	0.01715688	0.01337388	HUWE1/TUB	193
R-HSA-56536	Vesicle-mediated transport	76/901	80/1076	0.95	1.1345172	2.83622549	0.00150924	0.02232024	0.01739875	TUBA1C/SFN	76
R-HSA-191353	Interferon Signaling	58/901	60/1076	0.96666667	1.15442101	2.79179017	0.00151865	0.02232024	0.01739875	TUBA1C/OA5	58
R-HSA-12802	Cytokine Signaling in Immune system	100/901	107/1076	0.93457944	1.11610153	2.87022233	0.00152183	0.02232024	0.01739875	TUBA1C/TCP	100
R-HSA-565191	Disorders of transmembrane transporters	33/901	33/1076	1	1.19422863	2.57025183	0.00259288	0.0361173	0.02815364	NUP33	33
R-HSA-19999	Membrane Trafficking	72/901	76/1076	0.94736842	1.1313745	2.69442105	0.00263859	0.0361173	0.02815364	TUBA1C/SFN	72
R-HSA-16436	Disease	298/901	337/1076	0.884273	1.05602413	2.81459225	0.00266776	0.0361173	0.02815364	RPS28/RPS9	298
R-HSA-45053	Regulation of mRNA stability by proteins that bind AU-rich elements	32/901	32/1076	1	1.19422863	2.52979658	0.00311504	0.0411854	0.03205213	PABPC1/EIF4	32
R-HSA-69002	DNA Replication Pre-Initiation	31/901	31/1076	1	1.19422863	2.48876312	0.00374163	0.04818489	0.03756039	H2BC21/PSM	31

Supplementary Table 4 GOCC enrichment of C7orf50 RNA-dependent interactors

ID	Description	GeneRatio	BgRatio	RichFactor	FoldEnrichm	zScore	pvalue	p.adjust	qvalue	geneID	Count
GO:1990904	ribonucleoprotein complex	24/40	344/1381	0.06976744	2.40872093	5.20559001	1.8008E-06	0.00027913	0.0002578	NOP10/YBX1	24
GO:0005697	telomerase holoenzyme complex	4/40	11/1381	0.36363636	12.5545455	6.64269136	0.0001724	0.01336103	0.01234024	NOP10/HNR	4

Supplementary Table 5 Reactome enrichment of C7orf50 RNA-dependent interactors

ID	Description	GeneRatio	BgRatio	RichFactor	FoldEnrichm	zScore	pvalue	p.adjust	qvalue	geneID	Count
R-HSA-88687	rRNA processing in the nucleus and cytosol	12/22	127/1076	0.09448819	4.62133142	6.27526824	1.0271E-06	9.4388E-05	7.4839E-05	NOP10/KRR1	12
R-HSA-72312	rRNA processing	12/22	129/1076	0.09302326	4.54968288	6.20589878	1.2258E-06	9.4388E-05	7.4839E-05	NOP10/KRR1	12
R-HSA-89538	Metabolism of RNA	16/22	360/1076	0.04444444	2.17373737	3.9424023	0.00016553	0.00849729	0.00673743	NOP10/YBX1	16
R-HSA-67912	Major pathway of rRNA processing in the nucleolus and cytosol	5/22	121/1076	0.07438017	3.63786627	4.4477364	0.00030092	0.0115855	0.00918604	KRR1/DXD21	9
R-HSA-97595	Nonsense Mediated Decay (NMD) independent of the Exon Junction Complex (EJC)	7/22	82/1076	0.08536585	4.1751663	4.31991774	0.00077301	0.02380858	0.01887761	RPS10/PABP	7
R-HSA-15682	L13a-mediated translational silencing of Ceruloplasmin expression	7/22	92/1076	0.07608696	3.72134387	3.94162274	0.00156448	0.02571701	0.0203908	RPS10/PABP	7
R-HSA-92780	Nonsense-Mediated Decay (NMD)	7/22	92/1076	0.07608696	3.72134387	3.94162274	0.00156448	0.02571701	0.0203908	RPS10/PABP	7
R-HSA-97595	Nonsense Mediated Decay (NMD) enhanced by the Exon Junction Complex (EJC)	7/22	92/1076	0.07608696	3.72134387	3.94162274	0.00156448	0.02571701	0.0203908	RPS10/PABP	7
R-HSA-72613	Eukaryotic Translation Initiation	7/22	93/1076	0.07526882	3.68132942	3.90670084	0.00166994	0.02571701	0.0203908	RPS10/PABP	7
R-HSA-72737	Cap-dependent Translation Initiation	7/22	93/1076	0.07526882	3.68132942	3.90670084	0.00166994	0.02571701	0.0203908	RPS10/PABP	7
R-HSA-67909	rRNA modification in the nucleus and cytosol	4/22	29/1076	0.13793103	6.7460815	4.52994268	0.00229204	0.03120659	0.02474343	NOP10/KRR1	4
R-HSA-90105	Regulation of expression of SLTs and ROBOs	7/22	101/1076	0.06930693	3.38973897	3.643377	0.00273116	0.0315096	0.02498369	RPS10/PABP	7
R-HSA-37617	Signaling by ROBO receptors	7/22	103/1076	0.06796117	3.3239188	3.58161095	0.00306491	0.0315096	0.02498369	RPS10/PABP	7
R-HSA-19282	Viral mRNA Translation	6/22	77/1076	0.07792208	3.81109799	3.69686738	0.00327372	0.0315096	0.02498369	RPS10/RPL31	6
R-HSA-24085	Selenocysteine synthesis	6/22	77/1076	0.07792208	3.81109799	3.69686738	0.00327372	0.0315096	0.02498369	RPS10/RPL31	6
R-HSA-72764	Eukaryotic Translation Termination	6/22	77/1076	0.07792208	3.81109799	3.69686738	0.00327372	0.0315096	0.02498369	RPS10/RPL31	6
R-HSA-15690	Peptide chain elongation	6/22	78/1076	0.07692308	3.76223776	3.65795498	0.0034994	0.0317004	0.02513498	RPS10/RPL31	6
R-HSA-15684	Eukaryotic Translation Elongation	6/22	81/1076	0.07407407	3.62289562	3.54492658	0.00424746	0.03366417	0.02669202	RPS10/RPL31	6
R-HSA-96330	Response of EIF2AK4 (GCN2) to amino acid deficiency	6/22	81/1076	0.07407407	3.62289562	3.54492658	0.00424746	0.03366417	0.02669202	RPS10/RPL31	6
R-HSA-16825	Influenza Infection	7/22	110/1076	0.06363636	3.11239669	3.37659152	0.00449029	0.03366417	0.02669202	RPS10/RPL31	7
R-HSA-42247	Axon guidance	8/22	142/1076	0.05633803	2.75544174	3.24229422	0.00476717	0.03366417	0.02669202	RPS10/PABP	8
R-HSA-97110	Cellular response to starvation	6/22	83/1076	0.07228916	3.53559693	3.47248123	0.00480917	0.03366417	0.02669202	RPS10/RPL31	6
R-HSA-96751	Nervous system development	8/22	144/1076	0.05555556	2.71717172	3.19729187	0.00521099	0.03480951	0.02760016	RPS10/PABP	8
R-HSA-72685	Formation of a pool of free 40S subunits	6/22	85/1076	0.07058824	3.45240642	3.40220397	0.00542486	0.03480951	0.02760016	RPS10/RPL31	6
R-HSA-17993	SRP-dependent cotranslational protein targeting to membrane	6/22	86/1076	0.06976744	3.41226216	3.3678396	0.00575392	0.03544416	0.02810337	RPS10/RPL31	6
R-HSA-24085	Selenoamino acid metabolism	6/22	89/1076	0.06741573	3.29724208	3.26767201	0.00683068	0.04045865	0.03207931	RPS10/RPL31	6
R-HSA-18078	Extension of Telomeres	3/22	21/1076	0.14285714	6.98701299	4.00118733	0.00777942	0.04427543	0.0351056	NOP10/DKC1	3
R-HSA-72706	GTP hydrolysis and joining of the 60S ribosomal subunit	6/22	92/1076	0.06521739	3.18972332	3.17161801	0.00805008	0.04427543	0.0351056	RPS10/RPL31	6

Appendix

Supplementary Table 6 GOBP ANRIL interactome vs C7orf50 PPIs and RDIs

GOBP: ANRIL Interactome overlap PPIs + RDIs											
ID	Description	GeneRatio	BgRatio	RichFacto	FoldEnrich	zScore	pvalue	p.adjust	qvalue	geneID	Count
GO:0002181	cytoplasmic translation	7/12	95/1009	0.073684	6.195614	5.834436	2.84E-05	0.006157	0.005794	RPS10/PAI	7
GO:0061157	mRNA destabilization	3/12	16/1009	0.1875	15.76563	6.528456	0.000661	0.043259	0.040709	PABPC1/YI	3
GO:0050779	RNA destabilization	3/12	17/1009	0.176471	14.83824	6.309902	0.000797	0.043259	0.040709	PABPC1/YI	3
GO:0061014	positive regulation of mRNA catabolic process	3/12	17/1009	0.176471	14.83824	6.309902	0.000797	0.043259	0.040709	PABPC1/YI	3
GOBP: ANRIL Interactome overlap PPIs											
ID	Description	GeneRatio	BgRatio	RichFacto	FoldEnrich	zScore	pvalue	p.adjust	qvalue	geneID	Count
GO:0002181	cytoplasmic translation	41/157	95/1009	0.431579	2.773651	7.793223	7.37E-12	8.07E-09	8.07E-09	RPL28/NCI	41
GO:0042254	ribosome biogenesis	40/157	128/1009	0.3125	2.00836	5.23833	1.15E-06	0.000629	0.000629	BOP1/DDX	40
GO:0042255	ribosome assembly	13/157	25/1009	0.52	3.341911	5.087485	1.87E-05	0.005425	0.005425	BOP1/RPS	13
GO:0006412	translation	51/157	198/1009	0.257576	1.655375	4.413393	2.02E-05	0.005425	0.005425	RPL28/NCI	51
GO:0042273	ribosomal large subunit biogenesis	16/157	36/1009	0.444444	2.856334	4.866439	2.48E-05	0.005425	0.005425	BOP1/PES	16
GO:0022613	ribonucleoprotein complex biogenesis	49/157	192/1009	0.255208	1.640161	4.229498	4.24E-05	0.007732	0.007732	BOP1/DDX	49
GOBP: ANRIL Interactome overlap RDIs											
no enrichment found											

Supplementary Table 7 GOBP and GOCC terms for C7orf50 overlap with ANRIL fragments Ex6u7 and Ex16u17

GOBP: PPIs C7orf50 vs both ANRIL fragments Ex6u7 & Ex16u17											
ID	Description	GeneRatio	BgRatio	RichFacto	FoldEnrich	zScore	pvalue	p.adjust	qvalue	geneID	Count
GO:0002181	cytoplasmic translation	30/73	95/1009	0.315789	4.364816	9.618422	2.24E-14	2.07E-11	2.07E-11	RPL28/RP	30
GO:0006412	translation	37/73	198/1009	0.186869	2.582884	6.934656	5.12E-10	2.36E-07	2.36E-07	RPL28/RP	37
GO:0042255	ribosome assembly	10/73	25/1009	0.4	5.528767	6.400387	2.9E-06	0.000893	0.000893	RPS28/PRI	10
GO:0042254	ribosome biogenesis	23/73	128/1009	0.179688	2.483626	5.014125	8.8E-06	0.002032	0.002032	RPS28/RP	23
GO:0042274	ribosomal small subunit biogenesis	12/73	45/1009	0.266667	3.685845	5.145202	3.51E-05	0.00648	0.00648	RPS28/RP	12
GOCC: PPIs C7orf50 vs both ANRIL fragments Ex6u7											
ID	Description	GeneRatio	BgRatio	RichFacto	FoldEnrich	zScore	pvalue	p.adjust	qvalue	geneID	Count
GO:0046540	U4/U6 x U5 tri-snRNP complex	4/26	16/1027	0.25	9.875	5.76363	0.000479	0.033319	0.031792	PRPF31/PI	4
GO:0097526	spliceosomal tri-snRNP complex	4/26	16/1027	0.25	9.875	5.76363	0.000479	0.033319	0.031792	PRPF31/PI	4
GOCC: PPIs C7orf50 vs both ANRIL fragments Ex16u17											
ID	Description	GeneRatio	BgRatio	RichFacto	FoldEnrich	zScore	pvalue	p.adjust	qvalue	geneID	Count
GO:0022626	cytosolic ribosome	12/26	78/1027	0.153846	6.076923	7.513773	6.52E-08	6.65E-06	5.91E-06	RPL14/RP	12
GO:0044391	ribosomal subunit	12/26	99/1027	0.121212	4.787879	6.386795	1.04E-06	5.31E-05	4.72E-05	RPL14/RP	12
GO:0005840	ribosome	12/26	114/1027	0.105263	4.157895	5.760471	5.05E-06	0.000172	0.000152	RPL14/RP	12
GO:0022625	cytosolic large ribosomal subunit	7/26	42/1027	0.166667	6.583333	5.951732	4.24E-05	0.00108	0.000959	RPL14/RPI	7
GO:0015934	large ribosomal subunit	7/26	50/1027	0.14	5.53	5.290287	0.000137	0.002687	0.002385	RPL14/RPI	7
GO:0005925	focal adhesion	9/26	89/1027	0.101124	3.994382	4.761503	0.000169	0.002687	0.002385	RPS3A/RP	9
GO:0030055	cell-substrate junction	9/26	90/1027	0.1	3.95	4.719726	0.000184	0.002687	0.002385	RPS3A/RP	9
GO:0030054	cell junction	13/26	197/1027	0.06599	2.606599	4.040591	0.000325	0.004145	0.003679	RPL14/RP	13
GO:0022627	cytosolic small ribosomal subunit	5/26	30/1027	0.166667	6.583333	4.999769	0.000645	0.007305	0.006483	RPS3A/RP	5
GO:0070161	anchoring junction	9/26	117/1027	0.076923	3.038462	3.773272	0.001392	0.014195	0.012598	RPS3A/RP	9
GOBP: RDIs C7orf50 vs both ANRIL fragments Ex6u7 & Ex16u17											
no enrichment found											
GOCC: RDIs C7orf50 vs both ANRIL fragments Ex6u7 & Ex16u17											
ID	Description	GeneRatio	BgRatio	RichFacto	FoldEnrich	zScore	pvalue	p.adjust	qvalue	geneID	Count
GO:0022626	cytosolic ribosome	5/9	78/1027	0.064103	7.314815	5.452502	0.000221	0.0043	0.00265	RPS10/RPI	5
GO:0022625	cytosolic large ribosomal subunit	4/9	42/1027	0.095238	10.86772	6.136837	0.000263	0.0043	0.00265	RPLP0/RPI	4
GO:0005925	focal adhesion	5/9	89/1027	0.05618	6.410737	5.019622	0.000418	0.0043	0.00265	RPS10/RPI	5
GO:0030055	cell-substrate junction	5/9	90/1027	0.055556	6.339506	4.983949	0.000441	0.0043	0.00265	RPS10/RPI	5
GO:0015934	large ribosomal subunit	4/9	50/1027	0.08	9.128889	5.538472	0.000524	0.0043	0.00265	RPLP0/RPI	4
GO:0044391	ribosomal subunit	5/9	99/1027	0.050505	5.763187	4.685569	0.000695	0.004751	0.002928	RPS10/RPI	5
GO:0005840	ribosome	5/9	114/1027	0.04386	5.004873	4.262132	0.001354	0.007834	0.004827	RPS10/RPI	5
GO:0070161	anchoring junction	5/9	117/1027	0.042735	4.876543	4.186373	0.001528	0.007834	0.004827	RPS10/RPI	5
GO:0014069	postsynaptic density	3/9	32/1027	0.09375	10.69792	5.237969	0.002035	0.008307	0.005119	RPLP0/RPI	3
GO:0099572	postsynaptic specialization	3/9	32/1027	0.09375	10.69792	5.237969	0.002035	0.008307	0.005119	RPLP0/RPI	3
GO:0032279	asymmetric synapse	3/9	33/1027	0.090909	10.37374	5.14396	0.002229	0.008307	0.005119	RPLP0/RPI	3
GO:0098984	neuron to neuron synapse	3/9	34/1027	0.088235	10.06863	5.053909	0.002434	0.008315	0.005123	RPLP0/RPI	3
GO:0098794	postsynapse	3/9	57/1027	0.052632	6.005848	3.654688	0.010731	0.033845	0.020854	RPLP0/RPI	3
GO:0005615	extracellular space	6/9	275/1027	0.021818	2.489697	2.713166	0.013865	0.040604	0.025019	CHLSN/MC	6
GO:0030054	cell junction	5/9	197/1027	0.025381	2.896221	2.782301	0.015971	0.041944	0.025845	RPS10/RPI	5
GO:1990904	ribonucleoprotein complex	6/9	284/1027	0.021127	2.410798	2.626943	0.016368	0.041944	0.025845	RPS10/MR	6
GO:0005576	extracellular region	6/9	292/1027	0.020548	2.344749	2.55276	0.018869	0.045508	0.028041	CHLSN/MC	6
GOBP/GOCC: RDIs C7orf50 vs both ANRIL fragments Ex6u7											
no enrichment found											
GOBP/GOCC: RDIs C7orf50 vs both ANRIL fragments Ex16u17											
no enrichment found											

Appendix

Supplementary Table 8 GOBP of ANRIL interacting proteins

ID	Description	GeneRatio	BgRatio	pvalue	p.adjust	qvalue	geneID	Count
GO:0042254	ribosome biogenesis	90/295	310/18903	4,45E-91	1,12E-87	9,72E-88	WDR74/NOP53/	90
GO:0006364	rRNA processing	72/295	229/18903	5,41E-75	4,52E-72	3,93E-72	WDR74/NOP53/	72
GO:0002181	cytoplasmic translation	58/295	161/18903	3,94E-64	1,97E-61	1,72E-61	RPS26/HNRNPD	58
GO:0008380	RNA splicing	55/295	469/18903	2,65E-32	7,39E-30	6,43E-30	RPS26/HNRNPK	55
GO:0022618	ribonucleoprotein complex assembly	36/295	234/18903	2,15E-25	4,15E-23	3,61E-23	LUC7L3/NOP53/	36
GO:1903311	regulation of mRNA metabolic process	35/295	309/18903	3,29E-20	4,59E-18	3,99E-18	ELAVL1/HNRNPI	35
GO:0006402	mRNA catabolic process	26/295	248/18903	1,84E-14	2E-12	1,74E-12	ELAVL1/MOV10,	26
GO:0000723	telomere maintenance	19/295	154/18903	3,75E-12	2,94E-10	2,55E-10	HNRNPD/PARP1	19
GO:0000469	cleavage involved in rRNA processing	10/295	28/18903	7,54E-12	5,4E-10	4,7E-10	NOP14/UTP20/F	10
GO:0048524	positive regulation of viral process	11/295	64/18903	3,96E-09	1,91E-07	1,66E-07	HMGB1/HACD3/	11
GO:1902570	protein localization to nucleolus	7/295	18/18903	5,77E-09	2,73E-07	2,37E-07	NOP53/PINX1/R	7
GO:0006913	nucleocytoplasmic transport	22/295	329/18903	1,15E-08	4,98E-07	4,34E-07	ELAVL1/KPNA2/	22
GO:1904667	negative regulation of ubiquitin protein ligase activity	6/295	12/18903	1,17E-08	4,98E-07	4,34E-07	RPL11/RPS20/Rf	6
GO:0006356	regulation of transcription by RNA polymerase I	9/295	43/18903	1,72E-08	6,96E-07	6,06E-07	NOP53/DEK/MA	9
GO:0031397	negative regulation of protein ubiquitination	10/295	84/18903	7,34E-07	2,11E-05	1,84E-05	U2AF2/PINX1/R	10
GO:0006338	chromatin remodeling	20/295	373/18903	1,82E-06	4,97E-05	4,32E-05	HMGB1/CHAF1B	20
GO:0033750	ribosome localization	5/295	15/18903	2,36E-06	6,24E-05	5,43E-05	RAN/EIF6/MDN1	5
GO:0051054	positive regulation of DNA metabolic process	17/295	301/18903	5,54E-06	0,000136	0,000118	HMGB1/HNRNPD	17
GO:1901796	regulation of signal transduction by p53 class mediator	9/295	105/18903	3,94E-05	0,000837	0,000729	HNRNPK/NOP53/	9
GO:0006302	double-strand break repair	15/295	300/18903	7,98E-05	0,001575	0,001371	HMGB1/PARP1/	15
GO:0009615	response to virus	17/295	409/18903	0,000254	0,004251	0,003698	PCBP2/MOV10/	17
GO:0001825	blastocyst formation	5/295	45/18903	0,000656	0,010025	0,008722	WDR74/BYSL/Rf	5
GO:0098760	response to interleukin-7	3/295	14/18903	0,001205	0,01757	0,015286	YBX1/RAD23B/A	3
GO:0031647	regulation of protein stability	13/295	325/18903	0,001874	0,025678	0,022339	POLR2E/NOP53/	13
GO:0034644	cellular response to UV	6/295	89/18903	0,0027	0,034364	0,029897	PARP1/NEDD4/	6
GO:0032481	positive regulation of type I interferon production	5/295	63/18903	0,003005	0,037475	0,032603	GAPDH/DDX3X/	5
GO:0043631	RNA polyadenylation	4/295	41/18903	0,003737	0,045042	0,039186	ZCCHC7/PABPC1	4
GO:0071731	response to nitric oxide	3/295	21/18903	0,004063	0,048046	0,041799	HNRNPD/ATP5F	3

Supplementary Table 9 Protein distribution across clusters identified by unsupervised clustering

Cluster	No. proteins	Protein names
1	25	IMP4, BMS1, RRP15, CIRH1A, EMG1, BYSL, HEATR1, UTP14A, UTP15, MRTO4, RPS2, UTP11L, DCAF13, UTP6, NOL6, RPL30, RRP9, WDR75, NOC2L, GRWD1, KIAA0020, IMP3, MPHOSPH10, RCL1, WDR46
2	85	RPS15A, RPS20, DDX56, PRKDC, SERBP1, RPF1, RPS12, HIST1H4A, HIST2H3A, RPS18, RPS3, RPS19, RPSA, RPS16, RPS17, GNB2L1, RPS7, RPS10, RPS5, VIM, XRCC6, PABPC1, RPS28, ZCCHC7, HNRNPUL1, PABPC4, RPL23, HNRNPM, RBM10, NOP14, RPL22, RPL38, NOP16, RPL32, RPL7A, BOP1, WDR12, RPL18A, RPL28, RPL7L1, RPS4X, NOC3L, RPL15, PES1, RPL13A, RPL7, DDX47, YBX1, RRP7A, CEBP2, RBM34, PAPD5, DDX51, NLE1, NOL8, URB1, URB2, IGF2BP3, RPS11, RPL14, RPL35A, RPS13, RPS3A, PELP1, WDR18, RPL18, RPL4, EIF6, GTPBP4, RPL10A, RPL9, RPLP2, RPL5, RPL12, RPLP0, RPL11, RPL3, RPS14, NOL10, PPAN-P2RY11, WDR43, DNNTIP2, NOL11, MAK16, RPS9
3	5	DEK, SUB1, EIF2AK2, ARL6IP4, BRD3
4	20	ANXA2, SREK1IP1, SSRP1, SUPT16H, HNRNPA3, PCBP2, HNRNPA2B1, U2AF1, U2AF2, PRPF6, PRPF4, DDX23, PRPF3, SART1, USP39, GTPBP2, SMARCC2, RPLP1, BAZ1B, SENP3-EIF4A1
5	11	ADARB1, STRBP, ADAR, STAU2, ZNF346, ILF2, ILF3, DHX9, ZFR, HNRNPR, SYNCRIP
6	22	RRP8, WDR89, XRCC5, H2AFV, SSBP1, UTP3, PNO1, WDR74, GLTSCR2, RPS27, ELAVL1, RPS26, H2AFY, UPF1, PLEC, UTP20, EWSR1, LARP1, NMNAT1, MOV10, KRT18, RPA1
7	145	DCD, KPRP, POLR2E, SREK1, CASP14, HNRNPDL, HNRNPAB, HNRNPK, HNRNPD, HNRNPL, PIP4K2A, TGM3, TXN, HADHA, PNISR, SRRT, POLR1B, SUGP2, RBMX, RBMXL1, SNRPA, SNRPC, SMC1A, IK, PKP3, HNRNPH2, SF1, LMNA, GAPDH, RRP12, GPATCH8, CYR61, SRSF2, AQR, NCBP1, SAFB2, KPNA2, ZRANB2, CWC25, STAU1, HIST1H1T, PRDX1, C3orf17, NPM3, CHAF1B, CWF19L2, INO80, C1orf131, DHX36, PINX1, POLR2A, NKAP, ZNF668, KPNA3, ANKRD11, DDX28, EMD, ZNF770, BCKDHB, PIP, HACD3, HADHB, PRPF38A, RAE1, JPH1, BTBD1, TWISTNB, RBM22, TECR, C11orf57, CRYZ, HMGB1, PARP1, AKAP8, TAF13, PTBP1, ABCF1, EIF5B, LUC7L3, PPIB, FRG1, HMGB2, RPL39P5, FIBP, KRT6B, MRPL34, PIP4K2B, RPL26L1, ATP5B, COL1A2, ATP5A1, ENO1, ACTG1, TUBB4B, HSP90AB1, ALDOA, YWHAZ, RAN, ZNF30, EEF1A1P5, TAOK1, KHDRBS1, HNRNPH3, DDX3X, ZNF638, FUS, TAF15, YLPM1, SDAD1, KPNA1, DDX1, RPS19BP1, HSPB1, CHERP, RSL24D1, C7orf50, ISG20L2, ESF1, EXOSC10, RPA2, RRP36, ABT1, RBM42, MDN1, RPA3, WDR5, PRPF31, LSM8, PPIH, RPS21, BAG2, RPS15, PPHLN1, FCF1, TEX10, RPS29, WRAP53, RPL21, RAD23B, FAM207A, NVL, XPC

Appendix

Supplementary Table 10 GOBP enrichment analysis of biological processes in individual clusters

Cluster 1								
ID	Description	GeneRatio	BgRatio	pvalue	p.adjust	qvalue	geneID	Count
GO:0042254	ribosome biogenesis	20/25	90/295	1,26E-07	2,5E-05	2,5E-05	BMS1/RRP 20	
GO:0006364	rRNA processing	18/25	72/295	1,79E-07	2,5E-05	2,5E-05	BMS1/RRP 18	
Cluster 2								
ID	Description	GeneRatio	BgRatio	pvalue	p.adjust	qvalue	geneID	Count
GO:0002181	cytoplasmic translation	43/83	58/295	1,67E-16	8,04E-14	7,48E-14	RPS15A/RI 43	
GO:0034645	cellular macromolecule biosynthetic process	50/83	85/295	5,12E-13	4,92E-11	4,58E-11	RPS15A/RI 50	
GO:1901566	organonitrogen compound biosynthetic process	50/83	94/295	1,67E-10	1E-08	9,35E-09	RPS15A/RI 50	
GO:0004470	maturation of LSU-rRNA	11/83	12/295	4,87E-06	0,000213	0,000198	RPL7A/BO 11	
GO:0006364	rRNA processing	34/83	72/295	5,15E-05	0,001559	0,00145	DDX56/PR 34	
Cluster 3								
none								
Cluster 4								
ID	Description	GeneRatio	BgRatio	pvalue	p.adjust	qvalue	geneID	Count
GO:0000398	mRNA splicing, via spliceosome	10/19	40/295	2,66E-05	0,002618	0,002495	HNRNPA3 10	
Cluster 5								
ID	Description	GeneRatio	BgRatio	pvalue	p.adjust	qvalue	geneID	Count
GO:0140546	defense response to symbiont	4/9	12/295	0,00018	0,029551	0,025786	ADARB1/A 4	
GO:0050792	regulation of viral process	4/9	13/295	0,000257	0,029551	0,025786	ADARB1/A 4	
GO:0009605	response to external stimulus	6/9	47/295	0,000703	0,04297	0,037497	ADARB1/S 6	
Cluster 6								
none								
Cluster 7								
none								

Supplementary Table 11 Reactome downregulated genes 24h ANRIL knockdown

ID	Description	GeneRatio	BgRatio	RichFactor	FoldEnrichm	zScore	pvalue	p.adjust	qvalue	geneID	Count
R-HSA-33715	Attenuation phase	4/192	14/10908	0,28571429	16,2321429	7,63340412	8,1108E-05	0,00629292	0,00529203	HSP90AA1/F	4
R-HSA-33715	HSF1 activation	3/192	12/10908	0,25	14,203125	6,12520642	0,00105056	0,02731462	0,02297019	HSP90AA1/H	3
R-HSA-38103	ATF6 (ATF6-alpha) activates chaperones	3/192	12/10908	0,25	14,203125	6,12520642	0,00105056	0,02731462	0,02297019	MBTPS2/ATF	3
R-HSA-90134	RHOBTB2 GTPase cycle	5/192	23/10908	0,2173913	12,3505435	7,29379036	4,1701E-05	0,00542113	0,00455889	MSI2/HSP90a	5
R-HSA-21099	Basigin interactions	5/192	25/10908	0,2	11,3625	6,94299978	6,3987E-05	0,00629292	0,00529203	SLC7A6/ATP	5
R-HSA-39995	Sema3A PAK dependent Axon repulsion	3/192	15/10908	0,2	11,3625	5,37555537	0,0020898	0,03657146	0,03075471	HSP90AA1/H	3
R-HSA-89505	Gene and protein expression by JAK-STAT signaling after Interleukin-12 stimulation	7/192	36/10908	0,19444444	11,046875	8,08191812	2,5425E-06	0,00077122	0,00064856	CDCA2/LCP1	7
R-HSA-96159	Postmitotic nuclear pore complex (NPC) reformation	5/192	27/10908	0,18518519	10,5208333	6,62993634	9,4487E-05	0,00629292	0,00529203	NDCL1/SUMO	5
R-HSA-90205	Interleukin-12 signaling	8/192	45/10908	0,17777778	10,1	8,1876577	9,8389E-07	0,00044721	0,00037608	VAMP7/CDC	8
R-HSA-89345	Regulation of RUNX1 Expression and Activity	3/192	17/10908	0,17647059	10,0257353	4,9849418	0,00304337	0,04540109	0,03817998	AGO1/AGO2	3
R-HSA-98209	Respiratory syncytial virus (RSV) genome replication, transcription and translation	3/192	17/10908	0,17647059	10,0257353	4,9849418	0,00304337	0,04540109	0,03817998	SPCS1/HSP9a	3
R-HSA-44711	Interleukin-12 family signaling	9/192	54/10908	0,16666667	9,46875	8,35041774	3,6096E-07	0,00032847	0,00027623	VAMP7/CDC	9
R-HSA-20392	MicroRNA (miRNA) biogenesis	4/192	24/10908	0,16666667	9,46875	5,55926767	0,00075013	0,02133185	0,01793899	DICER1/AGO	4
R-HSA-33715	HSF1-dependent transactivation	4/192	24/10908	0,16666667	9,46875	5,55926767	0,00075013	0,02133185	0,01793899	HSP90AA1/F	4
R-HSA-18074	Nuclear import of Rev protein	5/192	33/10908	0,15151515	8,60795455	5,85864475	0,00025499	0,01087841	0,00914818	NDCL1/POM1	5
R-HSA-35223	Amino acid transport across the plasma membrane	5/192	33/10908	0,15151515	8,60795455	5,85864475	0,00025499	0,01087841	0,00914818	SLC7A2/SLC7	5
R-HSA-97065	RHOBTB GTPase Cycle	5/192	35/10908	0,14285714	8,11607143	5,64399403	0,00033897	0,01285276	0,00080851	HSP90AA1/H	5
R-HSA-17724	Interactions of Rev with host cellular proteins	5/192	36/10908	0,13888889	7,890625	5,4296406	0,00038808	0,01307977	0,01099941	NDCL1/POM1	5
R-HSA-46158	SUMOylation of DNA replication proteins	5/192	45/10908	0,13333333	7,575	5,91580762	0,00012653	0,00719657	0,00605194	BIRC5/NDCL1	6
R-HSA-16827	Transport of Ribonucleoproteins into the Host Nucleus	4/192	31/10908	0,12903226	7,33064516	4,72455787	0,00201785	0,0360969	0,03035564	NDCL1/KPNA	4
R-HSA-16833	NEP/NS2 Interacts with the Cellular Export Machinery	4/192	31/10908	0,12903226	7,33064516	4,72455787	0,00201785	0,0360969	0,03035564	NDCL1/POM1	4
R-HSA-16827	Export of Viral Ribonucleoproteins from Nucleus	4/192	33/10908	0,12121212	6,88636364	4,53290214	0,00255335	0,040764	0,03428043	NDCL1/POM1	4
R-HSA-18091	Vpr-mediated nuclear import of PICs	4/192	33/10908	0,12121212	6,88636364	4,53290214	0,00255335	0,040764	0,03428043	NDCL1/KPNA	4
R-HSA-90226	Regulation of MECP2 expression and activity	4/192	33/10908	0,12121212	6,88636364	4,53290214	0,00255335	0,040764	0,03428043	TBL1X/AGO1	4
R-HSA-16505	Rev-mediated nuclear export of HIV RNA	4/192	34/10908	0,11764706	6,6882353	4,44295892	0,0028545	0,04402704	0,03702447	NDCL1/POM1	4
R-HSA-40853	SUMOylation of SUMOylation proteins	4/192	34/10908	0,11764706	6,6882353	4,44295892	0,0028545	0,04402704	0,03702447	NDCL1/SUMO	4
R-HSA-99133	Formation of the dystrophin-glycoprotein complex (DGC)	4/192	35/10908	0,11428571	6,49285714	4,35656854	0,00317908	0,04666075	0,03923929	UTRN/LAMC	4
R-HSA-90134	RHO GTPase cycle	6/192	36/10908	0,10714286	6,08705357	5,10848768	0,00042971	0,01396561	0,01174436	CDCA2/SLC7	6
R-HSA-45704	SUMOylation of RNA binding proteins	5/192	47/10908	0,10638298	6,04388298	4,63837591	0,00135059	0,03414004	0,02871001	NDCL1/SUMO	5
R-HSA-33715	Cellular response to heat stress	5/192	89/10908	0,1011236	5,74508427	6,01633889	2,5392E-05	0,00473427	0,00398128	NDCL1/HSP90	9
R-HSA-14451	Translocation of SLC2A4 (GLUT4) to the plasma membrane	7/192	71/10908	0,09895155	5,60123239	5,20637834	0,00024096	0,01087841	0,00914818	TBC1D4/PRK	7
R-HSA-38107	IRE1alpha activates chaperones	5/192	51/10908	0,09803922	5,56985294	4,37843909	0,00195436	0,0360969	0,03035564	NDCL1/SSR1	5
R-HSA-55787	Transcriptional regulation by small RNAs	7/192	72/10908	0,09722222	5,5234375	5,15405853	0,00026299	0,01087841	0,00914818	NDCL1/AGO1	7
R-HSA-56288	TP53 Regulates Metabolic Genes	8/192	83/10908	0,09638554	5,47590361	4,47889198	0,00010166	0,00629292	0,00529203	CYC3/PRKAB	8
R-HSA-90134	RHO GTPase cycle	5/192	54/10908	0,09259259	5,26041667	4,20088666	0,00252181	0,040764	0,03428043	CDCA2/SLC4	5
R-HSA-31082	SUMOylation of DNA damage response and repair proteins	7/192	76/10908	0,09210526	5,23273026	4,95632735	0,0003679	0,01307977	0,01099941	NDCL1/SUMO	7
R-HSA-90185	Estrogen-dependent gene expression	10/192	115/10908	0,08695652	4,94021739	5,685713	3,3937E-05	0,00514705	0,00432841	FOSB/AGO1	10
R-HSA-21100	Gene Silencing by RNA	9/192	104/10908	0,08653846	4,91646635	5,37162516	8,7503E-05	0,00629292	0,00529203	NDCL1/DICER	9
R-HSA-45516	SUMOylation of chromatin organization proteins	5/192	58/10908	0,0862069	4,89762931	3,98369597	0,00345311	0,04987827	0,01494506	NDCL1/SUMO	5
R-HSA-38111	Unfolded Protein Response (UPR)	8/192	94/10908	0,08510638	4,83510638	4,99844685	0,00024337	0,01087841	0,00914818	HYOU1/MBT1	8
R-HSA-11694	IGS15 antiviral mechanism	6/192	72/10908	0,08333333	4,734375	4,25536283	0,00163994	0,0360969	0,03035564	NDCL1/KPNA	6
R-HSA-90131	RHO GTPase cycle	6/192	72/10908	0,08333333	4,734375	4,25536283	0,00163994	0,0360969	0,03035564	ANLN/ACBD1	6
R-HSA-90134	RHO GTPase cycle	6/192	73/10908	0,08219178	4,66952055	4,21059252	0,00176048	0,0360969	0,03035564	CDCA2/LETM	6
R-HSA-29954	Nuclear Envelope (NE) Reassembly	6/192	74/10908	0,08108108	4,60641892	4,16662615	0,00188829	0,0360969	0,03035564	NDCL1/SUMO	6
R-HSA-56871	MAPK6/MAPK4 signaling	6/192	75/10908	0,08	4,545	4,12343752	0,00202301	0,0360969	0,03035564	CDCA2/AGO1	6
R-HSA-98334	PKR-mediated signaling	6/192	75/10908	0,08	4,545	4,12343752	0,00202301	0,0360969	0,03035564	MAP2K6/SUF	6
R-HSA-98566	MIF-M-dependent gene expression	8/192	103/10908	0,0776699	4,41262136	4,65780443	0,00045444	0,01425994	0,01199187	DICER1/AGO	8
R-HSA-16290	Host Interactions of HIV factors	9/192	116/10908	0,07758621	4,40786638	4,9390964	0,00020261	0,01084541	0,00912043	NDCL1/KPNA	9
R-HSA-11694	Antiviral mechanism by IFN-stimulated genes	11/192	148/10908	0,07432432	4,22255068	5,2833745	5,92E-05	0,00629292	0,00529203	DICER1/MAP2	11
R-HSA-96791	Potential therapeutics for SARS	7/192	97/10908	0,07216495	4,09987113	4,10471957	0,0015864	0,0360969	0,03035564	GATAD2A/IF	7
R-HSA-97304	MIF-M-regulated melanocyte development	11/192	154/10908	0,07142857	4,05803571	5,11569703	8,4924E-05	0,00629292	0,00529203	DICER1/SUMO	11
R-HSA-16825	Influenza Infection	10/192	154/10908	0,06493506	3,68912338	4,49855455	0,00038652	0,01307977	0,01099941	NDCL1/CANX	10
R-HSA-31082	SUMO3 E3 ligases SUMOylate target proteins	10/192	167/10908	0,05988024	3,40194611	4,18683701	0,00077312	0,02133185	0,01793899	BIRC5/NDCL1	10
R-HSA-29908	SUMOylation	10/192	172/10908	0,05813953	3,30305233	4,07505707	0,00091795	0,02531321	0,0212871	BIRC5/NDCL1	10
R-HSA-89392	ESR-mediated signaling	10/192	188/10908	0,05319149	3,02194149	3,7431483	0,00179566	0,0360969	0,03035564	FOSB/AGO1	10
R-HSA-91353	Interferon Signaling	11/192	270/10908	0,05185185	2,94583333	4,33355633	0,00029592	0,01170823	0,0094602	NDCL1/MAP2	11
R-HSA-68882	Mitotic Anaphase	14/192	220/10908	0,05	2,840625	3,69160608	0,00175995	0,0360969	0,03035564	BIRC5/NDCL1	14
R-HSA-25553	Mitotic Metaphase and Anaphase	11/192	221/10908	0,04977376	2,82777149	3,67432062	0,00182426	0,0360969	0,03035564	BIRC5/NDCL1	11
R-HSA-90129	RHO GTPase cycle	21/192	435/10908	0,04827586	2,74267241	4,96491424	2,6012E-05	0,0047342			

Appendix

Supplementary Table 12 GOBP downregulated genes 48h ANRIL knockdown

ID	Description	GeneRatio	BgRatio	RichFactor	FoldEnrichm	zScore	pvalue	p.adjust	qvalue	geneID	Count
GO:0046598	positive regulation of viral entry into host cell	4/402	15/18235	0,26666667	12,0961857	6,45486194	0,00026193	0,02870746	0,02688617	TRIM11/LGAI	4
GO:0075294	positive regulation by symbiont of entry into host	4/402	15/18235	0,26666667	12,0961857	6,45486194	0,00026193	0,02870746	0,02688617	TRIM11/LGAI	4
GO:0046596	regulation of viral entry into host cell	5/402	20/18235	0,25	11,3401741	6,94656429	5,9916E-05	0,01509904	0,01414111	TRIM11/NEC	5
GO:0001522	pseudouridine synthesis	4/402	16/18235	0,25	11,3401741	6,21251389	0,00034319	0,03558019	0,03332287	PUSL1/RPUSI	4
GO:0052372	modulation by symbiont of entry into host	6/402	27/18235	0,22222222	10,0801548	7,08901358	2,2106E-05	0,0144315	0,01351591	TRIM11/NEC	6
GO:0043903	regulation of biological process involved in symbiotic interaction	7/402	41/18235	0,17073171	7,74450916	6,4911251	2,8273E-05	0,0144315	0,01351591	TRIM11/NEC	7
GO:0006734	NADH metabolic process	6/402	39/18235	0,15384615	6,97856869	5,61155676	0,00019488	0,02645685	0,02477834	SLC25A22/SL	6
GO:0042255	ribosome assembly	8/402	56/18235	0,14285714	6,4800995	6,16650744	2,9295E-05	0,0144315	0,01351591	BOP1/DHX37	8
GO:0006383	transcription by RNA polymerase III	7/402	62/18235	0,11290323	5,12136686	4,88051694	0,00041584	0,04055806	0,03798493	POLR3K/SNA	7
GO:0006360	transcription by RNA polymerase I	8/402	78/18235	0,1025641	4,65237913	4,85336444	0,00031731	0,03381127	0,03166618	FLNA/POLR2	8
GO:2000060	positive regulation of ubiquitin-dependent protein catabolic process	10/402	104/18235	0,09615385	4,36160543	5,1617186	0,00010018	0,01830009	0,01713907	DVLI/TRIB3/	10
GO:0044409	symbiont entry into host	12/402	134/18235	0,08955224	4,06215193	5,34157888	4,1903E-05	0,0144315	0,01351591	SLC25A22/TRI	12
GO:1901800	positive regulation of proteasomal protein catabolic process	10/402	113/18235	0,08849558	4,01422093	4,82561908	0,00020001	0,02645685	0,02477834	DVLI/TMEM1	10
GO:0042274	ribosomal small subunit biogenesis	9/402	102/18235	0,08823529	4,0024144	4,56538793	0,00042292	0,04055806	0,03798493	RPS19BP1/RI	9
GO:0046718	symbiont entry into host cell	11/402	129/18235	0,08527132	3,86796637	4,9079423	0,00013531	0,02162637	0,02025433	SLC25A2/TRI	11
GO:1903052	positive regulation of proteolysis involved in protein catabolic process	11/402	136/18235	0,08088235	3,66887987	4,69043354	0,00021593	0,0269813	0,02526951	DVLI/TMEM1	11
GO:0019362	pyridine nucleotide metabolic process	13/402	176/18235	0,07386364	3,35050599	4,70449103	0,00014814	0,021857	0,02047032	SLC25A22/Ni	13
GO:0046496	nicotinamide nucleotide metabolic process	13/402	176/18235	0,07386364	3,35050599	4,70449103	0,00014814	0,021857	0,02047032	SLC25A22/Ni	13
GO:0042254	ribosome biogenesis	22/402	305/18235	0,07213115	3,27191909	6,00750904	1,2342E-06	0,00236713	0,00221695	RPS19BP1/RI	22
GO:0072524	pyridine-containing compound metabolic process	13/402	183/18235	0,07103825	3,22234456	4,53644943	0,00021804	0,0269813	0,02526951	SLC25A22/Ni	13
GO:0044403	biological process involved in symbiotic interaction	15/402	214/18235	0,07009346	3,17948807	4,81519342	8,4752E-05	0,0164426	0,01539943	SLC25A2/TRI	15
GO:0009199	ribonucleoside triphosphate metabolic process	18/402	258/18235	0,06976744	3,16469976	5,25763834	1,8042E-05	0,0144315	0,01351591	SLC25A25/ITI	18
GO:0051701	biological process involved in interaction with host	12/402	171/18235	0,06976744	3,16469976	4,28261218	0,00044497	0,04163174	0,03899049	SLC25A2/TRI	12
GO:0045862	positive regulation of proteolysis	15/402	219/18235	0,06849315	3,10689702	4,70953444	0,00010977	0,01867357	0,01748885	DVLI/ASPH/	15
GO:0009205	purine ribonucleoside triphosphate metabolic process	17/402	251/18235	0,06772908	3,07223841	4,96335376	4,4696E-05	0,0144315	0,01351591	SLC25A25/ITI	17
GO:0016072	rRNA metabolic process	17/402	256/18235	0,06640625	3,01223375	4,86807704	5,718E-05	0,01509904	0,01414111	RPUSDI/BOF	17
GO:0045732	positive regulation of protein catabolic process	14/402	211/18235	0,06635071	3,00971446	4,40850962	0,00025666	0,02870746	0,02688617	RHBD3/DVI	14
GO:0009144	purine nucleoside triphosphate metabolic process	17/402	258/18235	0,06589147	2,9888831	4,83061359	6,2978E-05	0,01509904	0,01414111	SLC25A25/ITI	17
GO:0009141	nucleoside triphosphate metabolic process	18/402	274/18235	0,06569343	2,97989977	4,95786877	4,0086E-05	0,0144315	0,01351591	SLC25A25/ITI	18
GO:0046034	ATP metabolic process	15/402	229/18235	0,06550218	2,97122466	4,50699462	0,00017966	0,02525553	0,0239061	SLC25A25/NI	15
GO:0071826	protein-RNA complex organization	14/402	227/18235	0,06167401	2,797576	4,09175145	0,00053701	0,04790627	0,04486694	TSSC4/BOP1,	14
GO:0022613	ribonucleoprotein complex biogenesis	29/402	475/18235	0,06105263	2,76938989	5,86665654	8,2965E-07	0,00236713	0,00221695	TSSC4/RPS15	29
GO:0009150	purine ribonucleotide metabolic process	20/402	343/18235	0,05830904	2,64493857	4,61752331	8,1135E-05	0,0164426	0,01539943	SLC25A25/ITI	20
GO:0009259	ribonucleotide metabolic process	21/402	364/18235	0,05769231	2,61696326	4,67862475	6,297E-05	0,01509904	0,01414111	SLC25A25/ITI	21
GO:0042176	regulation of protein catabolic process	21/402	371/18235	0,05660377	2,5675866	4,58005758	8,2532E-05	0,0164426	0,01539943	RHBD3/DVI	21
GO:0019693	ribose phosphate metabolic process	21/402	372/18235	0,05645161	2,56068448	4,56616057	8,5728E-05	0,0164426	0,01539943	SLC25A25/ITI	21
GO:0006163	purine nucleotide metabolic process	24/402	437/18235	0,05491991	2,4912053	4,73733779	4,1999E-05	0,0144315	0,01351591	SLC25A25/SL	24
GO:0007005	mitochondrion organization	24/402	439/18235	0,0546697	2,47985585	4,71229284	4,5145E-05	0,0144315	0,01351591	UOCCA/ATAI	24
GO:0006091	generation of precursor metabolites and energy	26/402	479/18235	0,05427975	2,46216724	4,86893566	2,4645E-05	0,0144315	0,01351591	SLC25A25/NI	26
GO:0016032	viral process	21/402	400/18235	0,0525	2,38143657	4,19436464	0,00023352	0,0279938	0,02621778	JUN/SLC52A,	21
GO:0009117	nucleotide metabolic process	25/402	495/18235	0,05050505	2,29094427	4,37194895	0,00011196	0,01867357	0,01748885	SLC25A25/SL	25
GO:0140694	membraneless organelle assembly	21/402	417/18235	0,05035971	2,28435162	3,98349509	0,00040669	0,04055806	0,03798493	RNF4/BOP1/	21
GO:0030162	regulation of proteolysis	21/402	423/18235	0,04964539	2,25194947	3,91149193	0,00049029	0,04477995	0,04193896	THBS1/DVLI,	21

References

1. Zhang, Z., Li, L., Shi, H., Chen, B., Li, X., Zhang, Y., Liu, F., Wei, W., Zhou, Y., Liu, K. *et al.* (2023) Role of Circular RNAs in Atherosclerosis through Regulation of Inflammation, Cell Proliferation, Migration, and Apoptosis: Focus on Atherosclerotic Cerebrovascular Disease. *Medicina*, **59**, 1461.
2. Mudge, Jonathan M., Carbonell-Sala, S., Diekhans, M., Martinez, Jose G., Hunt, T., Jungreis, I., Loveland, Jane E., Arnan, C., Barnes, I., Bennett, R. *et al.* (2024) GENCODE 2025: reference gene annotation for human and mouse. *Nucleic Acids Research*, **53**, D966-D975.
3. Mattick, J.S., Amaral, P.P., Carninci, P., Carpenter, S., Chang, H.Y., Chen, L.L., Chen, R., Dean, C., Dinger, M.E., Fitzgerald, K.A. *et al.* (2023) Long non-coding RNAs: definitions, functions, challenges and recommendations. *Nat Rev Mol Cell Biol*, **24**, 430-447.
4. Gomes, C.P.d.C., Ágg, B., Andova, A., Arslan, S., Baker, A., Barteková, M., Beis, D., Betsou, F., Bezzina Wettinger, S., Bugarski, B. *et al.* (2019) Catalyzing Transcriptomics Research in Cardiovascular Disease: The CardioRNA COST Action CA17129. *Non-Coding RNA*, **5**, 31.
5. Poliseno, L., Lanza, M. and Pandolfi, P.P. (2024) Coding, or non-coding, that is the question. *Cell Research*, **34**, 609-629.
6. Zhang, P., Wu, W., Chen, Q. and Chen, M. (2019) Non-Coding RNAs and their Integrated Networks. *J Integr Bioinform*, **16**.
7. Naseer, Q.A., Malik, A., Zhang, F. and Chen, S. (2024) Exploring the enigma: history, present, and future of long non-coding RNAs in cancer. *Discover Oncology*, **15**, 214.
8. Fernandes, J.C.R., Acuña, S.M., Aoki, J.I., Floeter-Winter, L.M. and Muxel, S.M. (2019) Long Non-Coding RNAs in the Regulation of Gene Expression: Physiology and Disease. *Noncoding RNA*, **5**.
9. Milligan, M.J. and Lipovich, L. (2014) Pseudogene-derived lncRNAs: emerging regulators of gene expression. *Front Genet*, **5**, 476.
10. Constanty, F. and Shkumatava, A. (2021) lncRNAs in development and differentiation: from sequence motifs to functional characterization. *Development*, **148**.
11. Khan, M.R., Avino, M., Wellinger, R.J. and Laurent, B. (2023) Distinct regulatory functions and biological roles of lncRNA splice variants. *Molecular Therapy Nucleic Acids*, **32**, 127-143.
12. Khan, M.R., Wellinger, R.J. and Laurent, B. (2021) Exploring the Alternative Splicing of Long Noncoding RNAs. *Trends in Genetics*, **37**, 695-698.
13. Price, R.L., Bhan, A. and Mandal, S.S. (2021) HOTAIR beyond repression: In protein degradation, inflammation, DNA damage response, and cell signaling. *DNA Repair*, **105**, 103141.
14. Tsai, M.-C., Manor, O., Wan, Y., Mosammamparast, N., Wang, J.K., Lan, F., Shi, Y., Segal, E. and Chang, H.Y. (2010) Long Noncoding RNA as Modular Scaffold of Histone Modification Complexes. *Science*, **329**, 689-693.

References

15. Potolitsyna, E., Hazell Pickering, S., Tooming-Klunderud, A., Collas, P. and Briand, N. (2022) De novo annotation of lncRNA HOTAIR transcripts by long-read RNA capture-seq reveals a differentiation-driven isoform switch. *BMC Genomics*, **23**, 658.
16. Patop, I.L., Wüst, S. and Kadener, S. (2019) Past, present, and future of circRNAs. *The EMBO Journal*, **38**, e100836.
17. Kristensen, L.S., Andersen, M.S., Stagsted, L.V.W., Ebbesen, K.K., Hansen, T.B. and Kjems, J. (2019) The biogenesis, biology and characterization of circular RNAs. *Nature Reviews Genetics*, **20**, 675-691.
18. Chodurska, B. and Kunej, T. (2025) Long non-coding RNAs in humans: Classification, genomic organization and function. *Non-coding RNA Research*, **11**, 313-327.
19. Jeck, W.R., Sorrentino, J.A., Wang, K., Slevin, M.K., Burd, C.E., Liu, J., Marzluff, W.F. and Sharpless, N.E. (2013) Circular RNAs are abundant, conserved, and associated with ALU repeats. *Rna*, **19**, 141-157.
20. Derrien, T., Johnson, R., Bussotti, G., Tanzer, A., Djebali, S., Tilgner, H., Guernec, G., Martin, D., Merkel, A., Knowles, D.G. *et al.* (2012) The GENCODE v7 catalog of human long noncoding RNAs: analysis of their gene structure, evolution, and expression. *Genome Res*, **22**, 1775-1789.
21. Sun, Q., Hao, Q. and Prasanth, K.V. (2018) Nuclear Long Noncoding RNAs: Key Regulators of Gene Expression. *Trends Genet*, **34**, 142-157.
22. Bridges, M.C., Daulagala, A.C. and Kourtidis, A. (2021) LNCcation: lncRNA localization and function. *J Cell Biol*, **220**.
23. Gibb, E.A., Vucic, E.A., Enfield, K.S.S., Stewart, G.L., Lonergan, K.M., Kennett, J.Y., Becker-Santos, D.D., MacAulay, C.E., Lam, S., Brown, C.J. *et al.* (2011) Human Cancer Long Non-Coding RNA Transcriptomes. *PLOS ONE*, **6**, e25915.
24. Noh, J.H., Kim, K.M., McClusky, W.G., Abdelmohsen, K. and Gorospe, M. (2018) Cytoplasmic functions of long noncoding RNAs. *Wiley Interdiscip Rev RNA*, **9**, e1471.
25. Statello, L., Guo, C.J., Chen, L.L. and Huarte, M. (2021) Gene regulation by long non-coding RNAs and its biological functions. *Nat Rev Mol Cell Biol*, **22**, 96-118.
26. Xie, Y. and Wei, Y. (2021) A Novel Regulatory Player in the Innate Immune System: Long Non-Coding RNAs. *International Journal of Molecular Sciences*, **22**, 9535.
27. Marchese, F.P., Raimondi, I. and Huarte, M. (2017) The multidimensional mechanisms of long noncoding RNA function. *Genome Biol*, **18**, 206.
28. Karlsson, O. and Baccarelli, A.A. (2016) Environmental Health and Long Non-coding RNAs. *Curr Environ Health Rep*, **3**, 178-187.
29. Petermann, E., Lan, L. and Zou, L. (2022) Sources, resolution and physiological relevance of R-loops and RNA-DNA hybrids. *Nature Reviews Molecular Cell Biology*, **23**, 521-540.
30. Graf, M., Bonetti, D., Lockhart, A., Serhal, K., Kellner, V., Maicher, A., Jolivet, P., Teixeira, M.T. and Luke, B. (2017) Telomere Length Determines TERRA and R-Loop Regulation through the Cell Cycle. *Cell*, **170**, 72-85.e14.

References

31. Boque-Sastre, R., Soler, M., Oliveira-Mateos, C., Portela, A., Moutinho, C., Sayols, S., Villanueva, A., Esteller, M. and Guil, S. (2015) Head-to-head antisense transcription and R-loop formation promotes transcriptional activation. *Proc Natl Acad Sci U S A*, **112**, 5785-5790.
32. Zhu, L., Wei, Q., Qi, Y., Ruan, X., Wu, F., Li, L., Zhou, J., Liu, W., Jiang, T., Zhang, J. *et al.* (2019) PTB-AS, a Novel Natural Antisense Transcript, Promotes Glioma Progression by Improving PTBP1 mRNA Stability with SND1. *Mol Ther*, **27**, 1621-1637.
33. Li, Z., Jiang, P., Li, J., Peng, M., Zhao, X., Zhang, X., Chen, K., Zhang, Y., Liu, H., Gan, L. *et al.* (2018) Tumor-derived exosomal lnc-Sox2ot promotes EMT and stemness by acting as a ceRNA in pancreatic ductal adenocarcinoma. *Oncogene*, **37**, 3822-3838.
34. Yoon, J.H., Abdelmohsen, K. and Gorospe, M. (2014) Functional interactions among microRNAs and long noncoding RNAs. *Semin Cell Dev Biol*, **34**, 9-14.
35. Yoon, J.H., Abdelmohsen, K., Kim, J., Yang, X., Martindale, J.L., Tominaga-Yamanaka, K., White, E.J., Orjalo, A.V., Rinn, J.L., Kreft, S.G. *et al.* (2013) Scaffold function of long non-coding RNA HOTAIR in protein ubiquitination. *Nat Commun*, **4**, 2939.
36. Ribeiro, D.M., Zanzoni, A., Cipriano, A., Delli Ponti, R., Spinelli, L., Ballarino, M., Bozzoni, I., Tartaglia, G.G. and Brun, C. (2017) Protein complex scaffolding predicted as a prevalent function of long non-coding RNAs. *Nucleic Acids Research*, **46**, 917-928.
37. Wang, Z., Aftab, M., Dong, Z., Jiang, Y. and Liu, K. (2025) LncRNA–Protein Interactions: A Key to Deciphering LncRNA Mechanisms. *Biomolecules*, **15**, 881.
38. Schuettengruber, B., Chourrout, D., Vervoort, M., Leblanc, B. and Cavalli, G. (2007) Genome Regulation by Polycomb and Trithorax Proteins. *Cell*, **128**, 735-745.
39. Mondal, T., Subhash, S., Vaid, R., Enroth, S., Uday, S., Reinius, B., Mitra, S., Mohammed, A., James, A.R., Hoberg, E. *et al.* (2015) MEG3 long noncoding RNA regulates the TGF- β pathway genes through formation of RNA–DNA triplex structures. *Nature Communications*, **6**, 7743.
40. Hung, T., Wang, Y., Lin, M.F., Koegel, A.K., Kotake, Y., Grant, G.D., Horlings, H.M., Shah, N., Umbricht, C., Wang, P. *et al.* (2011) Extensive and coordinated transcription of noncoding RNAs within cell-cycle promoters. *Nature Genetics*, **43**, 621-629.
41. Roake, C.M. and Artandi, S.E. (2020) Regulation of human telomerase in homeostasis and disease. *Nature Reviews Molecular Cell Biology*, **21**, 384-397.
42. Kazimierczyk, M., Kasprowicz, M.K., Kasprzyk, M.E. and Wrzesinski, J. (2020) Human Long Noncoding RNA Interactome: Detection, Characterization and Function. *International Journal of Molecular Sciences*, **21**, 1027.
43. Yang, Y., Wen, L. and Zhu, H. (2015) Unveiling the hidden function of long non-coding RNA by identifying its major partner-protein. *Cell & Bioscience*, **5**, 59.
44. Marchese, D., de Groot, N.S., Lorenzo Gotor, N., Livi, C.M. and Tartaglia, G.G. (2016) Advances in the characterization of RNA-binding proteins. *Wiley Interdiscip Rev RNA*, **7**, 793-810.

References

45. Ray, D., Ha, K.C.H., Nie, K., Zheng, H., Hughes, T.R. and Morris, Q.D. (2017) RNAcompete methodology and application to determine sequence preferences of unconventional RNA-binding proteins. *Methods*, **118-119**, 3-15.
46. Gerber, A.P. (2021) RNA-Centric Approaches to Profile the RNA-Protein Interaction Landscape on Selected RNAs. *Noncoding RNA*, **7**.
47. Faoro, C. and Ataide, S.F. (2014) Ribonomic approaches to study the RNA-binding proteome. *FEBS Lett*, **588**, 3649-3664.
48. Pasmant, E., Laurendeau, I., Heron, D., Vidaud, M., Vidaud, D. and Bieche, I. (2007) Characterization of a germ-line deletion, including the entire INK4/ARF locus, in a melanoma-neural system tumor family: identification of ANRIL, an antisense noncoding RNA whose expression coclusters with ARF. *Cancer Res*, **67**, 3963-3969.
49. Holdt, L.M. and Teupser, D. (2013) From genotype to phenotype in human atherosclerosis - recent findings. *Current Opinion in Lipidology*, **24**.
50. Burd, C.E., Jeck, W.R., Liu, Y., Sanoff, H.K., Wang, Z. and Sharpless, N.E. (2010) Expression of Linear and Novel Circular Forms of an INK4/ARF-Associated Non-Coding RNA Correlates with Atherosclerosis Risk. *PLOS Genetics*, **6**, e1001233.
51. Dyer, S.C., Austine-Orimoloye, O., Azov, A.G., Barba, M., Barnes, I., Barrera-Enriquez, V.P., Becker, A., Bennett, R., Beracochea, M., Berry, A. *et al.* (2025) Ensembl 2025. *Nucleic Acids Res*, **53**, D948-d957.
52. He, S., Gu, W., Li, Y. and Zhu, H. (2013) ANRIL/CDKN2B-AS shows two-stage clade-specific evolution and becomes conserved after transposon insertions in simians. *BMC Evol Biol*, **13**, 247.
53. Kong, Y., Hsieh, C.H. and Alonso, L.C. (2018) ANRIL: A lncRNA at the CDKN2A/B Locus With Roles in Cancer and Metabolic Disease. *Front Endocrinol (Lausanne)*, **9**, 405.
54. Sanchez, A., Lhuillier, J., Grosjean, G., Ayadi, L. and Maenner, S. (2023) The Long Non-Coding RNA ANRIL in Cancers. *Cancers (Basel)*, **15**.
55. Sarkar, D., Oghabian, A., Bodiya, P.K., Joseph, W.R., Leung, E.Y., Finlay, G.J., Baguley, B.C. and Askarian-Amiri, M.E. (2017) Multiple Isoforms of ANRIL in Melanoma Cells: Structural Complexity Suggests Variations in Processing. *International Journal of Molecular Sciences*, **18**, 1378.
56. Teng, X., Chen, X., Xue, H., Tang, Y., Zhang, P., Kang, Q., Hao, Y., Chen, R., Zhao, Y. and He, S. (2020) NPInter v4.0: an integrated database of ncRNA interactions. *Nucleic Acids Res*, **48**, D160-d165.
57. Alfeghaly, C., Sanchez, A., Rouget, R., Thuillier, Q., Igel-Bourguignon, V., Marchand, V., Branlant, C., Motorin, Y., Behm-Ansmant, I. and Maenner, S. (2021) Implication of repeat insertion domains in the trans-activity of the long non-coding RNA ANRIL. *Nucleic Acids Res*, **49**, 4954-4970.
58. Kotake, Y., Nakagawa, T., Kitagawa, K., Suzuki, S., Liu, N., Kitagawa, M. and Xiong, Y. (2011) Long non-coding RNA ANRIL is required for the PRC2 recruitment to and silencing of p15(INK4B) tumor suppressor gene. *Oncogene*, **30**, 1956-1962.

References

59. Yap, K.L., Li, S., Munoz-Cabello, A.M., Raguz, S., Zeng, L., Mujtaba, S., Gil, J., Walsh, M.J. and Zhou, M.M. (2010) Molecular interplay of the noncoding RNA ANRIL and methylated histone H3 lysine 27 by polycomb CBX7 in transcriptional silencing of INK4a. *Mol Cell*, **38**, 662-674.
60. Holdt, L.M., Hoffmann, S., Sass, K., Langenberger, D., Scholz, M., Krohn, K., Finstermeier, K., Stahringer, A., Wilfert, W., Beutner, F. *et al.* (2013) Alu Elements in ANRIL Non-Coding RNA at Chromosome 9p21 Modulate Atherogenic Cell Functions through Trans-Regulation of Gene Networks. *PLOS Genetics*, **9**, e1003588.
61. Sherr, C.J. and Roberts, J.M. (1999) CDK inhibitors: positive and negative regulators of G1-phase progression. *Genes Dev*, **13**, 1501-1512.
62. Zhang, Y., Xiong, Y. and Yarbrough, W.G. (1998) ARF Promotes MDM2 Degradation and Stabilizes p53: *ARF-INK4a* Locus Deletion Impairs Both the Rb and p53 Tumor Suppression Pathways. *Cell*, **92**, 725-734.
63. Qiu, J.-J., Lin, Y.-Y., Ding, J.-X., Feng, W.-W., Jin, H.-Y. and Hua, K.-Q. (2015) Long non-coding RNA ANRIL predicts poor prognosis and promotes invasion/metastasis in serous ovarian cancer. *Int J Oncol*, **46**, 2497-2505.
64. Qiu, J.J., Wang, Y., Liu, Y.L., Zhang, Y., Ding, J.X. and Hua, K.Q. (2016) The long non-coding RNA ANRIL promotes proliferation and cell cycle progression and inhibits apoptosis and senescence in epithelial ovarian cancer. *Oncotarget*, **7**, 32478-32492.
65. Liu, M., Xing, L.Q. and Liu, Y.J. (2017) A three-long noncoding RNA signature as a diagnostic biomarker for differentiating between triple-negative and non-triple-negative breast cancers. *Medicine (Baltimore)*, **96**, e6222.
66. Nie, F.-q., Sun, M., Yang, J.-s., Xie, M., Xu, T.-p., Xia, R., Liu, Y.-w., Liu, X.-h., Zhang, E.-b., Lu, K.-h. *et al.* (2015) Long Noncoding RNA ANRIL Promotes Non-Small Cell Lung Cancer Cell Proliferation and Inhibits Apoptosis by Silencing KLF2 and P21 Expression. *Molecular Cancer Therapeutics*, **14**, 268-277.
67. Huang, M.-d., Chen, W.-m., Qi, F.-z., Xia, R., Sun, M., Xu, T.-p., Yin, L., Zhang, E.-b., De, W. and Shu, Y.-q. (2015) Long non-coding RNA ANRIL is upregulated in hepatocellular carcinoma and regulates cell proliferation by epigenetic silencing of KLF2. *Journal of Hematology & Oncology*, **8**, 57.
68. Zhang, C., Ge, S., Gong, W., Xu, J., Guo, Z., Liu, Z., Gao, X., Wei, X. and Ge, S. (2020) LncRNA ANRIL acts as a modular scaffold of WDR5 and HDAC3 complexes and promotes alteration of the vascular smooth muscle cell phenotype. *Cell Death Dis*, **11**, 435.
69. Zhou, X., Han, X., Wittfeldt, A., Sun, J., Liu, C., Wang, X., Gan, L.M., Cao, H. and Liang, Z. (2016) Long non-coding RNA ANRIL regulates inflammatory responses as a novel component of NF-kappaB pathway. *RNA Biol*, **13**, 98-108.
70. Holdt, L.M., Stahringer, A., Sass, K., Pichler, G., Kulak, N.A., Wilfert, W., Kohlmaier, A., Herbst, A., Northoff, B.H., Nicolaou, A. *et al.* (2016) Circular non-coding RNA ANRIL modulates ribosomal RNA maturation and atherosclerosis in humans. *Nat Commun*, **7**, 12429.
71. Grimm, T., Hölzel, M., Rohrmoser, M., Harasim, T., Malamoussi, A., Gruber-Eber, A., Kremmer, E. and Eick, D. (2006) Dominant-negative Pes1 mutants inhibit ribosomal

References

- RNA processing and cell proliferation via incorporation into the PeBoW-complex. *Nucleic Acids Res*, **34**, 3030-3043.
72. Rohrmoser, M., Hölzel, M., Grimm, T., Malamoussi, A., Harasim, T., Orban, M., Pfisterer, I., Gruber-Eber, A., Kremmer, E. and Eick, D. (2007) Interdependence of Pes1, Bop1, and WDR12 controls nucleolar localization and assembly of the PeBoW complex required for maturation of the 60S ribosomal subunit. *Mol Cell Biol*, **27**, 3682-3694.
73. Muniz, L., Lazorthes, S., Delmas, M., Ouvrard, J., Aguirrebengoa, M., Trouche, D. and Nicolas, E. (2021) Circular ANRIL isoforms switch from repressors to activators of p15/CDKN2B expression during RAF1 oncogene-induced senescence. *RNA Biol*, **18**, 404-420.
74. Song, Z., Wu, W., Chen, M., Cheng, W., Yu, J., Fang, J., Xu, L., Yasunaga, J.I., Matsuoka, M. and Zhao, T. (2018) Long Noncoding RNA ANRIL Supports Proliferation of Adult T-Cell Leukemia Cells through Cooperation with EZH2. *J Virol*, **92**.
75. Sethuraman, S., Gay, L.A., Jain, V., Haecker, I. and Renne, R. (2017) microRNA dependent and independent deregulation of long non-coding RNAs by an oncogenic herpesvirus. *PLOS Pathogens*, **13**, e1006508.
76. Wen, K.W. and Damania, B. (2010) Kaposi sarcoma-associated herpesvirus (KSHV): molecular biology and oncogenesis. *Cancer Lett*, **289**, 140-150.
77. Rahni, Z., Hosseini, S.M., Shahrokh, S., Saeedi Niasar, M., Shoraka, S., Mirjalali, H., Nazemalhosseini-Mojarad, E., Rostami-Nejad, M., Malekpour, H., Zali, M.R. *et al.* (2023) Long non-coding RNAs ANRIL, THRIL, and NEAT1 as potential circulating biomarkers of SARS-CoV-2 infection and disease severity. *Virus Res*, **336**, 199214.
78. Ginn, L., La Montagna, M., Wu, Q. and Shi, L. (2021), *Rev Med Virol*. © 2020 John Wiley & Sons Ltd., Vol. 31.
79. Zhang, D., Zhang, M., Zhang, L., Wang, W., Hua, S., Zhou, C. and Sun, X. (2024) Long non-coding RNAs and immune cells: Unveiling the role in viral infections. *Biomedicine & Pharmacotherapy*, **170**, 115978.
80. Qiu, L., Wang, T., Tang, Q., Li, G., Wu, P. and Chen, K. (2018) Long Non-coding RNAs: Regulators of Viral Infection and the Interferon Antiviral Response. *Front Microbiol*, **9**, 1621.
81. Cao, Y., Wu, J., Hu, Y., Chai, Y., Song, J., Duan, J., Zhang, S. and Xu, X. (2023) Virus-induced lncRNA-BTX allows viral replication by regulating intracellular translocation of DHX9 and ILF3 to induce innate escape. *Cell Reports*, **42**.
82. Wang, Y., Chen, X., Xie, J., Zhou, S., Huang, Y., Li, Y.-P., Li, X., Liu, C., He, J. and Zhang, P. (2019) RNA Helicase A Is an Important Host Factor Involved in Dengue Virus Replication. *Journal of Virology*, **93**, 10.1128/jvi.01306-01318.
83. Shen, B., Chen, Y., Hu, J., Qiao, M., Ren, J., Hu, J., Chen, J., Tang, N., Huang, A. and Hu, Y. (2020) Hepatitis B virus X protein modulates upregulation of DHX9 to promote viral DNA replication. *Cell Microbiol*, **22**, e13148.
84. Ouyang, J., Zhu, X., Chen, Y., Wei, H., Chen, Q., Chi, X., Qi, B., Zhang, L., Zhao, Y., Gao, George F. *et al.* (2014) NRAV, a Long Noncoding RNA, Modulates Antiviral Responses

References

- through Suppression of Interferon-Stimulated Gene Transcription. *Cell Host & Microbe*, **16**, 616-626.
85. Ji, X., Meng, W., Liu, Z. and Mu, X. (2022) Emerging Roles of lncRNAs Regulating RNA-Mediated Type-I Interferon Signaling Pathway. *Front Immunol*, **13**, 811122.
 86. Dalskov, L., Gad, H.H. and Hartmann, R. (2023) Viral recognition and the antiviral interferon response. *The EMBO Journal*, **42**, e112907.
 87. Chen, K., Liu, J. and Cao, X. (2017) Regulation of type I interferon signaling in immunity and inflammation: A comprehensive review. *Journal of Autoimmunity*, **83**, 1-11.
 88. Ji, L., Li, T., Chen, H., Yang, Y., Lu, E., Liu, J., Qiao, W. and Chen, H. (2023) The crucial regulatory role of type I interferon in inflammatory diseases. *Cell & Bioscience*, **13**, 230.
 89. Rehwinkel, J. and Gack, M.U. (2020) RIG-I-like receptors: their regulation and roles in RNA sensing. *Nature Reviews Immunology*, **20**, 537-551.
 90. McNab, F., Mayer-Barber, K., Sher, A., Wack, A. and O'Garra, A. (2015) Type I interferons in infectious disease. *Nature Reviews Immunology*, **15**, 87-103.
 91. Kowalinski, E., Lunardi, T., McCarthy, A.A., Loubser, J., Brunel, J., Grigorov, B., Gerlier, D. and Cusack, S. (2011) Structural basis for the activation of innate immune pattern-recognition receptor RIG-I by viral RNA. *Cell*, **147**, 423-435.
 92. Wu, B., Peisley, A., Richards, C., Yao, H., Zeng, X., Lin, C., Chu, F., Walz, T. and Hur, S. (2013) Structural basis for dsRNA recognition, filament formation, and antiviral signal activation by MDA5. *Cell*, **152**, 276-289.
 93. Berke, I.C. and Modis, Y. (2012) MDA5 cooperatively forms dimers and ATP-sensitive filaments upon binding double-stranded RNA. *Embo j*, **31**, 1714-1726.
 94. Peisley, A., Wu, B., Yao, H., Walz, T. and Hur, S. (2013) RIG-I forms signaling-competent filaments in an ATP-dependent, ubiquitin-independent manner. *Mol Cell*, **51**, 573-583.
 95. Seth, R.B., Sun, L., Ea, C.-K. and Chen, Z.J. (2005) Identification and Characterization of MAVS, a Mitochondrial Antiviral Signaling Protein that Activates NF- κ B and IRF3. *Cell*, **122**, 669-682.
 96. Chen, Y., Shi, Y., Wu, J. and Qi, N. (2021) MAVS: A Two-Sided CARD Mediating Antiviral Innate Immune Signaling and Regulating Immune Homeostasis. *Frontiers in Microbiology*, **Volume 12 - 2021**.
 97. Dong, H. and Shen, J. (2024) MAVS Ubiquitylation: Function, Mechanism, and Beyond. *FBL*, **29**.
 98. Liu, S., Cai, X., Wu, J., Cong, Q., Chen, X., Li, T., Du, F., Ren, J., Wu, Y.-T., Grishin, N.V. et al. (2015) Phosphorylation of innate immune adaptor proteins MAVS, STING, and TRIF induces IRF3 activation. *Science*, **347**, aaa2630.
 99. Ma, W., Huang, G., Wang, Z., Wang, L. and Gao, Q. (2023) IRF7: role and regulation in immunity and autoimmunity. *Frontiers in Immunology*, **Volume 14 - 2023**.
 100. Ren, Z., Ding, T., Zuo, Z., Xu, Z., Deng, J. and Wei, Z. (2020) Regulation of MAVS Expression and Signaling Function in the Antiviral Innate Immune Response. *Frontiers in Immunology*, **Volume 11 - 2020**.

References

101. Walter, M.R. (2020) The Role of Structure in the Biology of Interferon Signaling. *Frontiers in Immunology*, **Volume 11 - 2020**.
102. Schneider, W.M., Chevillotte, M.D. and Rice, C.M. (2014) Interferon-stimulated genes: a complex web of host defenses. *Annu Rev Immunol*, **32**, 513-545.
103. Hu, X., Li, J., Fu, M., Zhao, X. and Wang, W. (2021) The JAK/STAT signaling pathway: from bench to clinic. *Signal Transduction and Targeted Therapy*, **6**, 402.
104. Paul, A., Tang, T.H. and Ng, S.K. (2018) Interferon Regulatory Factor 9 Structure and Regulation. *Frontiers in Immunology*, **Volume 9 - 2018**.
105. Schoggins, J.W. (2019) Interferon-Stimulated Genes: What Do They All Do? *Annual Review of Virology*, **6**, 567-584.
106. Schoggins, J.W. and Rice, C.M. (2011) Interferon-stimulated genes and their antiviral effector functions. *Curr Opin Virol*, **1**, 519-525.
107. Ravi Sundar Jose Geetha, A., Fischer, K., Babadei, O., Smesnik, G., Vogt, A., Platanitis, E., Müller, M., Farlik, M. and Decker, T. (2024) Dynamic control of gene expression by ISGF3 and IRF1 during IFN β and IFN γ signaling. *Embo j*, **43**, 2233-2263.
108. Crow, Y.J. and Stetson, D.B. (2022) The type I interferonopathies: 10 years on. *Nat Rev Immunol*, **22**, 471-483.
109. Mendonça, L.O. and Frémond, M.-L. (2024) Interferonopathies: From concept to clinical practice. *Best Practice & Research Clinical Rheumatology*, **38**, 101975.
110. Arimoto, K.I., Löchte, S., Stoner, S.A., Burkart, C., Zhang, Y., Miyauchi, S., Wilmes, S., Fan, J.B., Heinisch, J.J., Li, Z. *et al.* (2017) STAT2 is an essential adaptor in USP18-mediated suppression of type I interferon signaling. *Nat Struct Mol Biol*, **24**, 279-289.
111. Jové, V., Wheeler, H., Lee, C.W., Healy, D.R., Levine, K., Ralph, E.C., Yamaguchi, M., Jiang, Z.K., Cabral, E., Xu, Y. *et al.* (2024) Type I interferon regulation by USP18 is a key vulnerability in cancer. *iScience*, **27**, 109593.
112. Lin, H., Jiang, M., Liu, L., Yang, Z., Ma, Z., Liu, S., Ma, Y., Zhang, L. and Cao, X. (2019) The long noncoding RNA Lnczc3h7a promotes a TRIM25-mediated RIG-I antiviral innate immune response. *Nature Immunology*, **20**, 812-823.
113. Jiang, M., Zhang, S., Yang, Z., Lin, H., Zhu, J., Liu, L., Wang, W., Liu, S., Liu, W., Ma, Y. *et al.* (2018) Self-Recognition of an Inducible Host lncRNA by RIG-I Feedback Restricts Innate Immune Response. *Cell*, **173**, 906-919.e913.
114. Ma, H., Han, P., Ye, W., Chen, H., Zheng, X., Cheng, L., Zhang, L., Yu, L., Wu, X., Xu, Z. *et al.* (2017) The Long Noncoding RNA NEAT1 Exerts Antihantaviral Effects by Acting as Positive Feedback for RIG-I Signaling. *J Virol*, **91**.
115. Imamura, K., Imamachi, N., Akizuki, G., Kumakura, M., Kawaguchi, A., Nagata, K., Kato, A., Kawaguchi, Y., Sato, H., Yoneda, M. *et al.* (2014) Long Noncoding RNA NEAT1-Dependent SFPO Relocation from Promoter Region to Paraspeckle Mediates IL8 Expression upon Immune Stimuli. *Molecular Cell*, **53**, 393-406.
116. Xie, Q., Chen, S., Tian, R., Huang, X., Deng, R., Xue, B., Qin, Y., Xu, Y., Wang, J., Guo, M. *et al.* (2018) Long Noncoding RNA ITPRIP-1 Positively Regulates the Innate Immune Response through Promotion of Oligomerization and Activation of MDA5. *J Virol*, **92**.

References

117. Marsh, G.A., de Jong, C., Barr, J.A., Tachedjian, M., Smith, C., Middleton, D., Yu, M., Todd, S., Foord, A.J., Haring, V. *et al.* (2012) Cedar Virus: A Novel Henipavirus Isolated from Australian Bats. *PLOS Pathogens*, **8**, e1002836.
118. Sabir, A.J., Rong, L., Broder, C.C. and Amaya, M. (2024) Cedar virus biology and its applications as a surrogate for highly pathogenic henipaviruses. *Cell Insight*, **3**, 100181.
119. Gamble, A., Yeo, Y.Y., Butler, A.A., Tang, H., Snedden, C.E., Mason, C.T., Buchholz, D.W., Bingham, J., Aguilar, H.C. and Lloyd-Smith, J.O. (2021) Drivers and Distribution of Henipavirus-Induced Syncytia: What Do We Know? *Viruses*, **13**, 1755.
120. Aguilar, H.C. and Iorio, R.M. (2012) In Lee, B. and Rota, P. A. (eds.), *Henipavirus: Ecology, Molecular Virology, and Pathogenesis*. Springer Berlin Heidelberg, Berlin, Heidelberg, pp. 79-94.
121. Liu, Q., Stone, J.A., Bradel-Tretheway, B., Dabundo, J., Benavides Montano, J.A., Santos-Montanez, J., Biering, S.B., Nicola, A.V., Iorio, R.M., Lu, X. *et al.* (2013) Unraveling a Three-Step Spatiotemporal Mechanism of Triggering of Receptor-Induced Nipah Virus Fusion and Cell Entry. *PLOS Pathogens*, **9**, e1003770.
122. Aguilar, H.C. and Lee, B. (2011) Emerging paramyxoviruses: molecular mechanisms and antiviral strategies. *Expert Reviews in Molecular Medicine*, **13**, e6.
123. Zimmer, G., Budz, L. and Herrler, G. (2001) Proteolytic Activation of Respiratory Syncytial Virus Fusion Protein: CLEAVAGE AT TWO FURIN CONSENSUS SEQUENCES*. *Journal of Biological Chemistry*, **276**, 31642-31650.
124. Diederich, S., Moll, M., Klenk, H.-D. and Maisner, A. (2005) The Nipah Virus Fusion Protein Is Cleaved within the Endosomal Compartment *. *Journal of Biological Chemistry*, **280**, 29899-29903.
125. Yeo, Y.Y., Buchholz, D.W., Gamble, A., Jager, M. and Aguilar, H.C. (2021) Headless Henipaviral Receptor Binding Glycoproteins Reveal Fusion Modulation by the Head/Stalk Interface and Post-receptor Binding Contributions of the Head Domain. *Journal of Virology*, **95**, 10.1128/jvi.00666-00621.
126. Wang, L.-F., Harcourt, B.H., Yu, M., Tamin, A., Rota, P.A., Bellini, W.J. and Eaton, B.T. (2001) Molecular biology of Hendra and Nipah viruses. *Microbes and Infection*, **3**, 279-287.
127. Diederich, S., Babiuk, S. and Boshra, H. (2023) A Survey of Henipavirus Tropism-Our Current Understanding from a Species/Organ and Cellular Level. *Viruses*, **15**.
128. Eaton, B.T., Broder, C.C., Middleton, D. and Wang, L.-F. (2006) Hendra and Nipah viruses: different and dangerous. *Nature Reviews Microbiology*, **4**, 23-35.
129. Audsley, M.D. and Moseley, G.W. (2013) Paramyxovirus evasion of innate immunity: Diverse strategies for common targets. *World J Virol*, **2**, 57-70.
130. Parks, G.D. and Alexander-Miller, M.A. (2013) Paramyxovirus activation and inhibition of innate immune responses. *J Mol Biol*, **425**, 4872-4892.
131. Pisanelli, G., Pagnini, U., Iovane, G. and García-Sastre, A. (2022) Type I and Type II Interferon Antagonism Strategies Used by Paramyxoviridae: Previous and New Discoveries, in Comparison. *Viruses*, **14**.

References

132. Andrejeva, J., Childs, K.S., Young, D.F., Carlos, T.S., Stock, N., Goodbourn, S. and Randall, R.E. (2004) The V proteins of paramyxoviruses bind the IFN-inducible RNA helicase, mda-5, and inhibit its activation of the IFN-beta promoter. *Proc Natl Acad Sci U S A*, **101**, 17264-17269.
133. Childs, K.S., Andrejeva, J., Randall, R.E. and Goodbourn, S. (2009) Mechanism of mda-5 Inhibition by Paramyxovirus V Proteins. *Journal of Virology*, **83**, 1465-1473.
134. Ramachandran, A. and Horvath Curt, M. (2010) Dissociation of Paramyxovirus Interferon Evasion Activities: Universal and Virus-Specific Requirements for Conserved V Protein Amino Acids in MDA5 Interference. *Journal of Virology*, **84**, 11152-11163.
135. Parisien, J.-P., Bamming, D., Komuro, A., Ramachandran, A., Rodriguez, J.J., Barber, G., Wojahn, R.D. and Horvath, C.M. (2009) A Shared Interface Mediates Paramyxovirus Interference with Antiviral RNA Helicases MDA5 and LGP2. *Journal of Virology*, **83**, 7252-7260.
136. Davis, M.E., Wang, M.K., Rennick, L.J., Full, F., Gableske, S., Mesman, A.W., Gringhuis, S.I., Geijtenbeek, T.B., Duprex, W.P. and Gack, M.U. (2014) Antagonism of the phosphatase PP1 by the measles virus V protein is required for innate immune escape of MDA5. *Cell Host Microbe*, **16**, 19-30.
137. Wagner, N.D., Liu, H., Rohrs, H.W., Amarasinghe, G.K., Gross, M.L. and Leung, D.W. (2022) Nipah Virus V Protein Binding Alters MDA5 Helicase Folding Dynamics. *ACS Infectious Diseases*, **8**, 118-128.
138. Sánchez-Aparicio, M.T., Feinman, L.J., García-Sastre, A. and Shaw, M.L. (2018) Paramyxovirus V Proteins Interact with the RIG-I/TRIM25 Regulatory Complex and Inhibit RIG-I Signaling. *J Virol*, **92**.
139. Shaw, M.L., García-Sastre, A., Palese, P. and Basler, C.F. (2004) Nipah virus V and W proteins have a common STAT1-binding domain yet inhibit STAT1 activation from the cytoplasmic and nuclear compartments, respectively. *J Virol*, **78**, 5633-5641.
140. Rodriguez, J.J., Parisien, J.P. and Horvath, C.M. (2002) Nipah virus V protein evades alpha and gamma interferons by preventing STAT1 and STAT2 activation and nuclear accumulation. *J Virol*, **76**, 11476-11483.
141. Becker, N. and Maisner, A. (2023) Nipah Virus Impairs Autocrine IFN Signaling by Sequestering STAT1 and STAT2 into Inclusion Bodies. *Viruses*, **15**, 554.
142. Shaw, M.L., Cardenas, W.B., Zamarin, D., Palese, P. and Basler, C.F. (2005) Nuclear localization of the Nipah virus W protein allows for inhibition of both virus- and toll-like receptor 3-triggered signaling pathways. *J Virol*, **79**, 6078-6088.
143. Lieu, K.G., Marsh, G.A., Wang, L.-F. and Netter, H.J. (2015) The non-pathogenic Henipavirus Cedar paramyxovirus phosphoprotein has a compromised ability to target STAT1 and STAT2. *Antiviral Research*, **124**, 69-76.
144. Scheibe, M., Butter, F., Hafner, M., Tuschl, T. and Mann, M. (2012) Quantitative mass spectrometry and PAR-CLIP to identify RNA-protein interactions. *Nucleic Acids Res*, **40**, 9897-9902.
145. Srisawat, C. and Engelke, D.R. (2001) Streptavidin aptamers: affinity tags for the study of RNAs and ribonucleoproteins. *Rna*, **7**, 632-641.

References

146. Butter, F., Scheibe, M., Morl, M. and Mann, M. (2009) Unbiased RNA-protein interaction screen by quantitative proteomics. *Proc Natl Acad Sci U S A*, **106**, 10626-10631.
147. Abramson, J., Adler, J., Dunger, J., Evans, R., Green, T., Pritzel, A., Ronneberger, O., Willmore, L., Ballard, A.J., Bambrick, J. *et al.* (2024) Accurate structure prediction of biomolecular interactions with AlphaFold 3. *Nature*, **630**, 493-500.
148. Trendel, J., Schwarzl, T., Horos, R., Prakash, A., Bateman, A., Hentze, M.W. and Krijgsveld, J. (2019) The Human RNA-Binding Proteome and Its Dynamics during Translational Arrest. *Cell*, **176**, 391-403.e319.
149. Dubois, M.-L. and Boisvert, F.-M. (2016) In Bazett-Jones, D. P. and Dellaire, G. (eds.), *The Functional Nucleus*. Springer International Publishing, Cham, pp. 29-49.
150. Ponti, D. (2025) The Nucleolus: A Central Hub for Ribosome Biogenesis and Cellular Regulatory Signals. *International Journal of Molecular Sciences*, **26**, 4174.
151. Bhutada, P., Favre, S., Jaafar, M., Hafner, J., Liesinger, L., Unterweger, S., Bischof, K., Darnhofer, B., Siva Sankar, D., Rechberger, G. *et al.* (2022) Rbp95 binds to 25S rRNA helix H95 and cooperates with the Npa1 complex during early pre-60S particle maturation. *Nucleic Acids Research*, **50**, 10053-10077.
152. Rohrmoser, M., Hölzel, M., Grimm, T., Malamoussi, A., Harasim, T., Orban, M., Pfisterer, I., Gruber-Eber, A., Kremmer, E. and Eick, D. (2007) Interdependence of Pes1, Bop1, and WDR12 controls nucleolar localization and assembly of the PeBoW complex required for maturation of the 60S ribosomal subunit. *Mol Cell Biol*, **27**, 3682-3694.
153. Hu, X., Chen, F., Jia, L., Long, A., Peng, Y., Li, X., Huang, J., Wei, X., Fang, X., Gao, Z. *et al.* (2024) A gut-derived hormone regulates cholesterol metabolism. *Cell*, **187**, 1685-1700.e1618.
154. Shou, F., Li, G. and Morshedi, M. (2024) Long Non-coding RNA ANRIL and Its Role in the Development of Age-Related Diseases. *Mol Neurobiol*, **61**, 7919-7929.
155. Gareev, I., Kudriashov, V., Sufianov, A., Begliarzade, S., Ilyasova, T., Liang, Y. and Beylerli, O. (2022) The role of long non-coding RNA ANRIL in the development of atherosclerosis. *Noncoding RNA Res*, **7**, 212-216.
156. Dörner, K., Ruggeri, C., Zemp, I. and Kutay, U. (2023) Ribosome biogenesis factors— from names to functions. *The EMBO Journal*, **42**, e112699.
157. Lu, J., Gu, B., Lu, W., Liu, J. and Lu, J. (2023) Lnc-ANRIL modulates the immune response associated with NF- κ B pathway in LPS-stimulated bovine mammary epithelial cells. *Immun Inflamm Dis*, **11**, e1125.
158. Bocchetti, M., Scrima, M., Melisi, F., Luce, A., Sperlongano, R., Caraglia, M., Zappavigna, S. and Cossu, A.M. (2021) LncRNAs and Immunity: Coding the Immune System with Noncoding Oligonucleotides. *Int J Mol Sci*, **22**.
159. Hu, J., Wang, D., Wu, H., Yang, Z., Yang, N. and Dong, J. (2019) Long non-coding RNA ANRIL-mediated inflammation response is involved in protective effect of rhein in uric acid nephropathy rats. *Cell Biosci*, **9**, 11.

References

160. Cuenda, A. and Rousseau, S. (2007) p38 MAP-Kinases pathway regulation, function and role in human diseases. *Biochimica et Biophysica Acta (BBA) - Molecular Cell Research*, **1773**, 1358-1375.
161. Kumar, R., Khandelwal, N., Thachamvally, R., Tripathi, B.N., Barua, S., Kashyap, S.K., Maherchandani, S. and Kumar, N. (2018) Role of MAPK/MNK1 signaling in virus replication. *Virus Res*, **253**, 48-61.
162. Zou, W. and Zhang, D.-E. (2006) The Interferon-inducible Ubiquitin-protein Isopeptide Ligase (E3) EFP Also Functions as an ISG15 E3 Ligase *. *Journal of Biological Chemistry*, **281**, 3989-3994.
163. Sanchez, J.G., Chiang, J.J., Sparrer, K.M.J., Alam, S.L., Chi, M., Roganowicz, M.D., Sankaran, B., Gack, M.U. and Pornillos, O. (2016) Mechanism of TRIM25 Catalytic Activation in the Antiviral RIG-I Pathway. *Cell Rep*, **16**, 1315-1325.
164. Shemesh, M., Lochte, S., Piehler, J. and Schreiber, G. (2021) IFNAR1 and IFNAR2 play distinct roles in initiating type I interferon-induced JAK-STAT signaling and activating STATs. *Science Signaling*, **14**, eabe4627.
165. Pinho, S.S., Alves, I., Gaifem, J. and Rabinovich, G.A. (2023) Immune regulatory networks coordinated by glycans and glycan-binding proteins in autoimmunity and infection. *Cellular & Molecular Immunology*, **20**, 1101-1113.
166. Wang, W.-H., Lin, C.-Y., Chang, M.R., Urbina, A.N., Assavalapsakul, W., Thitithanyanont, A., Chen, Y.-H., Liu, F.-T. and Wang, S.-F. (2020) The role of galectins in virus infection - A systemic literature review. *Journal of Microbiology, Immunology and Infection*, **53**, 925-935.
167. Martinez, W.M. and Spear, P.G. (2001) Structural Features of Nectin-2 (HveB) Required for Herpes Simplex Virus Entry. *Journal of Virology*, **75**, 11185-11195.
168. Wang, J., Zheng, X., Peng, Q., Zhang, X. and Qin, Z. (2020) Eph receptors: the bridge linking host and virus. *Cell Mol Life Sci*, **77**, 2355-2365.
169. Nyström, K., Biller, M., Grahn, A., Lindh, M., Larson, G. and Olofsson, S. (2004) Real time PCR for monitoring regulation of host gene expression in herpes simplex virus type 1-infected human diploid cells. *Journal of Virological Methods*, **118**, 83-94.
170. Kuchipudi, S.V., Tellabati, M., Nelli, R.K., White, G.A., Perez, B.B., Sebastian, S., Slomka, M.J., Brookes, S.M., Brown, I.H., Dunham, S.P. *et al.* (2012) 18S rRNA is a reliable normalisation gene for real time PCR based on influenza virus infected cells. *Virology Journal*, **9**, 1-7.
171. Zhao, J., He, S., Minassian, A., Li, J. and Feng, P. (2015) Recent advances on viral manipulation of NF-κB signaling pathway. *Curr Opin Virol*, **15**, 103-111.
172. Yu, K., Peng, H., Zhang, Z., Ye, L., Zhan, K., Li, C., Gan, L., Lin, Y., Wang, Y., Song, Y. *et al.* (2025) Long non-coding RNA ANRIL/p65 negative feedback loop protects intestinal barrier function in inflammatory bowel disease. *Non-coding RNA Research*.
173. Chen, M., Tachedjian, M., Marsh, G.A., Cui, J. and Wang, L.F. (2020) Distinct Cell Transcriptomic Landscapes Upon Henipavirus Infections. *Front Microbiol*, **11**, 986.

References

174. Garner, O.B., Aguilar, H.C., Fulcher, J.A., Levroney, E.L., Harrison, R., Wright, L., Robinson, L.R., Aspericueta, V., Panico, M., Haslam, S.M. *et al.* (2010) Endothelial Galectin-1 Binds to Specific Glycans on Nipah Virus Fusion Protein and Inhibits Maturation, Mobility, and Function to Block Syncytia Formation. *PLOS Pathogens*, **6**, e1000993.
175. Yu, K., Peng, H., Zhang, Z., Ye, L., Zhan, K., Li, C., Gan, L., Lin, Y., Wang, Y., Song, Y. *et al.* (2025) Long non-coding RNA ANRIL/p65 negative feedback loop protects intestinal barrier function in inflammatory bowel disease. *Non-coding RNA Research*, **12**, 167-179.
176. Eustermann, S., Schall, K., Kostrewa, D., Lakomek, K., Strauss, M., Moldt, M. and Hopfner, K.-P. (2018) Structural basis for ATP-dependent chromatin remodelling by the INO80 complex. *Nature*, **556**, 386-390.
177. Cai, Y., Jin, J., Yao, T., Gottschalk, A.J., Swanson, S.K., Wu, S., Shi, Y., Washburn, M.P., Florens, L., Conaway, R.C. *et al.* (2007) YY1 functions with INO80 to activate transcription. *Nature Structural & Molecular Biology*, **14**, 872-874.
178. Wu, S., Shi, Y., Mulligan, P., Gay, F., Landry, J., Liu, H., Lu, J., Qi, H.H., Wang, W., Nickoloff, J.A. *et al.* (2007) A YY1-INO80 complex regulates genomic stability through homologous recombination-based repair. *Nat Struct Mol Biol*, **14**, 1165-1172.
179. Delhaye, L., De Bruycker, E., Volders, P.-J., Fijalkowska, D., De Sutter, D., Degroeve, S., Martens, L., Mestdagh, P. and Eyckerman, S. (2022) Orthogonal proteomics methods to unravel the HOTAIR interactome. *Scientific Reports*, **12**, 1513.
180. Scherer, M., Levin, M., Butter, F. and Scheibe, M. (2020) Quantitative Proteomics to Identify Nuclear RNA-Binding Proteins of Malat1. *Int J Mol Sci*, **21**.
181. Van Nostrand, E.L., Freese, P., Pratt, G.A., Wang, X., Wei, X., Xiao, R., Blue, S.M., Chen, J.Y., Cody, N.A.L., Dominguez, D. *et al.* (2020) A large-scale binding and functional map of human RNA-binding proteins. *Nature*, **583**, 711-719.
182. Li, J.H., Liu, S., Zheng, L.L., Wu, J., Sun, W.J., Wang, Z.L., Zhou, H., Qu, L.H. and Yang, J.H. (2014) Discovery of Protein-lncRNA Interactions by Integrating Large-Scale CLIP-Seq and RNA-Seq Datasets. *Front Bioeng Biotechnol*, **2**, 88.
183. Lebedeva, S., Jens, M., Theil, K., Schwanhäusser, B., Selbach, M., Landthaler, M. and Rajewsky, N. (2011) Transcriptome-wide Analysis of Regulatory Interactions of the RNA-Binding Protein HuR. *Molecular Cell*, **43**, 340-352.
184. Ripin, N., Boudet, J., Duszczuk, M.M., Hinniger, A., Faller, M., Krepl, M., Gadi, A., Schneider, R.J., Šponer, J., Meisner-Kober, N.C. *et al.* (2019) Molecular basis for AU-rich element recognition and dimerization by the HuR C-terminal RRM. *Proc Natl Acad Sci U S A*, **116**, 2935-2944.
185. Simion, V., Zhou, H., Haemmig, S., Pierce, J.B., Mendes, S., Tesmenitsky, Y., Pérez-Cremades, D., Lee, J.F., Chen, A.F., Ronda, N. *et al.* (2020) A macrophage-specific lncRNA regulates apoptosis and atherosclerosis by tethering HuR in the nucleus. *Nat Commun*, **11**, 6135.

References

186. Su, X., Li, W., Zhang, D. and Zhu, H. (2023) Melatonin Regulates lncRNA NEAT1/miR-138-5p/HIF-1 α Axis through MOV10 to Affect Acid-Related Esophageal Epithelial Cell Pyroptosis. *Pharmacology*, **108**, 344-358.
187. Fu, K., Tian, S., Tan, H., Wang, C., Wang, H., Wang, M., Wang, Y., Chen, Z., Wang, Y., Yue, Q. *et al.* (2019) Biological and RNA regulatory function of MOV10 in mammalian germ cells. *BMC Biology*, **17**, 39.
188. El Messaoudi-Aubert, S., Nicholls, J., Maertens, G.N., Brookes, S., Bernstein, E. and Peters, G. (2010) Role for the MOV10 RNA helicase in polycomb-mediated repression of the INK4a tumor suppressor. *Nat Struct Mol Biol*, **17**, 862-868.
189. Guarnaccia, A.D. and Tansey, W.P. (2018) Moonlighting with WDR5: A Cellular Multitasker. *J Clin Med*, **7**.
190. Han, P. and Chang, C.P. (2015) Long non-coding RNA and chromatin remodeling. *RNA Biol*, **12**, 1094-1098.
191. Bhan, A. and Mandal, S.S. (2015) LncRNA HOTAIR: A master regulator of chromatin dynamics and cancer. *Biochim Biophys Acta*, **1856**, 151-164.
192. Loda, A., Collombet, S. and Heard, E. (2022) Gene regulation in time and space during X-chromosome inactivation. *Nature Reviews Molecular Cell Biology*, **23**, 231-249.
193. Malakar, P., Shukla, S., Mondal, M., Kar, R.K. and Siddiqui, J.A. (2024) The nexus of long noncoding RNAs, splicing factors, alternative splicing and their modulations. *RNA Biol*, **21**, 1-20.
194. Ma, W., Qiao, J., Zhou, J., Gu, L. and Deng, D. (2020) Characterization of novel LncRNA P14AS as a protector of ANRIL through AUF1 binding in human cells. *Mol Cancer*, **19**, 42.
195. Ma, W. and Hu, J. (2023) The linear ANRIL transcript P14AS regulates the NF- κ B signaling to promote colon cancer progression. *Molecular Medicine*, **29**, 162.
196. Xie, X., Lin, J., Fan, X., Zhong, Y., Chen, Y., Liu, K., Ren, Y., Chen, X., Lai, D., Li, X. *et al.* (2021) LncRNA CDKN2B-AS1 stabilized by IGF2BP3 drives the malignancy of renal clear cell carcinoma through epigenetically activating NUF2 transcription. *Cell Death Dis*, **12**, 201.
197. Wan, J., Bao, Y., Hou, L.J., Li, G.J., Du, L.J., Ma, Z.H., Yang, G.K., Hou, Y., Li, Z.X. and Yang, Y. (2023) lncRNA ANRIL accelerates wound healing in diabetic foot ulcers via modulating HIF1A/VEGFA signaling through interacting with FUS. *J Gene Med*, **25**, e3462.
198. McCool, M.A., Buhagiar, A.F., Bryant, C.J., Ogawa, L.M., Abriola, L., Surovtseva, Y.V. and Baserga, S.J. (2022) Human pre-60S assembly factors link rRNA transcription to pre-rRNA processing. *Rna*, **29**, 82-96.
199. Jiao, L., Liu, Y., Yu, X.-Y., Pan, X., Zhang, Y., Tu, J., Song, Y.-H. and Li, Y. (2023) Ribosome biogenesis in disease: new players and therapeutic targets. *Signal Transduction and Targeted Therapy*, **8**, 15.

References

200. Jia, F., Wu, Q., Wang, Z., Zhang, M., Yuan, S., Che, Y., Li, B., Hu, Z. and Hu, X. (2021) BOP1 Knockdown Attenuates Neointimal Hyperplasia by Activating p53 and Inhibiting Nascent Protein Synthesis. *Oxid Med Cell Longev*, **2021**, 5986260.
201. Han, S. and Chen, L.L. (2024) Long non-coding RNAs in the nucleolus: Biogenesis, regulation, and function. *Curr Opin Struct Biol*, **87**, 102866.
202. Mamontova, V., Trifault, B., Boten, L. and Burger, K. (2021) Commuting to Work: Nucleolar Long Non-Coding RNA Control Ribosome Biogenesis from Near and Far. *Non-Coding RNA*, **7**, 42.
203. Dunbrack, R.L. (2025) Rēs ipSAE loquunt: What’s wrong with AlphaFold’s ipTM score and how to fix it. *bioRxiv*, 2025.2002.2010.637595.
204. Ludaic, M. and Elofsson, A. (2025) Limits of deep-learning-based RNA prediction methods. *bioRxiv*, 2025.2004.2030.651414.
205. Wang, Z.-W., Pan, J.-J., Hu, J.-F., Zhang, J.-Q., Huang, L., Huang, Y., Liao, C.-Y., Yang, C., Chen, Z.-W., Wang, Y.-D. *et al.* (2022) SRSF3-mediated regulation of N6-methyladenosine modification-related lncRNA ANRIL splicing promotes resistance of pancreatic cancer to gemcitabine. *Cell Reports*, **39**.
206. Yoon, J.H. and Gorospe, M. (2016) Cross-Linking Immunoprecipitation and qPCR (CLIP-qPCR) Analysis to Map Interactions Between Long Noncoding RNAs and RNA-Binding Proteins. *Methods Mol Biol*, **1402**, 11-17.
207. Peng, X., Gralinski, L., Armour, C.D., Ferris, M.T., Thomas, M.J., Proll, S., Bradel-Tretheway, B.G., Korth, M.J., Castle, J.C., Biery, M.C. *et al.* (2010) Unique signatures of long noncoding RNA expression in response to virus infection and altered innate immune signaling. *mBio*, **1**.
208. Warden, C.D. and Wu, X. (2024) Critical Differential Expression Assessment for Individual Bulk RNA-Seq Projects. *bioRxiv*.
209. Dass, D., Dhotre, K., Chakraborty, M., Nath, A., Banerjee, A., Bagchi, P. and Mukherjee, A. (2023) miRNAs in Herpesvirus Infection: Powerful Regulators in Small Packages. *Viruses*, **15**.
210. Sorel, O. and Dewals, B.G. (2016) MicroRNAs in large herpesvirus DNA genomes: recent advances. *Biomolecular Concepts*, **7**, 229-239.
211. Gaucherand, L. and Gaglia, M.M. (2022) The Role of Viral RNA Degrading Factors in Shutoff of Host Gene Expression. *Annu Rev Virol*, **9**, 213-238.
212. Ludwig, S. and Planz, O. (2008) Influenza viruses and the NF- κ B signaling pathway – towards a novel concept of antiviral therapy. *Biological Chemistry*, **389**, 1307-1312.
213. Huang, Y., Su, Y., Shen, L., Huo, Z., Chen, C., Sun, T., Tian, X., Li, N. and Yang, C. (2022) A novel IFNbeta-induced long non-coding RNA ZAP-IT1 interrupts Zika virus replication in A549 cells. *Virologica Sinica*, **37**, 904-912.
214. Vella, P., Barozzi, I., Cuomo, A., Bonaldi, T. and Pasini, D. (2011) Yin Yang 1 extends the Myc-related transcription factors network in embryonic stem cells. *Nucleic Acids Research*, **40**, 3403-3418.

References

215. Schutt, C., Hallmann, A., Hachim, S., Klockner, I., Valussi, M., Atzberger, A., Graumann, J., Braun, T. and Boettger, T. (2020) LincMYH configures INO80 to regulate muscle stem cell numbers and skeletal muscle hypertrophy. *The EMBO Journal*, **39**, e105098.
216. Fullam, A. and Schröder, M. (2013) DExD/H-box RNA helicases as mediators of anti-viral innate immunity and essential host factors for viral replication. *Biochim Biophys Acta*, **1829**, 854-865.
217. Watson, S.F., Bellora, N. and Macias, S. (2020) ILF3 contributes to the establishment of the antiviral type I interferon program. *Nucleic Acids Res*, **48**, 116-129.
218. Levroney, E.L., Aguilar, H.C., Fulcher, J.A., Kohatsu, L., Pace, K.E., Pang, M., Gurney, K.B., Baum, L.G. and Lee, B. (2005) Novel Innate Immune Functions for Galectin-1: Galectin-1 Inhibits Cell Fusion by Nipah Virus Envelope Glycoproteins and Augments Dendritic Cell Secretion of Proinflammatory Cytokines1. *The Journal of Immunology*, **175**, 413-420.
219. Bluhm, A., Viceconte, N., Li, F., Rane, G., Ritz, S., Wang, S., Levin, M., Shi, Y., Kappei, D. and Butter, F. (2019) ZBTB10 binds the telomeric variant repeat TTGGGG and interacts with TRF2. *Nucleic Acids Res*, **47**, 1896-1907.
220. Shevchenko, A., Tomas, H., Havlis, J., Olsen, J.V. and Mann, M. (2006) In-gel digestion for mass spectrometric characterization of proteins and proteomes. *Nat Protoc*, **1**, 2856-2860.
221. Rappsilber, J., Mann, M. and Ishihama, Y. (2007) Protocol for micro-purification, enrichment, pre-fractionation and storage of peptides for proteomics using StageTips. *Nat Protoc*, **2**, 1896-1906.
222. Elfmann, C. and Stülke, J. (2023) PAE viewer: a webserver for the interactive visualization of the predicted aligned error for multimer structure predictions and crosslinks. *Nucleic Acids Research*, **51**, W404-W410.
223. Sehnal, D., Bittrich, S., Deshpande, M., Svobodová, R., Berka, K., Bazgier, V., Velankar, S., Burley, S.K., Koča, J. and Rose, A.S. (2021) Mol* Viewer: modern web app for 3D visualization and analysis of large biomolecular structures. *Nucleic Acids Research*, **49**, W431-W437.
224. Kittler, R., Heninger, A.K., Franke, K., Habermann, B. and Buchholz, F. (2005) Production of endoribonuclease-prepared short interfering RNAs for gene silencing in mammalian cells. *Nat Methods*, **2**, 779-784.
225. Heninger, A.K. and Buchholz, F. (2007) Production of Endoribonuclease-Prepared Short Interfering RNAs (esiRNAs) for Specific and Effective Gene Silencing in Mammalian Cells. *CSH Protoc*, **2007**, pdb prot4824.
226. Henschel, A., Buchholz, F. and Habermann, B. (2004) DEQOR: a web-based tool for the design and quality control of siRNAs. *Nucleic Acids Res*, **32**, W113-120.
227. Rao, X., Huang, X., Zhou, Z. and Lin, X. (2013) An improvement of the 2^{Δ(-ΔΔ)} method for quantitative real-time polymerase chain reaction data analysis. *Biostat Bioinforma Biomath*, **3**, 71-85.

References

228. Damann, N., Rothermel, M., Klupp, B.G., Mettenleiter, T.C., Hatt, H. and Wetzel, C.H. (2006) Chemosensory properties of murine nasal and cutaneous trigeminal neurons identified by viral tracing. *BMC Neurosci*, **7**, 46.
229. Lenhard, L., Müller, M., Diederich, S., Loerzer, L., Friedrichs, V., Köllner, B., Finke, S., Dorhoi, A. and Pei, G. (2025) Ephrin B1 and B2 Mediate Cedar Virus Entry into Egyptian Fruit Bat Cells. *Viruses*, **17**, 573.
230. Kärber, G. (1931) Beitrag zur kollektiven Behandlung pharmakologischer Reihenversuche. *Naunyn-Schmiedebergs Archiv für experimentelle Pathologie und Pharmakologie*, **162**, 480-483.
231. Wu, T., Hu, E., Xu, S., Chen, M., Guo, P., Dai, Z., Feng, T., Zhou, L., Tang, W., Zhan, L. *et al.* (2021) clusterProfiler 4.0: A universal enrichment tool for interpreting omics data. *Innovation (Camb)*, **2**, 100141.
232. Yu, G. and He, Q.Y. (2016) ReactomePA: an R/Bioconductor package for reactome pathway analysis and visualization. *Mol Biosyst*, **12**, 477-479.

Curriculum vitae

Patricia Schupp

-

Education

PhD - Johannes Gutenberg University Mainz	2025
<i>Titel: "Quantitative interactomics screen reveals the role of the lncRNA ANRIL during viral infection"</i>	
<i>Final grade: tba</i>	
Master of Science in Biology - Johannes Gutenberg University Mainz	2020
<i>Titel: "Substances from traditional Chinese medicine induce different types of cell death in therapy-resistant prostate carcinoma cells"</i>	
<i>Final grade: 1.3</i>	
Bachelor of Science in Biology - Johannes Gutenberg University Mainz	2018
<i>Titel: "The importance of PIAS1 for the progressive growth of renal cell carcinoma"</i>	
<i>Final grade: 2.0</i>	
Abitur - Albrecht-Dürer-Schule Weiterstadt	2013
<i>Final grade: 2.6</i>	

Professional experience

Institute for Molecular Biology (IMB), Mainz	April 2021 - August 2021
<i>Research Assistant at AG Falk Butter</i>	
Helmholtz-Institut Mainz, Mainz	January 2017 – May 2019
<i>Working student</i>	
Molecular Pharmacology and Immunology, University Medicine Mainz	Sept. 2016 – Nov. 2016
<i>Internship at AG Hartmut Kleinert</i>	
<i>Titel: „Post transcriptional regulation of the inducible nitrogen monoxide synthase“</i>	

Publications

- Quantitative interactomics screen reveals the role of the lncRNA ANRIL during viral infection* in submission
- Authors: **Schupp, P.** et al.
Shikonin Inhibits Cell Growth of Sunitinib-Resistant Renal Cell Carcinoma by Activating the Necrosome Complex and Inhibiting the AKT/mTOR Signaling Pathway Front Oncol. 2022
- Authors: Markowitsch et al., including **Schupp, P.**
 DOI: 10.3390/cancers14051114
Artesunate Inhibits the Growth Behavior of Docetaxel-Resistant Prostate Cancer Cells Cancers 2022
- Authors: Vakhrusheva et al., including **Schupp, P.**
 DOI: 10.3389/fonc.2022.789284
Shikonin reduces growth of docetaxel-resistant prostate cancer cells mainly through necroptosis Cancers 2021
- Authors: Markowitsch et al., including **Schupp, P.**
 DOI: 10.3390/cancers13040882
Artesunate Inhibits Growth of Sunitinib-Resistant Renal Cell Carcinoma Cells through Cell Cycle Arrest and Induction of Ferroptosis Cancers (Basel) 2020
- Authors: Markowitsch et al., including **Schupp, P.**
 DOI: 10.3390/cancers12113150

Conferences

- 29th annual RNA Society Confer - Edinburgh, Scotland* 28. May – 2. June 2024
- Type:** Poster presentation
Titel: “Unraveling the RNA-Protein Interactome: Exploration of RNA Binding Proteins in Cellular Dynamics”
RNA 3' end formation and the regulation of eukaryotic genomes - Oxford, United Kingdom 19 – 23. September 2022
- Type:** Poster presentation
Titel: “Investigating the impact of conserved 3'UTR structures on gene expression”
6th Science Day – TransMed Graduate School - Mainz 19. September 2019
- Type:** Poster presentation
Titel: “Artesunate reduces cell growth and induces ferroptosis in resistant RCC cell lines”